

Quantum Simulation of Spin-1 Physics with Bosons in Optical Lattice

by

Woo Chang Chung

B.A., Columbia University (2013)

Submitted to the Department of Physics
in partial fulfillment of the requirements for the degree of

Doctor of Philosophy in Physics

at the

MASSACHUSETTS INSTITUTE OF TECHNOLOGY

June 2021

© Massachusetts Institute of Technology 2021. All rights reserved.

Author
Department of Physics
May 15, 2021

Certified by.....
Wolfgang Ketterle
John D. MacArthur Professor of Physics
Thesis Supervisor

Accepted by
Deepto Chakrabarty
Associate Department Head of Physics

Quantum Simulation of Spin-1 Physics with Bosons in Optical Lattice

by

Woo Chang Chung

Submitted to the Department of Physics
on May 15, 2021, in partial fulfillment of the
requirements for the degree of
Doctor of Philosophy in Physics

Abstract

Mott insulators of ultracold atoms in optical lattices are widely used as an experimental platform for simulating and studying many-body physics. A topic at the frontier of quantum simulation with Mott insulators is the study of quantum spin models, which are intimately connected to other modern research topics such as the study of quantum phase transitions and quantum thermalization. While quantum spin models are also realized and have traditionally been studied with complex magnetic materials in solid-state physics, the advantages of a cold atom quantum simulator are its wide tunability of model parameters and its capability of preparing a variety of initial states, some of which may not even be possible in solid-state settings.

So far, most of the spin models realized with two-component atom clouds in optical lattices are based on Mott insulators with singly occupied sites. In this thesis, I describe how a Mott insulator with doubly occupied sites gives rise to a qualitatively new spin model. In particular, the addition of the on-site interaction in doubly occupied sites gives rise to a new magnetic anisotropy term known as a single-ion anisotropy, which is inaccessible to models with singly occupied lattice sites. The thesis describes in detail the mapping from a doubly-occupied Mott insulator to an effective spin-1 Heisenberg model with a tunable single-ion anisotropy, along with the details of the experimental setup and the benchmarks that need to met in order to probe low-energy physics such as those studied in the effective spin model. I demonstrate that the experimentally realized spin chains in our optical lattice features coherent spin-1 exchange dynamics and also demonstrate a remarkable interplay between the spin exchange and the single-ion anisotropy term.

The atomic species used is ^{87}Rb , and its internal structure allows the use of a state-dependent lattice with an appreciable detuning from resonances. I explain how the state-dependent lattice is used to control the spin-dependent interaction and how it can be used to initialize a two-component atom cloud into a spin Mott insulator, which is a spinful state with no density and spin fluctuation. The spin Mott insulator state is highly interesting because it can be used as an initial state for adiabatic passages to different spinful states, such as the spin superfluid state or an antiferromagnetically

textured spin state. I describe the on-going experimental efforts for making adiabatic passages from the spin Mott to the aforementioned target states and provide an outlook on how the experimental setup can be upgraded for a cleaner and more versatile study of spin-1 physics within the optical lattice.

Thesis Supervisor: Wolfgang Ketterle

Title: John D. MacArthur Professor of Physics

Acknowledgments

During my time at MIT I got to know and work with many smart and intellectually motivated people; I consider this the biggest perk of studying physics in a graduate school. Without their help and willingness to stop and listen for questions and answers, I do not think I would have made this far.

I would first like to acknowledge my advisor Wolfgang Ketterle. He was willing to take me into his group when I had no prior experience with atomic physics or laser optics, and his style of teaching has had a profound impact on my understanding of physics and perhaps on my life as well. I used to be a student who was so easily impressed by complicated/convoluted mathematical equations and knowledge of technical details when searching for answers to scientific problems. I also used to look down upon “obvious” problems and concepts and not study them carefully. However, Wolfgang’s insistence on simplicity and intuitive pictures of the given problem that can convince any other scientist has helped me analyze problems from a more effective angle and communicate my understanding better to my colleagues. As a result I feel much more confident about communicating scientific (and also non-scientific) ideas than I used to.

Julius de Hond joined our group as a postdoc in late October 2018 and has overlapped with me just under three years, but he has had a great influence on me and others within the group with his diverse set of skills and very nice personality. He helped me move forward when I was not feeling too optimistic about the experimental progress within the lab, and his proficiency with numerical simulations has helped us gain better insight to the spin model we are studying. I feel like our working styles complemented each other and I really enjoyed my last several years of doctoral studies because of his help and frequent exchange of ideas in and outside the lab. And this thesis would have not come to fruition without his extensive proofreading.

Jinggang Xiang also joined our group several months earlier than Julius, and he was eager to get things done on the first day he joined. I think all of us in the group were impressed by his construction of a home-made white-light interferometer and

characterization of optical aberrations in an objective, all of which were done in his first year. I feel sorry that I could not finish building the microscope setup with him, which he hoped to do early in his graduate school career, but I hope that I will enjoy his new role and responsibility as the new senior student of the group. Enid Cruz-Cólon is the latest member of the rubidium team and while she is yet inexperienced in atomic physics research like I was when I was a junior student, I am happy to see the progress she has been making lately in the lab and also in her participation in our discussions. I would also like to thank her for keeping the Thanksgiving dinner party a tradition of the lab. Thanks to her, Jingtang, and Julius, the atmosphere in the rubidium lab has been collegial.

Of course, I also spent a long time as a junior student in the lab, and Colin Kennedy and William Cody Burton were the senior students above me, both from whom I have learned a lot. Colin had a great energy and also a lot of courage when tweaking things and sensitive alignments; this is something I tried to emulate when I became a senior student. Cody was a calm presence that every lab needs, and he never seemed to be disturbed when something wrong happened in the lab while I would panic and feel unsure what to do. I think I absorbed some of that quality when I eventually became the chief debugger of the experiment. It is an interesting fate that the three of us will convene again in the Boulder area when I start my new job after graduation. Wenlan was the postdoc before Julius and she brought a great set of knowledge and skills that she gained from Vladan Vuletic's group. The idea of a microscope upgrade became an actual plan when Colin, Cody, and Wenlan were still in the group and they also contributed to our on-going experimental effort towards the realization of an adiabatic passage within the spin-1 model. I should also mention that Samarth Vadia was an exchange student in our lab for a year and greatly increased the productivity of the lab by providing a new database system.

Outside the rubidium lab, there are many other Ketterle group and CUA members that I learned a lot from and enjoyed talking to, and it would be very difficult to list them all here. I would like to thank in particular the original members of the lithium lab (BEC5) - Jesse Amato-Grill, Ivana Dimitrova, Niki Jepsen and Will "Goreblaster"

Lunden - for sharing materials and ideas with the rubidium lab and also going out to lunches and dinners together. I would also like to acknowledge the current and past members of the Dypole lab (Pierre Barral, Michael Cantara, Li Du, Alan Jamison), BEC3 (Hyungmok Son, Julie Park, Timur Rvachov), and BEC2 (Yair Margalit, Yukun Lu, Furkan Top, Junru Li, Boris Shteynas, Jeongwon Lee) for stimulating discussions and sharing optics. Outside the Ketterle group I would like to acknowledge Lawrence Cheuk, Matthew Nichols and Carsten Robens in Martin Zwierlein's group for sharing important tips for the microscope upgrade and Yu-Ting Chen and Joonseok Hur from Vladan Vuletic's group for sometimes stopping by the far-away rubidium lab office and exchanging ideas or just hanging out. Outside the lab, I enjoyed the weekend potluck dinners that I had with Jinwook Lee and Changhoon Oh, both of whom I met through the Samsung Scholarship program.

Finally, I would like to thank my parents and my older brother for supporting me while I was studying far away from them. They always have thought so proudly of me and unconditionally invested a lot of emotional and financial support for my well-being and education. I feel a bit sad that my continued life in the United States will not allow me to see them in Korea more frequently after my graduation, but we know that our bonds are the strongest. I cannot wait to see them in person and tell them I made it through the finish line.

Contents

1	Introduction	19
1.1	Quantum simulation and ultracold atoms	19
1.2	Why quantum magnetism?	20
1.3	Overview of research efforts in BEC4	21
1.4	Thesis outline	23
2	The BEC4 ^{87}Rb machine	25
2.1	MOT chamber	25
2.1.1	Optical setup	25
2.1.2	MOT loading and molasses	28
2.1.3	Loading of the atom cloud to the magnetic trap	28
2.1.4	Forced RF evaporation in the magnetic trap	29
2.1.5	Transfer to the transport optical dipole trap	29
2.2	Old science chamber	30
2.2.1	Optical setup for dipole traps	30
2.2.2	Optical setup for optical lattices	31
2.2.3	Mitigation of interference fringes	32
2.2.4	Magnetic field control	34
2.2.5	Atom number calibration	37
3	Non-scalar Light Shift	41
3.1	Classical explanation of light shift	41
3.2	Anisotropy in atomic structure	44

3.3	Calculation of atomic polarizability	46
3.4	Wavelength selection	50
4	Optical Lattices	53
4.1	Making an optical lattice	53
4.2	State-dependent optical lattice	57
4.2.1	lin- θ -lin scheme	58
4.2.2	$\sigma^+ - \sigma^-$ scheme	65
5	The Bose-Hubbard Hamiltonian	71
5.1	Review of the derivation	71
5.2	Mean-field phase diagram	73
5.2.1	Perturbative approach	74
5.2.2	Numerical diagonalization	77
5.2.3	Comparison to experiments	79
5.3	Corrections due to higher bands	81
6	Quantum Magnetism	91
6.1	Derivation of an effective Hamiltonian	92
6.1.1	Kinetic Exchange	92
6.1.2	On-site anisotropy	93
6.1.3	Formal mapping	93
6.2	Magnetic phases in spin-1	100
6.3	Spin-1/2 vs spin-1 realizations	102
7	Spin-1 physics with a two-component Bose gas	107
7.1	Measurement of local spin pairing	107
7.2	Observation of exchange in spin-1 model	111
7.2.1	Idea behind the experiment	112
7.2.2	Experimental sequence	114
7.2.3	Result and analysis	115
7.2.4	Possible effects of magnetic gradient	116

7.2.5	Conclusion	119
7.3	Investigation of the spin Mott phase	121
7.3.1	Adiabatic passage with a state-dependent lattice	121
7.3.2	Adiabatic passage with a magnetic gradient	129
8	Conclusion	133
A	Quantum Gas Microscope	137
A.1	Optical aberration	137
A.2	Strategy for a high-flatness vacuum window	141
B	Tunable Single-Ion Anisotropy in Spin-1 Models Realized with Ultracold Atoms	145
C	Calculation of the effective spin-1 model parameters	155
D	Spherical tensor identities	159
D.1	Spherical basis	159
D.2	Reduced matrix element	161
D.3	Polarizability	161

List of Figures

2-1	Experimental sequence for the production of a BEC	26
2-2	Laser beams propagating in the science chamber.	32
2-3	Examples of atom clouds affected by accidental interference fringes, as viewed from the vertical direction.	33
2-4	Ramsey coherence measurement before and after shimming residual magnetic gradient.	35
2-5	Effect of coil current ripple on the magnetic bias field.	36
2-6	Optical pumping during absorption imaging at weak imaging beam intensities.	39
3-1	Atomic level structure with and without spin -orbit coupling.	45
3-2	Ratio of vector shift to total light scattering rate.	50
3-3	Raman scattering rate vs. total scattering rate.	52
4-1	Comparison between Wannier and Bloch functions.	56
4-2	Plot of the state-dependent lattice potential and physical separation between different hyperfine states.	60
4-3	Polarization rotation control for state-dependent lattices.	61
4-4	Imbalance in the state-dependent lattice potential depth caused by a folding mirror.	64
4-5	The $\sigma^+ - \sigma^-$ scheme for state-dependent lattices.	66
5-1	Mean-field phase diagram of the Bose-Hubbard Hamiltonian.	76

5-2	Calculation of the average filling factor $\langle \hat{n} \rangle$ around the $n = 1$ and $n = 2$ Mott lobes, for $U/zt = 11$	78
5-3	Simulation of the Mott lobe populations in 3D $20 E_{R,1064 \text{ nm}}$ lattice	87
5-4	Perturbative calculation of correction to Hubbard interaction energy U due to inclusion of higher-band Wannier orbitals.	88
5-5	Perturbative calculation of correction to tunneling amplitude t due to inclusion of higher-band Wannier orbitals and the bond-charge effect.	89
6-1	Kinetic exchange mechanism in a two-component Mott insulator with filling factor $\langle \hat{n} \rangle = 2$	94
6-2	On-site anisotropy in a two-component Mott insulator with filling factor $\langle \hat{n} \rangle = 2$	94
6-3	Table of second-order matrix elements for a $\langle \hat{n} \rangle = 2$ Mott insulator.	98
6-4	Comparison of energy spectrum between the Bose-Hubbard model and the effective spin-1 model.	100
6-5	Magnetic phases of a ferromagnetic spin-1 chain	101
7-1	Measurement of local spin pairing by inducing spin-selective decay.	110
7-2	Variation of $-J$ and D with respect to the longitudinal lattice depth in a three-dimensional optical lattice.	112
7-3	Experimental sequence for the measurement of spin alignment and doublon fractions.	113
7-4	Coherent dynamics of the spin alignment A after a quench in D/J . Varying the hold time at characteristic lattice depths for both positive and negative values of D/J	117
7-5	Coherent spin oscillations in a two-site model.	118
7-6	Effect of magnetic gradient on a two-site spin-1 model.	120
7-7	Phase diagram of the spin-1 model	122
7-8	Demonstration of an increase in condensate fraction due to the spin entropy from spin dephasing.	123

7-9	Experimental sequence for the measurement of spin alignment after a ramp into a state-dependent lattice.	125
7-10	Measurement of spin pairing fraction as a function of $U_{ab}/U = 1 - D/U$.128	
7-11	Energy diagram of the spin-1 model augmented by a magnetic gradient term $\Delta \sum_i i S_{z,i}$	131
A-1	Objective as a perfect blackbox imaging system	139
A-2	Effect of vacuum window deformation on wavefront error.	143
A-3	An example vacuum viewport structure.	144

List of Tables

4.1	Comparison of LC and EOM performance	64
-----	--	----

Chapter 1

Introduction

The research topic considered in this thesis is at the intersection of three broad fields of study in physics: quantum simulation, atomic gases in optical lattices, and quantum magnetism. In this chapter I provide a brief and personal summary of the history of the experimental research performed within the rubidium lab. While the lab has worked on a variety of research topics, the study of quantum magnetism using ultracold atoms has been a long standing goal of the lab. The motivation for studying quantum magnetism is briefly explained. The chapter concludes with a structural outline of the thesis.

1.1 Quantum simulation and ultracold atoms

The field of ultracold quantum gases has seen a tremendous growth since the first realization of Bose-Einstein condensation in 1995 [1, 2] and the first realization of a degenerate Fermi gas in 1999 [3]. Within the next decade following the achievement of quantum degeneracy in atomic gases, researchers intensely studied the properties and the dynamics of quantum gases in various regimes of temperature and interaction strengths, developing new techniques, tools and data analysis methods to control and monitor quantum gases with more ease and precision [4, 5]. At the same time, it was recognized early that quantum gases themselves could be ingredients for building new and possibly more complex quantum systems and studying new quantum phenomena.

The origin of this idea dates back to Richard Feynman’s famous keynote speech in 1982, where he proposed using quantum-mechanical objects to build a quantum computer to simulate quantum mechanical laws of nature [6]. The first observation of the superfluid-Mott insulator transition, a quantum phase transition, in a Bose-Einstein condensate in an optical lattice in 2002 confirmed the enormous potential of cold atomic gases as a new platform for quantum simulations [7]. The interest and the excitement surrounding quantum simulations with ultracold quantum gases has only grown stronger in the following two decades.

1.2 Why quantum magnetism?

The history of quantum magnetism dates back to the early days of quantum mechanics, when Heisenberg and Dirac discovered the exchange interaction effects for indistinguishable particles [8, 9]. In that regard it is a rather old subject, but it still plays a central role in modern research topics such as quantum phase transitions [10] and quantum integrability [11]. It is also challenging to observe and study quantum magnetic phenomena because the associated energy scales are typically very small and hence require low temperature and entropy. On the other hand, the strict experimental requirements drive experimenters to improve their methods and come up with new ideas to construct quantum systems with extremely low entropy.

As a platform for studying quantum magnetism, ultracold atoms offer a distinct advantages compared to others such as solid crystals with magnetic ions. The internal level structures of atoms are relatively simple compared to those of molecules or chemical compounds, and thus are well-understood, especially for alkali atoms. This has helped experimenters develop a wide variety of techniques for preparing pure initial quantum states with external laser beams, RF/microwave pulses and/or magnetic fields. The initial states can be ground states that are relevant to the study of phase transitions between quantum magnetic phases, or they can be excited states¹ that are relevant to the study of non-equilibrium dynamics. The variety of initial states

¹Here I mean the excited states of a quantum spin model, not of an atom.

that can be prepared with ultracold atoms enables a wide range of experiments that probe different physics within the same model.

In this thesis, we consider both the ground state properties and the nonequilibrium dynamics of a spin-1 model. We study different ground states of a spin-1 model by using a state-dependent lattice - an optical lattice that provides different potential energy for different spin states of an atom - and tune the lattice to induce a phase transition from a magnetic ground state with an energy gap (“spin Mott”) to a ground state without an energy gap (“spin superfluid”). We also study how exchanges between spins occur in the presence of a magnetic anisotropy by initializing the system into a superposition of different spins and observing how pairing between different spins changes. It should be pointed out that the study of nonequilibrium physics is not something that we originally planned to do, but we had the freedom to quickly design an experiment to probe it and eventually observed some unexpected and interesting effects. This is an example of the power of quantum simulation with ultracold atoms; sometimes you make discoveries by simply “trying things out,” and having the freedom to do so is important.

1.3 Overview of research efforts in BEC4

The history of the rubidium lab in the Ketterle group, also known as BEC4, has followed a shift of interest from studying Bose-Einstein condensates themselves to using them as a tool. In the beginning, which was only a few years after the achievement of Bose-Einstein condensation was recognized with a Nobel Prize in physics in 2001, the lab contributed to a deeper understanding of superradiance in matter waves within the short probe time regime [12]. The research on the reaction of matter waves to external probe pulses continued for some time, until the lab took a major interest in studying spin physics in optical lattices, whose energy scale is very small and hence requires an extremely low entropy in the system. In 2009 the lab began its progress toward simulating spin physics in optical lattices by developing a new form of in-situ thermometry inside an optical lattice (spin gradient thermometry), which was capa-

ble of measuring temperature as low as 1 nK [13]. The lowest temperature measured was further reduced to 350 pK with the help of an adiabatic demagnetization cooling technique in 2011 [14]. While the experiments performed did not simulate a quantum spin Hamiltonian, they showed that quantum gases can be loaded to optical lattices and studied at a very low temperature associated with the magnetic exchange energy scale.

When I joined BEC4 as a young student with no previous experience of atomic physics in the fall of 2013, the lab was already exploring a new avenue in quantum simulation, which was the simulation of artificial gauge fields for neutral atoms in optical lattices [15], with hopes of studying quantum Hall physics with ultracold bosons. I was fortunate to join this research effort and to contribute to the observation of bosonic condensation in the presence of a large artificial gauge field [16]. During our efforts toward the artificial gauge field experiment, for which a tilted optical lattice was a key ingredient, we observed an interesting shielding of matter wave coherence lifetime (dubbed superfluid shielding) in a tilted optical lattice due to the interaction between a mobile spin component and an immobile spin component [17]. While I take pride in having made measurable contributions to both experiments, I will not elaborate on those experiments in this thesis as they have been thoroughly described in the PhD theses of Colin Kennedy [18] and William Cody Burton [19]. During this time I also had a chance to work on a laser frequency lock between a 532 nm and a 1596 nm source, which was supposed to generate an optical triple-well superlattice, which would have been useful for extending the experimental effort in the direction of artificial gauge fields. While this research plan was ultimately shelved, I had a valuable time learning about and characterizing laser frequency noise.

Soon after the conclusion of the superfluid shielding experiment, we finally set out to simulate the quantum Heisenberg spin-1 model following the early theoretical proposals ([20,21]) from 2003 and guided by a theoretical analysis of the spin-1 magnetic phase diagram in [22, 23]. We obtained some preliminary results on the realization of a spin Mott phase after installing the first working state-dependent optical lattice in our lab [18, 19], but at the time we did not find conclusive evidence that we were

probing the physics of magnetic exchange. At the same time, an amorphous idea of a new science chamber upgrade (on which I took the lead) fully developed into a plan for a new quantum gas microscope for the future, so that we would be able to probe off-site spin correlations in our simulated spin chains. As we kept working on the spin chain experiment and the microscope upgrade, we discovered many things in our old experimental setup that were not explained well previously or not appropriately adjusted. It was a frustrating experience to work on them one by one, but at the same time helped me improve and become confident in problem-solving skills.

At the conclusion of my prolonged doctoral studies, we finally found conclusive evidence of magnetic exchange within our simulated spin-1 chains and observed an interesting interplay between the magnetic exchange and the magnetic anisotropy within our spin chain, which we reported in [24]. Also, while we have stocked most of the ingredients to make the upgrade for a quantum gas microscope, we identified key issues in our imaging setup. This thesis focuses on how we realize a spin-1 chain in an optical lattice, and the troubleshooting we had to undertake to improve our experiment and our future upgrade for the quantum gas microscope. While it is unfortunate that so many of the insights to the problems arrived rather late in my career as a graduate student, I am glad that I discovered some of them and hope that the thesis serves as a useful guide for the future generation of students in BEC4.

1.4 Thesis outline

- Chapter 2 describes the current status of the BEC4 ^{87}Rb machine after many years of adjustments. It also gives some suggestions for further improvements.
- Chapter 3 describes the general theory of non-scalar light shift. Most of the material is from [25] but I tried to avoid the heavy machinery of spherical tensor algebra in the introduction to the theory. The focus is on motivating the notion of a non-scalar polarizability at a more intuitive level. This chapter is helpful for understanding how a state-dependent optical lattice works.

- Chapter 4 gives a short introduction to what an optical lattice is and gives a quick demonstration on how to compute the Wannier basis, which is important to calculating interaction parameters. The rest of the chapter discusses and analyzes the different realizations of a state-dependent optical lattice.
- Chapter 5 reviews the Bose-Hubbard Hamiltonian as a model for neutral atoms in optical lattices and gives a detailed description of how to simulate the mean-field distribution of the local occupancy number in the optical lattice. The simulation is important in understanding how we characterize our Mott insulator before using it as a background for simulating spin physics.
- Chapter 6 attempts to explain a specific quantum spin model, which is the quantum Heisenberg spin model, and discusses how it is realized with a two-component Bose gas in an optical lattice, which can be either state-independent or state-dependent. The chapter concludes with a discussion of experimental observables in the spin model.
- Chapter 7 describes the two experiments performed on the simulated spin-1 chain. The first experiment is a study of quench dynamics in the spin chain, where we observe an interesting interplay between spin exchange and spin anisotropy. The main result is also reported in [24], whose copy is available in Appendix B. The second experiment studies the properties of the spin Mott state and how it can be used as a starting point for adiabatic passages to different spin states with the help of a state-dependent lattice.
- Chapter 8 serves as the conclusion to the thesis and provides some scientific outlook for the study of spin models in doubly occupied Mott insulators.

Chapter 2

The BEC4 ^{87}Rb machine

The rubidium quantum gas setup was conceived and built in the early 2000's and has seen many repairs and upgrades. The setup consists of two chambers: the main chamber, where magneto-optical trapping (MOT) and magnetic trapping are used to produce a nearly degenerate rubidium cloud, and the science chamber, to which the cloud is transported for evaporation to Bose-Einstein condensate (BEC) and further manipulation. The design of the main chamber can be found in [26, 27] and that of the science chamber in [28]. In this chapter I will provide an up-to-date description of the setup and things to be improved for future experiments. The experimental sequence for the production of a BEC is summarized in Fig. 2-1.

2.1 MOT chamber

2.1.1 Optical setup

The optical setup for the MOT chamber remains similar to what is already described in [26]. It has been almost two decades since the creation of the first MOT inside the vacuum chamber, and operations inside the chamber work reasonably well to produce a nearly degenerate atom cloud within an acceptable experimental cycle time (approximately 27 s), but it is likely that the parameters have deviated from the optimal conditions.

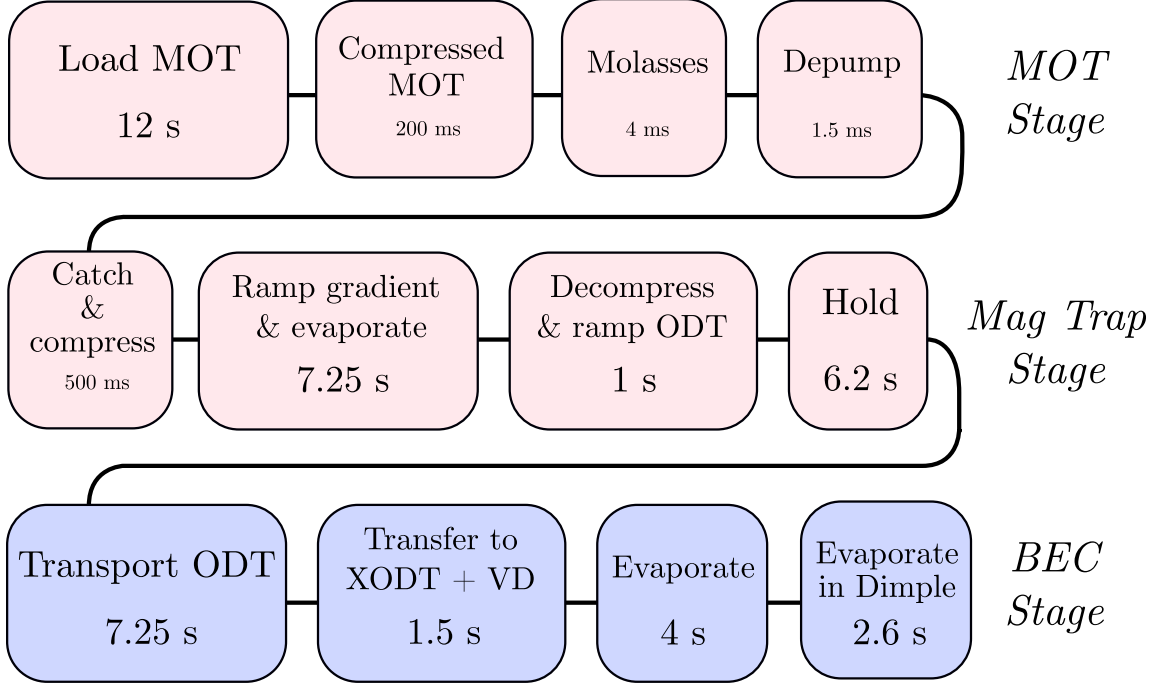


Figure 2-1: Experimental sequence for the production of a BEC. The steps with the light background take place inside the MOT chamber, whereas the steps with the dark background take place inside the science chamber.

The main cooling and trapping light power is derived from a frequency-doubled fiber laser (Quantel EYLSA780), which is set to output 800 mW out of 1000 mW maximum possible output. This high-power, turn-key system obviated the need for injection-locked slave diode lasers, which were prone to losing locks due to small mechanical shocks and temperature drifts. However, after five years of stable operation, the fiber laser began to frequently show problems that were usually not user-serviceable (internal monitoring photodiode losing efficiency, faulty voltage regulators, enhanced back-reflection of 1560 nm pump power). Based on this experience, a system of tapered amplifier (TA) seeded by an external cavity diode laser (ECDL) could still be a good option for a stable high-power source at 780 nm in the long run [29].

The fiber laser is locked to -2×93 MHz from the $D_2 F = 2 \rightarrow F' = 3$ transition of ^{87}Rb (also known as the cycling transition) via polarization rotation spectroscopy [30]. The fiber laser output is split into two separate paths, one for the MOT and one for the Zeeman slower. Each path consists of an acousto-optic modulator (AOM) in the

double-pass configuration. From the laser table we ultimately deliver 150 mW to the MOT optics and 30 mW to the Zeeman slower optics on the machine table. Despite the initial high power and good spatial mode quality of the fiber laser output, the ultimate power delivered to the atoms is substantially smaller than 800 mW due to limited diffraction efficiencies of AOMs in the double-pass configuration, limited fiber-coupling efficiencies (60 \sim 70%), and reflection losses through various beam cubes and lenses. It is suspected that transmission through the AOMs causes distortion to the spatial mode, possibly due to the smallness of the active aperture or thermal effects from RF carrier power. Note that the actual MOT power delivered to the atoms is also smaller than 150 mW due to losses during propagation through the optics.

The repumper beam is derived from an old TA (Toptica TA-100) seeded by an ECDL (Toptica DL-100). The ECDL is locked to +80 MHz from the D_2 $F = 1 \rightarrow F' = 0/1$ crossover transition. The reason for locking to a crossover transition is that it displays the strongest anisotropy in the polarization rotation signal for lower hyperfine states ($F = 1$ for ^{87}Rb), where the optical pumping dynamics is more complicated than the upper hyperfine states ($F = 2$) [30]. In the original setup as described in [26], the ECDL was supposed to be locked to -80 MHz from the D_2 $F = 1 \rightarrow F' = 1$ transition. We have double-checked that the current locking point is indeed the crossover transition by comparing to the saturated absorption signal and also by measuring the frequency with a high-resolution wavemeter¹. The MOT repumper beam is then expected to be -33 MHz from the $F = 1 \rightarrow F' = 2$ transition, after passing through an AOM. We have not checked whether the Zeeman slower and MOT performances are optimal with the current frequency lock point, so this is one parameter that can be tweaked in a general optimization search. We deliver a total of 12 mW to the MOT repumper, and 4 mW to the slower repumper.

¹We realized this fact about the repumper locking point around the end of September 2020, which is only half a year before the time of this writing.

2.1.2 MOT loading and molasses

The MOT beams also function as $\sigma^+ - \sigma^-$ type polarization gradient cooling beams during the 4 ms optical molasses stage that succeeds the MOT loading. Due to the design of the Zeeman slower, there is a fraction of the background bias field for the Zeeman slower that is present during the MOT loading, but absent during the molasses stage. The MOT cloud shifts visibly in position when the current to the Zeeman slower is switched off, so this makes the beam alignment optimization of the MOT/molasses beams tricky. Note that the residual field cannot be left on during the molasses as this will degrade the optical molasses performance [31]. Over the course of the doctoral studies described here, we only had to re-align the MOT/molasses beams a handful of times, such as when water from the magnetic coil cooling line sprayed onto the optics, or when one of the beams got slightly misaligned after stepping on the 80/20 structures and replacing the ^{87}Rb ampoule in the oven. Due to a current lack of appropriate imaging setup for a time-of-flight imaging in the MOT chamber, we optimized the loading by monitoring the final number of atoms left in the optical dipole trap after evaporative cooling in the magnetic trap. In contrast to the sequence described in [26,27], neither the intensity of the molasses beam or the repumper beam is adjusted during the compressed MOT and the molasses stage.

2.1.3 Loading of the atom cloud to the magnetic trap

In the original setup there used to be a $F = 2 \rightarrow F' = 2$ depumper beam that optically pumps atoms into the $F = 1$ manifold after the molasses step and before loading to the magnetic trap. It turned out that what was labeled as a depumper was not causing any effect; the depumping process relied on the small off-resonant scattering from the $F = 2 \rightarrow F' = 2$ transition by the molasses beam, which takes 2 ms to complete. After the depumping, the atom cloud is loaded into the magnetic trap, first by forming a weak spherical trap to mode-match the density distribution of the atom cloud and then transforming into a cigar-shaped trap with a very high gradient in the radial direction. This “catch-and-compress” step is crucial and needs

to be well-optimized. We found that a suboptimal step leads to a noticeably lower atom number in the optical dipole trap before the transport to the science chamber. Prior to this step, the capacitors of the high-current power supplies are fully charged, and provide a fast rush of current to the magnetic trap once the insulated-gate bipolar transistor (IGBT) switches are closed. It was empirically found that slightly delaying the rapid switch-on of the “axial” power supply (which pushes current to the curvature and anti-bias coils in our cloverleaf magnetic trap) while the “squeeze” power supply (which pushes current to the curvature coil only) rapidly turns on yields the most number of atoms caught. A plausible explanation is that the initial absence of current in the anti-bias coil makes sure that the radial gradient is not too strong compared to the axial gradient.

2.1.4 Forced RF evaporation in the magnetic trap

One of the previous lab members (Colin Kennedy) found out that we could push current (527 A) into the radial coils beyond the nominal rating of the power supply (500 A), helping us achieve a tighter magnetic trap and a faster evaporation. The evaporation in the magnetic trap now takes 7 seconds and probably does not need further optimization at this point.

2.1.5 Transfer to the transport optical dipole trap

Ideally, the optical dipole trap beam that transports the atom cloud from the MOT chamber to the science chamber is aligned simultaneously to the center of the magnetic trap and to the crossing of the laser beams that define the dipole trap in the science chamber. However, that cannot be satisfied in general. Because the optical transport is done by moving a single lens and thereby moving the focus of the dipole trap beam, alignment at one focal position fixes the alignment at other focal positions. If we treat the moving lens as an ideal lens, the angle at which the laser beam hits the lens determines the position on the focal plane, and the angle is fixed. We discovered that our current center of alignment for our lattice beams and the objective in the science

chamber constrains the position of the optical transport beam to be $\approx 500\mu\text{m}$ below the magnetic trap. The transfer from the magnetic trap to the optical trap is done by weakening the magnetic gradient and letting the cloud sag down due to gravity. However, this also reduces the trapping frequencies, such that the confinement along the axis of the transport beam does not enjoy enhancement by the magnetic trap, and this prolongs the required transfer time. We currently have to wait 6 s to completely fill up the dipole trap volume in the sagged trap position. If we shim the magnetic field to move the magnetic trap center down, we can reduce the transfer time to less than 1 s. Given the strength of the peak gradient (250 G/cm), we need 12 G of extra shim field along the transport axis.

An unsolved problem in the optical transport is the appearance of $|F = 1, m_F = 0\rangle$ impurities within the originally pure $|F = 1, m_F = -1\rangle$ cloud as the atoms get transported from the MOT chamber to the science chamber. It is suspected that this diabatic transition happens somewhere in the connection (gate valve) between the two chambers; we remove the impurities in the science chamber by flipping them to $|F = 2, m_F = 0\rangle$ and blowing them out with a resonant light pulse.

2.2 Old science chamber

2.2.1 Optical setup for dipole traps

The optical transport beam (“ODT”) moves the nearly-degenerate atom cloud roughly 38 cm with 80% single-pass transfer efficiency over 3 seconds. The atom cloud is transferred from the ODT beam to a crossed dipole trap [see Fig. 2-2(a)]. Previously, the crossed dipole trap was formed by a beam anti-parallel to the transport beam (“anti-ODT”) and a beam perpendicular to the transport beam (“XODT”) [28]. Now it is formed by a highly elliptical XODT beam from the side, and a vertical dipole beam (“VD”) along the gravity direction. Both beams are derived from an externally seeded 1064 nm fiber amplifier. The XODT beam has a $1/e^2$ beam waist that is roughly $(w_x, w_y) = (500 \mu\text{m}, 50 \mu\text{m})$ at the center of the trap and provides levitation against

gravitational sag. The VD beam has a $1/e^2$ beam waist of $95\ \mu\text{m}$ and provides radial confinement when viewed from the top. A precise control of the tilt of the XODT beam allows us to null projected optical gradient along the axis of the beam and levitate the atom cloud optically without horizontal drift². The absence of horizontal gradients while holding the atom cloud with just the XODT beam allows us to align the horizontal directions of lattice beams by monitoring the displacement of the in-trap position of the atom cloud. To control the atom number, we introduce a tightly focused beam (“Dimple”) that keeps a desired number of atoms while a high magnetic gradient in a horizontal direction kicks out the remaining number of atoms. The Dimple beam is derived from a temporally incoherent light source (superluminescent diode, Superlum M-S-850) with its center wavelength around 850 nm. The temporal incoherence minimizes occurrences of interference fringes and helps achieve a tight focal spot.

2.2.2 Optical setup for optical lattices

The three-dimensional optical lattice is generated by propagating three independent laser beams in three orthogonal directions and then retroreflecting them. The directions for the horizontal lattice beams are marked “Closet” and “Tool”, which are roughly -45° and $+45^\circ$ rotated from the direction of the XODT beam [see Fig. 2-2(b)]. The wavelength of the Vertical and Closet lattice beams is 1064 nm (Nufern fiber amplifier) while that of the Tool beam can be either 1064 nm (from the same fiber amplifier that provides power for Vertical and Closet beams) or 810 nm (from a Ti:Sapphire laser), depending on the experiment being performed. For every lattice beam, we have a set of two photodiodes that receive some light from a beam sampler and are used for feedback stabilization and monitoring of the optical power output³. After the beam sampler, an optical isolator is placed so that the retroreflected light

²Since the gravitational force is equivalent to $2130\ \text{Hz}/\mu\text{m}$ for ^{87}Rb , a 1° tilt results in a projected gradient of $37\ \text{Hz}/\mu\text{m}$, which becomes noticeable at small radial trapping frequencies.

³The second photodiode for monitoring serves to measure out-of-loop intensity noise. The closed feedback loop suppresses shot noise seen by the feedback photodiode, so an independent measurement of the output power is needed to see the true noise level of the output light.

does not reflect off the optical fiber tip and reach the photodiodes, introducing noise in the process⁴. It has been found out that such backreflection is deleterious for the stabilization of the optical lattice intensity at acoustic frequency range [18].

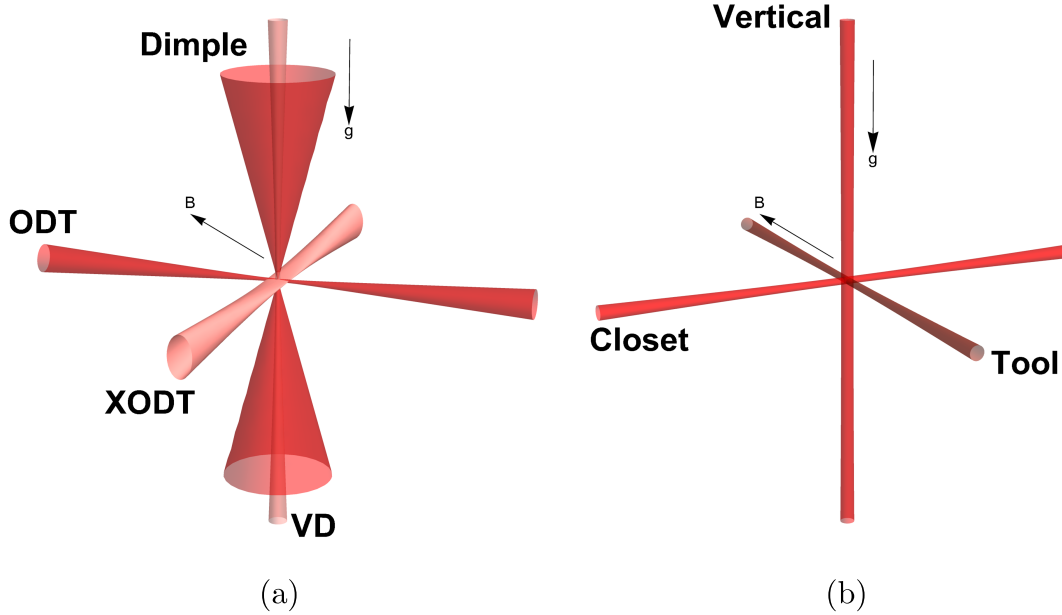


Figure 2-2: Laser beams propagating in the science chamber. The arrow labeled “g” denotes the gravity direction. The arrow labeled “B” denotes the bias magnetic field direction. The beam labels are attached to the side where the beam is launched. (a) Optical dipole trap beams. For the two vertical beams, the low-divergence beam is the VD beam and the high-divergence beam is the Dimple beam. The VD beam forms a crossed optical dipole trap with the XODT beam that traps the BEC. All beams except the Dimple have a wavelength of 1064 nm. The Dimple beam is derived from a temporally incoherent source with a center wavelength of 850 nm and a coherence length of $\mathcal{O}(10 \mu\text{m})$. (b) Optical lattice beams. The wavelength of the Tool beam can be either 1064 nm or 810 nm.

2.2.3 Mitigation of interference fringes

Over the years, a recurrent problem in the optical setup around the science chamber was the unintentional formation of interference fringes. Because of the extremely high coherence length of the lasers being used (e.g. 300 km for our 1064 nm master

⁴Such a problem was described by Markus Greiner at a CUA winter retreat. I later found out the problem in our setup by noticing a small but visible difference in the oscilloscope trace of the photodiode while I blocked and unblocked the retroreflecting mirror.

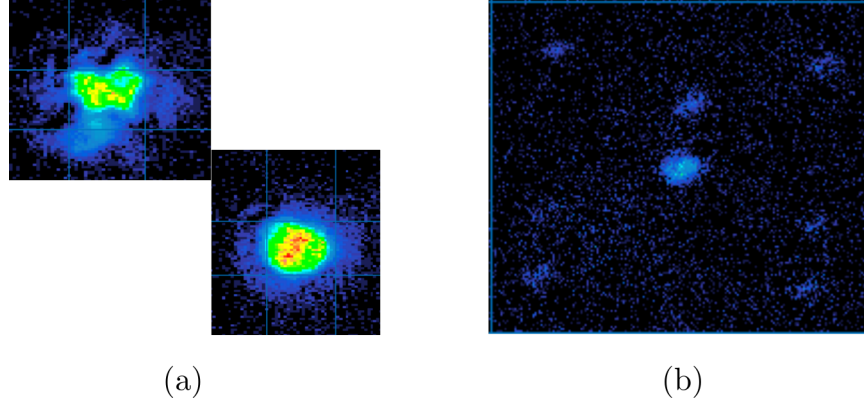


Figure 2-3: Examples of atom clouds accidental interference fringes, as viewed from the vertical direction. (a) Fringes formed by Vertical lattice beam input and a back-reflection of a backreflection (double backreflection) from a lens. The two images show in-trap atomic density profiles with and without fringes. (b) Fringes formed by the XODT beam and a backreflection from a vacuum window. A ghost diffraction peak along the XODT axis is visible.

laser Coherent Mephisto), it is easy to form accidental fringes if there are many surfaces or if the laser beams are not angled sufficiently away from normal incidence. Due to anti-reflection coatings, the reflected power will usually be 1% or less, but constructive interference in amplitude with the incident beam will result in up to $\pm 20\%$ spatial modulation of the original optical intensity. If the length scale of the modulation is large enough to be resolved by the imaging system and the atomic gas is degenerate and in the Thomas-Fermi regime, the corrugation in the potential can be seen directly in an in-trap image of the atom cloud [Fig. 2-3(a)]. If the length scale is too short to be resolved, but the modulation depth is sufficiently high, it may leave detectable “ghost” diffraction peaks in a time-of-flight image [Fig. 2-3(b)]. The corrugation in the potential can be dynamic if the optical elements vibrate at acoustic frequencies and it can possibly heat the atom cloud while ramping up optical lattices. In general, it is advised that the laser beams are angled by 1° or more with respect to surfaces/windows/flats, depending on the beam divergence and power.

2.2.4 Magnetic field control

The magnetic coils around the science chamber are described in [28]. The bias magnetic field is set to be roughly parallel to the Tool beam, which generates the spin-dependent lattice in our experiments. The residual gradients are shimmed by flowing extra current in one of two coils in each of the Tool coil pair and the Closet coil pair. The extra bias generated from this shimming contributes 3 G in quadrature to 8 G generated by the Tool coil pair, resulting in a net bias field of ~ 9 G which is slightly tilted away from the Tool lattice beam direction. We check the quality of the gradient shimming by performing a Ramsey interferometry measurement on the $|F = 1, m_F = -1\rangle \rightarrow |F = 2, m_F = -2\rangle$ transition (see Fig. 2-4).

The biggest source of noise in the magnetic field is from the ripple current of the Tool coil power supply (Agilent 6651A) that runs at a superposition of harmonics of the mains frequency (Fig. 2-5). The RMS ripple current according to the datasheet is 25 mA and it results in a 8.8 mG ripple in the bias. In principle, this bias ripple can be nulled by connecting a feedforward shunt running out of phase with respect to the mains line [32]. However, we have left the bias ripple uncompensated and simply switch on the RF or microwave power on a mains line trigger when performing spin flips. Besides current noise, ferromagnetic components around the chamber can have a hysteretic effect on the bias field. Applying large horizontal gradients requires running $\mathcal{O}(100$ A) through our coils, and we measured that the bias changes by $\mathcal{O}(100$ mG) after a large gradient was ramped up and down. This bias change is semi-permanent in the sense that subsequent experiment cycles without a gradient ramp show a similar bias change that decays slowly, ruling out the possibility of the change being induced by eddy currents. It is likely that there are some ferromagnetic domains within the science chamber or some nearby bolts, so it is advised that a new chamber is checked for magnetic hysteresis before the final assembly.

A nuisance of the current magnetic field control is the lack of Earth's-field-canceling coil pairs. At a low bias field (< 2 G), which is required for efficient optical pumping during imaging, the Earth's magnetic field (≈ 0.5 G) interferes with the field strength

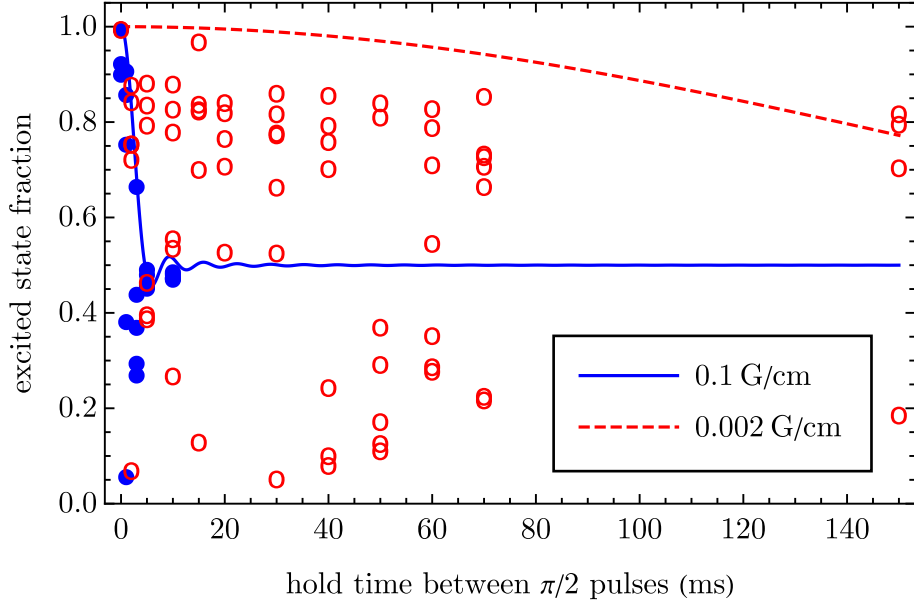


Figure 2-4: Ramsey coherence measurement before and after shimming residual magnetic gradient. The transition used is $|F = 1, m_F = -1\rangle \rightarrow |F = 2, m_F = -2\rangle$ at the bias field of 8.916 G (transition frequency $\omega_0 = 2\pi \times 6815.962$ MHz). During the measurement, the atom cloud is held in a crossed optical dipole trap with no lattices, so some motion-induced averaging of the gradient by the atoms might have occurred. The blue solid dots and the red open dots correspond to data obtained before and after shimming, respectively. The blue solid line and the red dashed line correspond to fit models with estimated gradient values before and after shimming, respectively. The fit models are based on the averaged values of $\cos(\pi t \delta)^2$ over a spherical volume in which a linear gradient runs along the z -axis. We assume the extent of the cloud is $10 \mu\text{m}$. The scattering of the raw data away from the fit function envelopes is due to the uncompensated bias fluctuations at the harmonics of mains frequency (Fig. 2-5), which can add extra rotation by π or more during the hold time. If the AC line trigger is set such that the average of the bias deviation over a ripple period is zero, and the hold times are exactly integer multiples of the ripple period, we expect the scattering to disappear.

$$\Omega_{|1,-1\rangle \rightarrow |2,-2\rangle} = 2\pi \times 28.63 \text{ kHz}$$

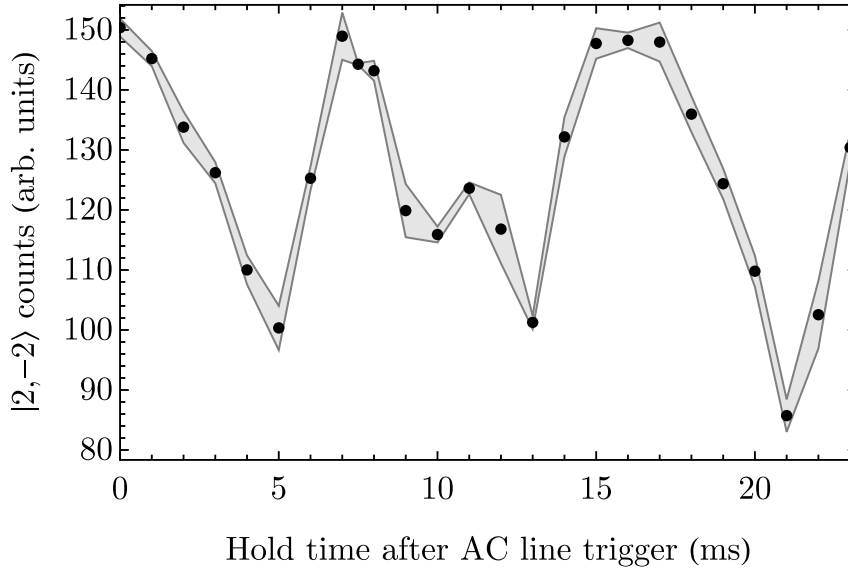


Figure 2-5: Effect of coil current ripple on the magnetic bias field. A π -pulse addressing the $|1, -1\rangle \rightarrow |2, -2\rangle$ transition is applied to a $|1, -1\rangle$ BEC after a variable hold time with respect to the AC line trigger edge. The gray band denotes the \pm -standard error of the mean of the $|2, -2\rangle$ atom number measurements. The power supply providing most of the bias field is Agilent 6651A, which has a 25 mA current ripple. The specified current ripple is estimated to produce an amplitude of 8.8 mG in bias fluctuation at harmonics of the mains frequency. The estimated maximum detuning of the transition is 0.65Ω , where $\Omega = 2\pi \times 28.63$ kHz is the Rabi frequency of the transition. The estimated maximal detuning corresponds to a maximal bias deviation of 8.9 mG.

and orientation control. Something as modest as wrapping flexible wires multiple times around the vacuum chamber and flowing a small current through them should compensate the Earth’s magnetic field⁵.

2.2.5 Atom number calibration

Absorption imaging

Absorption imaging measures integrated column density nl of the atom cloud, and it requires a precise knowledge of the effective absorption cross section σ_{abs} to convert the integrated column density into the observed atom number in an image. The formula for the total atom number N_{atoms} is

$$\begin{aligned} N_{\text{atoms}} &= \frac{1}{\sigma_{\text{abs}}} \int (n\sigma l) dA = \frac{A_{\text{pixel}}}{\sigma_{\text{abs}}} \sum_{\text{pixels}} (n\sigma_{\text{abs}} l) = -\frac{A_{\text{pixel}}}{\sigma_{\text{abs}}} \sum_{\text{pixels}} \log \left(\frac{I_{PWA}}{I_{PWOA}} \right) \\ &= \frac{A_{\text{pixel}}}{\sigma_{\text{abs}}} (\text{Ncount}) \end{aligned}$$

where I_{PWA} and I_{PWOA} denote pixel values of the picture-with-atoms image and the picture-without-atoms images respectively. The effective absorption cross section will reach the ideal value of $\sigma_0 = 3\lambda^2/(2\pi)$ only if the imaging is performed on the cycling transition, the imaging beam polarization is of a pure circular polarization, and the imaging intensity is far below the saturation intensity, which is 1.67 mW/cm² for the D_2 cycling transition [33]. For best results, there should be a small homogeneous bias to fix the quantization axis. We currently flow a small current in one of the Closet coils to establish an imaging bias field.

The cleanliness of the imaging beam polarization beam can be checked by imaging atom clouds prepared in different hyperfine states (e.g. $|F = 2, m_F = 0, -1, -2\rangle$) but under otherwise same conditions, and comparing the ratios of the absorption signals to the ratios of the transition strengths [see Fig. 2-6(b)], which are given by squares of Clebsch-Gordan coefficients for respective transitions [34]. Note that such

⁵As for why this has not been done, it is difficult to wrap anything around the chamber, especially the bottom side, due to the proximity of the optical breadboards and RF/microwave antennae.

measurements should be done at a very low imaging beam intensity and with short exposures to prevent optical pumping. A CCD camera in a low-noise readout mode and with hardware pixel binning enabled should be able to detect such low signals.

For an accurate count of the atom numbers, it is best to keep the peak optical density (OD) well below 1. We have seen that the same atom cloud will register a lower total count if it does not expand enough during time-of-flight and hence has a higher optical density. A detailed look at the evolution of the absorption signals during imaging is provided for two different ranges of OD in Fig. 2-6. We suspect that at high optical densities, re-absorption of spontaneously emitted photons becomes non-negligible and provides a small optical pumping out of the stretched state, lowering the effective absorption cross section.

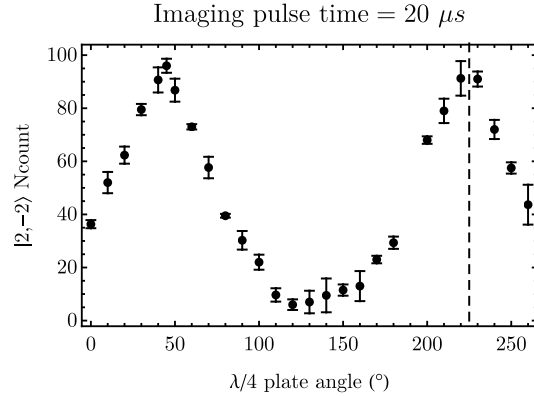
BEC expansion

An atom number calibration method that does not rely on a precise knowledge of the effective absorption cross section is the measurement of cloud widths as a BEC expands during time of flight. Instead, it requires a precise knowledge of the trapping parameters and the velocities at which the cloud expands. The method also assumes that the BEC is trapped in a harmonic trap and is deep in the Thomas-Fermi regime. In the Thomas-Fermi regime, when the harmonic trap is abruptly switched off, the total energy released is dominated by the mean-field interaction energy, which is converted into the kinetic energy of the expanding atom cloud [35]. Also, in this regime the density distribution is expected to maintain its initial parabolic shape during the expansion [36], so that the time-dependent density distribution can be written as

$$n(x, y, z, t) = n_0(t) \left(1 - \frac{x^2}{R_x^2(t)} - \frac{y^2}{R_y^2(t)} - \frac{z^2}{R_z^2(t)} \right) \quad (i \leq R_i(t), i \in \{x, y, z\})$$

where $R_x(0), R_y(0), R_z(0)$ correspond to the initial Thomas-Fermi radii of the cloud and $n_0(0)$ is the initial peak density. Note that the expression holds only where $n \geq 0$.

(a)



(b)

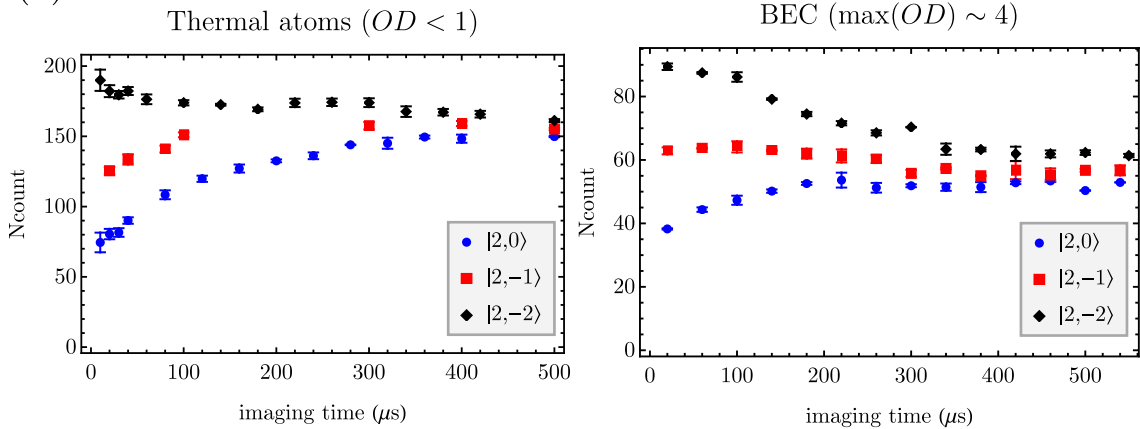


Figure 2-6: Optical pumping during absorption imaging at weak imaging beam intensities. A pulse time of $20 \mu\text{s}$ corresponds to roughly one photon absorbed per atom. The imaging bias is around 2 G. (a) Calibration of the imaging beam polarization. A linear polarizer (Thorlabs NIR100) and a quarter-wave plate are installed before the vacuum chamber. A maximal absorption by $|2, -2\rangle$ atoms is achieved when the polarization is σ^- . The non-sinusoidal behavior is possibly due to a birefringent effect from the vacuum window. After modeling the vacuum window as a fixed retarder at some angle and fitting the model to the data, we estimate that the maximum absolute value of the circularity of the input polarization is around 0.9, which is close to the maximum value of one. We set the quarter-wave plate at the angle specified by the dashed line. (b) Optical pumping dynamics at different optical densities. The ratios of the early-time absorption signals agree nicely with the ratios of the relative line strengths, which are (24,40,60) for the $\Delta m_F = -1$ transitions from $|F = 2, m_F = 0, -1, -2\rangle$ [34]. However, we see a noticeable decay of the signal for $|2, -2\rangle$ at high optical densities, whereas it stays relatively flat for low optical densities. We suspect there is a small optical pumping rate out of $|2, -2\rangle$ at high optical densities due to reabsorption of spontaneously emitted photons, which is to be expected at high OD .

From this we can derive that the observed kinetic energy of the expansion E_{rel} is

$$E_{\text{rel}} = \frac{8\pi}{105} \frac{m}{2} v_b^2 n_0(t) R_x(t) R_y(t) R_z(t)$$

where m is the mass of a single atom and $v_b = \sqrt{R_x^2 + R_y^2 + R_z^2}/t$ is proportional to the root mean square of the expansion velocity of the cloud boundaries. On the other hand, the total mean-field energy E_{int} of a trapped cloud is

$$E_{\text{int}} = \frac{16\pi}{105} g n_0(0)^2 [R_x(0) R_y(0) R_z(0)]$$

where $g = 4\pi\hbar^2 a_s/m$ and a_s is the s -wave scattering length. If we set $E_{\text{rel}} = E_{\text{int}}$, we obtain

$$N_{\text{atoms}} = \frac{\sqrt{2}}{120} \frac{m^2}{\hbar^2 a_s} \frac{v_b^5}{\omega_x \omega_y \omega_z}$$

where $\omega_{x,y,z}$ are the angular trapping frequencies in the x, y and z directions, which can be measured accurately with induced dipole oscillations after kicking the atom cloud in the trap. Because the expression contains a fifth power of v_b and hence is sensitive to its precise value, long times of flight should be used to measure v_b . For ^{87}Rb , $m = 86.9$ u and $a_s = 100 a_0$, where $a_0 = 5.29 \times 10^{-11}$ m is the Bohr radius, so for $(\omega_x \omega_y \omega_z)^{1/3} = 2\pi \times 40$ Hz, $v_b = 2.5$ mm/s yields $N_{\text{atoms}} = 25650$, while $v_b = 2.8$ mm/s yields $N_{\text{atoms}} = 45200$. We have checked that this method agrees nicely with perturbative absorption imaging performed on the stretched state $|F = 2, m_F = -2\rangle$ prepared with the cleanest imaging beam polarization possible.

Chapter 3

Non-scalar Light Shift

Understanding the non-scalar or state-dependent light shift is crucial for many applications. For example, when atoms are used as qubits and stored in tightly-focused beams, the electric field can have a non-zero longitudinal polarization near the focus and give rise to an inhomogeneous state-dependent potential that dephases any internal state superposition unless it is suppressed by an orthogonal and real magnetic field [37, 38].

On the other hand, a state-dependent potential can be used as a beneficial tool for state preparation and manipulation of cold atoms. There have been numerous experimental works using state-dependent potentials in different platforms, such as optical nanofiber traps [39] and optical lattices [40–42]. Our quantum simulation experiment also makes a prominent use of state-dependent lattice potential. In this chapter we give a brief review of the theory of non-scalar light shift.

3.1 Classical explanation of light shift

In this section, we neglect the details of the internal structure of an atom, and concentrate on how atoms interact with a polarized light in general. Atoms can be thought of as miniature dielectric objects. They can be polarized by external electric fields, and hence they experience an energy shift due to the interaction between the induced dipole moment and the external electric field. If the external field is sufficiently small,

a linear relationship between the induced dipole moment \vec{d} and external field \vec{E} holds: $\vec{d}(\omega) = \alpha(\omega)\vec{E}(\omega)$, where the transfer function $\alpha(\omega)$ is called the polarizability of the atom. The argument of ω in the relationship denotes that the terms are functions of frequency. Note that $\alpha(\omega)$ and $\vec{E}(\omega)$ are complex in general. For a fixed frequency ω , complex $\vec{E}(\omega)$ is related to the real electric field $\mathbf{E}(t)$ as $\vec{E}(\omega)e^{-i\omega t} + \text{c.c}$ where c.c stands for complex conjugate and to its time-averaged intensity I as $2\varepsilon_0 c |\vec{E}(\omega)|^2$ where ε_0 is the vacuum permittivity.

The energy of a real dipole moment \mathbf{d} in a real electric field \mathbf{E} is $-\mathbf{d} \cdot \mathbf{E}$. Because the dipole moment of an atom is induced from zero to its final value as the external field is switched on, the net energy shift that an atom experiences under the field is

$$U = -\frac{1}{2} \langle \mathbf{d} \cdot \mathbf{E} \rangle = -\text{Re}[\alpha(\omega)] |\vec{E}(\omega)|^2 = -\frac{1}{2\varepsilon_0 c} \text{Re}[\alpha(\omega)] I \quad (3.1)$$

where the angle brackets denote time-averaging.

We see that the light shift is proportional to the intensity of the laser but is not dependent on its polarization. To allow such dependence, we have to generalize the complex polarizability $\alpha(\omega)$ from a scalar to a rank-2 tensor $\alpha(\omega)_{ij}$, ($i, j = x, y, z$) so that the light shift is expressed as $-\sum_{i,j} \text{Re}[\alpha_{ij}(\omega) E_i(\omega)^* E_j(\omega)]$. We suppress the summation symbol in the discussions to follow.

We can make use of rotational symmetry to decompose that expression into a series of terms, one of which couples to intensity only (the scalar term), and others that have additional couplings to polarization. Any rank-2 tensor can be decomposed into three irreducible tensors that respect rotational symmetry:

$$\begin{aligned} \alpha_{ij} &= \alpha_{ij}^{(0)} + \alpha_{ij}^{(1)} + \alpha_{ij}^{(2)} \\ \alpha_{ij}^{(0)} &= \frac{1}{3} \alpha_{kk} \delta_{ij} \\ \alpha_{ij}^{(1)} &= \frac{1}{2} (\alpha_{ij} - \alpha_{ji}) = \frac{1}{2} \varepsilon_{kij} (\varepsilon_{kab} \alpha_{ab}) \\ \alpha_{ij}^{(2)} &= \frac{1}{2} (\alpha_{ij} + \alpha_{ji}) - \frac{1}{3} \alpha_{kk} \delta_{ij} \end{aligned}$$

The superscripts (0), (1), and (2) on the three irreducible tensors mean that they

transform as a scalar, a vector and a (symmetric and trace-less) tensor respectively under rotation. They have 1, 3, and 5 degrees of freedom respectively¹, which sum up to the total of 9 as expected for a general rank-2 tensor. The tensor ε_{ijk} is the Levi-Civita symbol² and δ_{ij} is the Kronecker delta function. Following the same approach, the tensor $E_i^* E_j$ can be decomposed into scalar, vector, and tensor parts:

$$\begin{aligned} E_i^* E_j &= (E_i^* E_j)^{(0)} + (E_i^* E_j)^{(1)} + (E_i^* E_j)^{(2)} \\ (E_i^* E_j)^{(0)} &= \frac{|\vec{E}|^2}{3} \delta_{ij} \\ (E_i^* E_j)^{(1)} &= \frac{1}{2} \varepsilon_{ijk} (\vec{E}^* \times \vec{E})_k \\ (E_i^* E_j)^{(2)} &= \frac{1}{2} \left(E_i^* E_j + E_j^* E_i - \frac{2}{3} |\vec{E}|^2 \delta_{ij} \right) \end{aligned}$$

If we combine the decompositions for α_{ij} and $E_i^* E_j$ together by taking their product, it is not difficult to see that the scalar part of α_{ij} couples to the scalar part of $E_i^* E_j$ only and so on: $\alpha_{ij} E_i^* E_j = \sum_{k=0}^2 \alpha_{ij}^{(k)} (E_i^* E_j)^{(k)}$. This decomposition principle looks slightly different in the spherical basis, due to the transformation between the Cartesian basis and the spherical basis (see Appendix D).

We see that the vectorial and tensorial components of the polarizability couples to the polarization of the laser as well as its intensity. In particular, the vectorial part is proportional to the circularity of the light \mathcal{A} , where \mathcal{A} is defined as

$$\hat{\epsilon}^* \times \hat{\epsilon} = i\mathcal{A}\hat{k}$$

where $\hat{\epsilon}$ is the complex polarization of the laser and \hat{k} is the propagation direction of the laser. For linear polarization, \mathcal{A} is zero, while circular polarizations $\sigma_+ = (-\hat{x} - i\hat{y})/\sqrt{2}$ and $\sigma_- = (\hat{x} - i\hat{y})/\sqrt{2}$ have values of +1 and -1 respectively for \mathcal{A} .

Just as the vectorial part of $E_i^* E_j$ is proportional to the circularity of the po-

¹In fact, these degrees of freedom correspond to those of spherical tensors with rank $J = 0, 1, 2$ respectively. We have chosen to express the tensor components in the Cartesian basis, but one may as well express them in the spherical basis, which will facilitate evaluations of expectation values with respect to angular momentum eigenstates.

²A useful identity is $\varepsilon_{kij}\varepsilon_{kab} = \delta_{ia}\delta_{jb} - \delta_{ja}\delta_{ib}$.

larization, the vectorial part of the polarizability tensor α_{ij} carries some notion of handedness as well. We will see that this is related to the projection of the electron angular momentum to the wavevector of the light. Intuitively, one needs a non-zero angular momentum to have some anisotropy in the response of the atom to the external electric field.

3.2 Anisotropy in atomic structure

Before we delve into the details of the quantum-mechanical calculation of the atomic polarizability tensor, it is instructive to consider how changes in the atomic level structures will lead to changes in the anisotropy of the polarizability. First consider the atomic structure that arises from the kinetic energy of the electron and the Coulomb potential, $p^2/2m + V(r)$. This Hamiltonian has eigenstates that are labeled by the orbital angular momentum L and for alkali atoms the ground state is $L = 0$, for which the atom-light coupling is isotropic [Fig. 3-1(a)]. The coupling is isotropic in the sense that the transition strength is independent of the polarization of the light field. If spin-orbit coupling ($A\vec{L}\cdot\vec{S}$) between the electron spin S and the electron orbital angular momentum L is switched on, the new eigenstates are labeled by the total electron angular momentum $\vec{J} = \vec{L} + \vec{S}$, and the excited states before the switch-on ($L' = 1$) now splits into a fine structure of two J' manifolds (also known as the D lines in alkali spectroscopy). The non-zero angular momentum of the ground state gives rise to an anisotropic atom-light coupling [Fig. 3-1(b)].

For atoms with zero orbital angular momentum in the ground state, the strength of the anisotropic atom-light coupling depends on the detuning of the laser frequency from the center of the D lines. If the laser detuning Δ_L is much larger than the fine-structure splitting Δ_{FS} , then in the rotating frame of the laser, the spin-orbit coupling term that gives rise to Δ_{FS} appears as a small off-diagonal perturbation in comparison to the large diagonal energy term of Δ_L . Colloquially we say that the highly-detuned laser cannot “resolve” the fine structure of the atom. Hence, the system can be approximated as an isotropic system in the large detuning limit [Fig. 3-

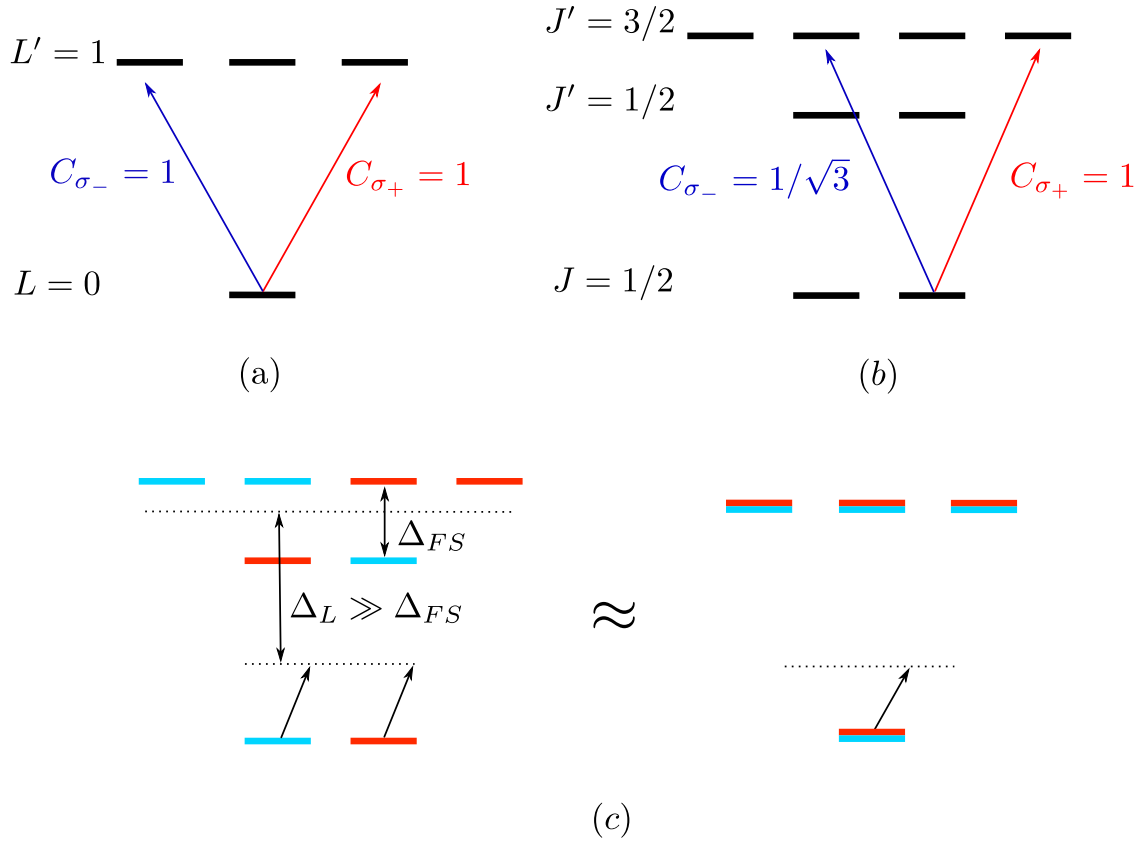


Figure 3-1: (a) Atomic level structure without spin-orbit coupling. Because the ground state has zero angular momentum ($L = 0$), its coupling to the excited states ($L' = 1$) is isotropic (it has equal Clebsch-Gordan coefficients C_ϵ for any polarization \hat{e} of the electric field). (b) Atomic level structure with spin-orbit coupling. Each state is labeled by the total electron angular momentum J , which is non-zero for both ground and excited states. Coupling from the ground state to the excited states is no longer isotropic. (c) If the laser detuning Δ_L is much larger than the fine-structure splitting Δ_{FS} due to the spin-orbit coupling interaction, the anisotropy cannot be resolved and the system approximates an isotropic system. The light-red and light-blue coloring of the states denotes the spin component with a higher weight within the total angular momentum state (light-red and light-blue refer to spin up and down, respectively).

1(c)].

In general, light shift scales as $1/\Delta_L$ and light scattering rate as $1/\Delta_L^2$. However, the vector light shift for states with zero orbital angular momentum scales with Δ_{FS}/Δ_L^2 [43] so that, asymptotically, the ratio of the vector light shift to the total light scattering rate becomes independent of the detuning. However, such an argument does not apply to states with non-zero orbital angular momentum. An example is a hypothetical four-level system consisting of $|L = 1, m_L = -1, 0, 1\rangle$ as the ground state manifold and $|L = 0, m_L = 0\rangle$ as the excited state. In this example, the $|m_L = -1, 0, 1\rangle$ states respond only to σ^+ , π , and σ^- polarizations respectively, so that the light shift is clearly state-dependent but scales with $1/\Delta_L$. Indeed, for atomic species with non-zero orbital angular momentum in the ground state, such as titanium, which is a transitional metal, or erbium, which is a lanthanide, significant non-scalar light shift per unit light scattering rate can be achieved far away from atomic resonances [44].

3.3 Calculation of atomic polarizability

The general quantum-mechanical expression for light shift experienced by an atom in an external electric field is provided by second-order perturbation theory. To derive the expression for atomic polarizability, it is sufficient to work in the semiclassical picture, where we work with quantized energy levels of the atom but treat the electromagnetic field classically. Furthermore, in the long-wavelength approximation (also known as dipole approximation) where the wavelength of the light is much larger than the localization extent of the addressed electron, the atom-light interaction H_{int} resembles the expression for the energy of a classical dipole in an electric field: $-\mathbf{d} \cdot \mathbf{E}$, with $\mathbf{d} = q\mathbf{r}$ now a quantum-mechanical operator. Assuming a monochromatic field with angular frequency ω , we can split H_{int} into two parts, one rotating at positive

frequency (V_-) and the other rotating at negative frequency (V_+)³:

$$\begin{aligned} H_{\text{int}} &= -(\mathbf{d} \cdot \hat{\epsilon})E(\omega)e^{-i\omega t} - (\mathbf{d} \cdot \hat{\epsilon}^*)E(\omega)e^{+i\omega t} \\ &= V_-e^{-i\omega t} + V_+e^{i\omega t} \end{aligned}$$

Note that the complex phase is assumed by the polarization vector ϵ , and the amplitude of the oscillation $E(\omega)$ is real. We obtain the second-order energy shift due to this time-dependent perturbation by calculating the first-order correction to the wavefunction using standard time-dependent perturbation theory. Since H_{int} is time-periodic, we can also apply a more systematic approach such as Floquet perturbation theory, which is described in Appendix D of Ref. [25]. The second-order energy shift given by this approach closely resembles the expression for the shift given by time-independent second-order perturbation theory:

$$\delta E = \sum_{n'} \frac{\langle n|V_+|n'\rangle\langle n'|V_-|n\rangle}{E_n - E_{n'} + \hbar\omega} + \sum_{n'} \frac{\langle n|V_-|n'\rangle\langle n'|V_+|n\rangle}{E_n - E_{n'} - \hbar\omega}$$

The state $|n\rangle$ is the initial and final state of the atom, and $|n'\rangle$ ($\neq |n\rangle$) are the intermediate states connected by the atom-light interaction. The energy shift may be rewritten as

$$\begin{aligned} \delta E &= (\langle n|(\mathbf{d} \cdot \hat{\epsilon}^*)R_+(\mathbf{d} \cdot \hat{\epsilon}) + (\mathbf{d} \cdot \hat{\epsilon})R_-(\mathbf{d} \cdot \hat{\epsilon}^*)|n\rangle) E(\omega)^2 \\ R_{\pm} &= \sum_{n'} \frac{|n'\rangle\langle n'|}{E_n - E_{n'} \pm \hbar\omega} \end{aligned} \quad (3.2)$$

We can express $(\mathbf{d} \cdot \hat{\epsilon}^*)R_+(\mathbf{d} \cdot \hat{\epsilon})$ as $(d_i R_+ d_j) \hat{\epsilon}_i^* \hat{\epsilon}_j$ and apply the decomposition into three irreducible tensor components for $d_i R_+ d_j$ and $\hat{\epsilon}_i^* \hat{\epsilon}_j$. Similar decomposition should be done for $d_i R_- d_j$ and $\hat{\epsilon}_i \hat{\epsilon}_j^*$. We assume that $|n\rangle$ and $|n'\rangle$ are eigenstates of the total angular momentum operator \mathbf{J} , so it is better to perform the irreducible tensor decomposition in the spherical basis. From here now on, we refer to the tensor $d_i R_{\pm} d_j$ as $\mathbf{d} \otimes R_{\pm} \mathbf{d}$ and the spherical components of its irreducible rank- k tensors as

³Note that Ref. [25] uses the symbol V_- for the positive-frequency term. The symbol may make more sense if we take the minus sign to suggest photon absorption [45].

$(\mathbf{d} \otimes R_{\pm} \mathbf{d})_q^{(k)}$ with $-k \leq q \leq k$, and similarly for $\hat{\epsilon}_i^* \hat{\epsilon}_j$. In the spherical basis, we can re-organize the terms further in using Eq. D.2 (see Appendix D and Ref. [25]):

$$\delta E = E(\omega)^2 \sum_{k=0}^2 (-1)^k \sum_{q=-k}^k (-1)^q \langle n | (\mathbf{d} \otimes (R_+ + (-1)^k R_-) \mathbf{d})_q^{(k)} | n \rangle (\epsilon^* \otimes \epsilon)_{-q}^{(k)}$$

Assuming $|n\rangle = |J, m_J\rangle$, we can apply the Wigner-Eckart theorem⁴ to $\langle n | \mathbf{d} \otimes R_{\pm} \mathbf{d} | n \rangle$:

$$\langle J, m_J | (\mathbf{d} \otimes R_{\pm} \mathbf{d})_q^{(k)} | J, m_J \rangle = \langle J || (\mathbf{d} \otimes R_{\pm} \mathbf{d})^{(k)} || J \rangle \langle J, m_J | J, m_J; k, q \rangle$$

The Clebsch-Gordan coefficient forces $q = 0$. We can substitute explicit expressions for the Clebsch-Gordan coefficient for $k = 0, 1, 2$:

$$\begin{aligned} \langle J, m_J | J, m_J; 0, 0 \rangle &= 1 \\ \langle J, m_J | J, m_J; 1, 0 \rangle &= \begin{cases} \frac{m_J}{\sqrt{J(J+1)}} & J \geq \frac{1}{2} \\ 0 & \text{else} \end{cases} \\ \langle J, m_J | J, m_J; 2, 0 \rangle &= \begin{cases} \frac{3m_J^2 - J(J+1)}{\sqrt{J(1+J)(2J-1)(2J+3)}} & J \geq 1 \\ 0 & \text{else} \end{cases} \end{aligned}$$

We immediately see why a non-zero angular momentum is required for non-scalar effects. In particular, if $J = 1/2$, as is the case for alkali atoms, the vector term is non-zero but the tensor term is zero. A hand-waving explanation is that one can establish a non-zero orientation with two sublevels, but one needs at least three sublevels to establish a non-zero alignment, which is associated with tensorial effects⁵. The minimum requirement of $J = 1/2$ for a vector effect and $J = 1$ for a tensor effect still holds when the hyperfine interaction between the electron total angular

⁴Note that the normalization of reduced matrix element depends on the choice of convention; see Appendix D. Also, reduced matrix element does not behave like a normal matrix element under conjugation [46].

⁵A visual explanation for the difference between orientation and alignment is an asymmetric 2D Gaussian distribution centered at zero with a small variance along the x-axis and a large variance along the y-axis. The zero average represents zero orientation and the asymmetric variances represent a non-zero alignment towards the y-axis.

momentum J and the nuclear spin I is included.

To arrive at a simple expression for the second-order light shift, we also provide explicit expressions for $(\epsilon^* \otimes \epsilon)_0^{(k)}$ [25]:

$$\begin{aligned} (\epsilon^* \otimes \epsilon)_0^{(0)} &= -\frac{1}{\sqrt{3}} \\ (\epsilon^* \otimes \epsilon)_0^{(1)} &= \frac{i}{\sqrt{2}} (\hat{\epsilon}^* \times \hat{\epsilon}) \cdot \hat{z} = -\frac{1}{\sqrt{2}} \mathcal{A} \cos \theta_k \\ (\epsilon^* \otimes \epsilon)_0^{(2)} &= \frac{1}{\sqrt{6}} (3|\hat{\epsilon} \cdot \hat{z}|^2 - 1) = \frac{1}{\sqrt{6}} (3 \cos^2 \theta_p - 1) \end{aligned}$$

We have introduced two angles related to polarization: $\cos \theta_k = \hat{k} \cdot \hat{z}$ and $\cos \theta_p = \hat{\epsilon} \cdot \hat{z}$. The first angle is the angle between the laser wavevector and the quantization axis, and the second angle is the angle between the polarization and the quantization axis. We see that in order to take advantage of the vectorial effect, the wavevector needs to be parallel to the quantization axis. The final expression for the second-order light shift is

$$\delta E = -E(\omega)^2 \left[\alpha_J^S + \mathcal{A} \cos \theta_k \frac{m_J}{2J} \alpha_J^V + \left(\frac{3 \cos^2 \theta_p - 1}{2} \right) \frac{3m_J^2 - J(J+1)}{J(2J-1)} \alpha_J^T \right] \quad (3.3)$$

where the scalar, vector, and tensor polarizabilities α^S , α^V , α^T are defined as

$$\begin{aligned} \alpha_J^S &= \frac{1}{\sqrt{3}} \alpha_J^{(0)} \\ \alpha_J^V &= -\sqrt{\frac{2J}{J+1}} \alpha_J^{(1)} \\ \alpha_J^T &= -\sqrt{\frac{2J(2J-1)}{3(J+1)(2J+3)}} \alpha_J^{(2)} \\ \alpha_J^{(k)} &= \left\langle J \left\| \left(\mathbf{d} \otimes (R_+ + (-1)^k R_-) \mathbf{d} \right)^{(k)} \right\| J \right\rangle \end{aligned} \quad (3.4)$$

Note that the frequency dependence is built in R_{\pm} . For the computation of non-scalar light shift for hyperfine states, where we assume that the detuning is sufficiently large enough to leave the hyperfine structure unresolved, we replace $|J, m_J\rangle$ with $|F, m_F\rangle$ and make the substitutions $J \rightarrow F, \alpha_J^{(k)} \rightarrow \alpha_F^{(k)}$ in Eq. 3.3 and Eq. 3.4. The explicit

expressions for $\alpha_J^{(k)}$ and $\alpha_F^{(k)}$ are provided in Appendix D.

3.4 Wavelength selection

For state-dependent control with off-resonant laser beams, we are interested in having a large vector shift per unit of optical power. However, since that requires a smaller detuning for atomic species without non-zero orbital angular momentum in the ground state manifold, one has to make a compromise between maximum achievable vector shift and limited lifetime due to light scattering. For atomic species such as rubidium and cesium, the presence of a large splitting between the D_1 and D_2 lines allows one to achieve a reasonable (vector shift/scattering rate) ratio by setting the wavelength between the D lines. See Fig. 3-2 for the ratio calculated for ^{87}Rb . However, between

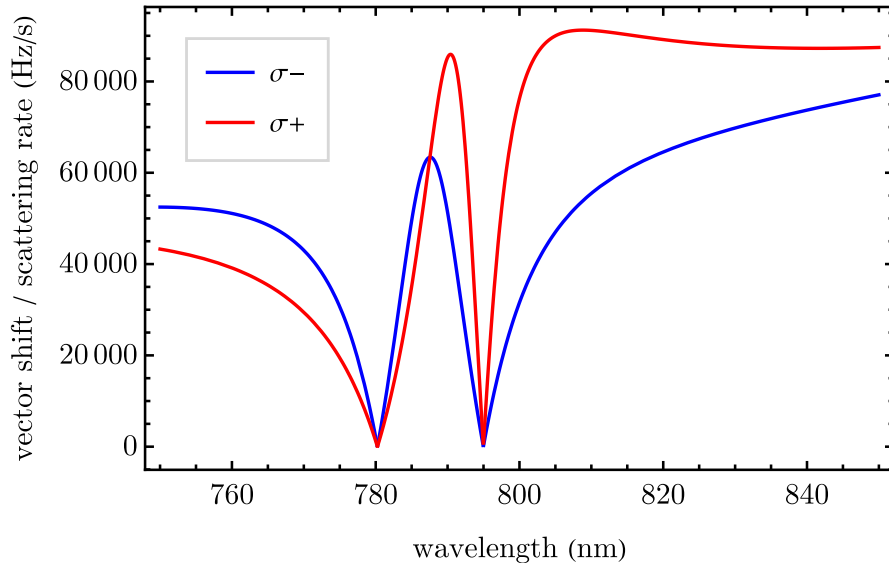


Figure 3-2: Ratio of vector shift to total light scattering rate for $|F, m_F\rangle = |1, -1\rangle$ for different polarizations. The vector shift is defined here as the difference between the light shift of the chosen circular polarization and that of the opposite circular polarization. The assumed beam parameters are incident power of 0.1 W and $1/e^2$ beam radius of $125 \mu\text{m}$.

the D lines the nature of the light scattering is largely spontaneous Raman scattering from one hyperfine state to another, as we see in Fig. 3-3. Since spin impurities may be deleterious for quantum simulation of spin chains in an optical lattice, it is best

to select a wavelength where Raman scattering is minimized. Thus we decided to set the wavelength of our state-dependent optical lattice to 810 nm where Rayleigh scattering is dominant.

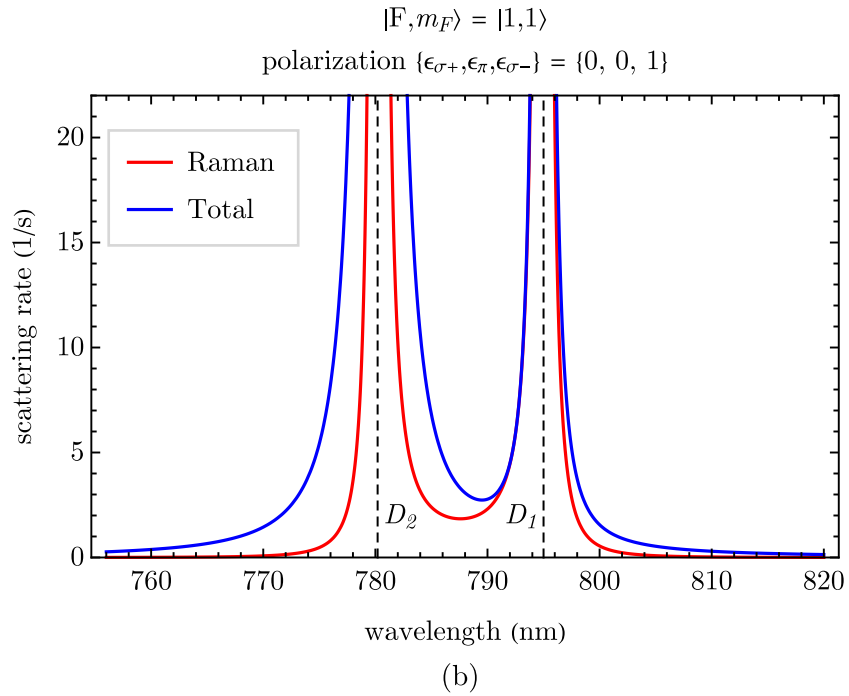
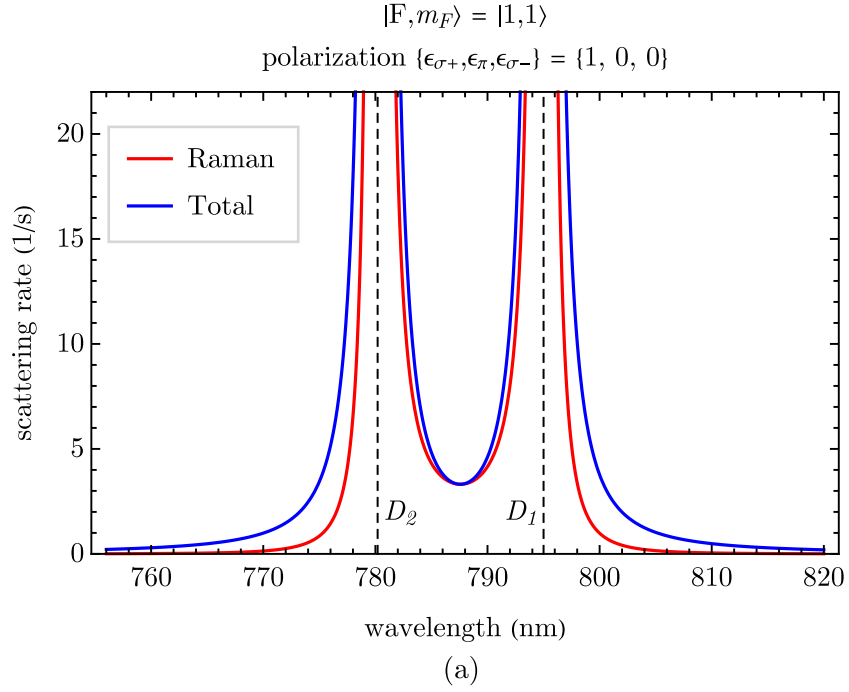


Figure 3-3: Light scattering rate calculation for $|F, m_F\rangle = |1, 1\rangle$ with incident power of 0.1 W and $1/e^2$ radius of $125 \mu\text{m}$. The dotted lines show the locations for D_1 and D_2 resonances. (a) σ^+ polarization. (b) σ^- polarization.

Chapter 4

Optical Lattices

An optical lattice is a standing wave of light that provides a periodic potential for atoms. It is widely used as a primary tool in quantum simulation and atom-based metrology experiments. A small sample of the spectacular applications of this tool includes the observation of long-range anti-ferromagnetic ordering in fermions [47] and the realization of 10^{-18} frequency stability by an optical lattice clock [48]. A general survey of modern research topics being investigated in optical lattice experiments can be found in [49–51]. A review of the dynamics of matter waves inside an optical lattice can be found in [52]. Some of the non-cubic lattice geometries are discussed in [53]. Our lab is interested in using a state-dependent optical lattice for controlling the interaction between atoms in different hyperfine states¹. Hence this chapter will review the properties of a state-dependent lattice and its implementations.

4.1 Making an optical lattice

We first review the simplest form of an optical lattice: the state-independent or scalar lattice with cubic symmetry. Assume we have a laser whose electric field can be idealized as a plane wave that propagates in the $+x$ direction with angular frequency ω , wavevector $k = \omega/c$ and complex amplitude E_0 . Without loss of generality, we

¹In this context, the hyperfine states all belong to the ground state manifold. Another example of a state-dependent control is the provision of a differential light shift between an excited state and a ground state [54].

assume the field is linearly polarized in the z -direction. Then the total electric field after a retroreflection is

$$\vec{E}(x, t) = (E_0 e^{ikx - i\omega t} + E_0 e^{-ikx - i\omega t}) \hat{z}$$

The time-averaged intensity of this electric field in vacuum with permittivity ε_0 written as

$$I(x) = \frac{1}{2} \varepsilon_0 c |\vec{E}|^2 = \varepsilon_0 c |E_0|^2 \cos(kx)^2$$

The potential seen by atoms with scalar dynamic polarizability $\alpha(\omega)$ (Eq. 3.1) at angular frequency ω is

$$U(x) = -\frac{1}{2\varepsilon_0 c} \text{Re}[\alpha(\omega)] I(x) = -\frac{\text{Re}[\alpha(\omega)]}{2} |E_0|^2 \cos(kx)^2$$

One can generalize the one-dimensional lattice to three dimensions by adding retro-reflected laser beams along other directions. By using orthogonal polarizations and introducing reasonable frequency offsets, the potential is separable and we can write the total potential as $U_{3D}(x, y, z) = U(x) + U(y) + U(z)$. Intricate interference between electric fields of lasers with different orientations of wavevectors can give rise to non-separable potentials, such as hexagonal [55], honeycomb [56], or Kagome [57] lattices in two dimensions.

The behavior of a single atom trapped in periodic potential can be found by diagonalizing the Hamiltonian $H = p^2/2m + U(x)$ with the help of Bloch's theorem [58]. The eigenstates $|\psi_{n,k}\rangle$ are labeled by band index n where $n = 0, 1, 2, \dots$ and crystal momentum (also known as quasimomentum) $\hbar k$, where $-\pi/a_L \leq k \leq \pi/a_L$ and a_L is the spatial periodicity or the lattice constant of the potential. By Bloch's theorem, the eigen-wavefunctions $\psi_{n,k}(x)$ take the form $e^{ikx} u_{n,k}(x)$ where $u_{n,k}(x)$ is periodic with periodicity a_L . These so-called Bloch functions are delocalized in space.

However, for the study of interacting atoms, the Bloch state basis is rather inconvenient to work with, because for many atomic species the dominant form of

interaction is a short-range interaction by s -wave collisions and hence interaction takes place locally at individual lattice sites. Thus, it is preferable to transform to a basis where the wavefunctions are maximally localized, and such a basis is known as the Wannier basis. Each Wannier function is labeled by band index n and coordinate number R , which is the spatial coordinate of the center of the function. Without loss of generality, the transformation from the Bloch basis to the Wannier basis in one dimension is defined as

$$|w_{n,R}\rangle = \frac{L}{2\pi} \int_{\text{BZ}} dk e^{-ikR} e^{i\theta(k)} |\psi_{n,k}\rangle$$

where L is the length of the lattice and BZ stands for integration over the first Brillouin zone. A good choice of “gauge” function² $e^{i\theta(k)}$ yields a wavefunction that is maximally localized, i.e., yields minimal $\langle x^2 \rangle$ [59]. See Figure 4-1 for a comparison between a Bloch function and a Wannier function. Although it is customary for solid state physics textbooks to introduce the Wannier basis states as simple superpositions of Bloch states [58], with $e^{i\theta(k)}$ appearing to be unity³, a direct application of such a definition to the numerically obtained Bloch wavefunctions leads to Wannier wavefunctions that are not well-localized over single or several lattice sites. For one-dimensional periodic potentials which are even under inversion, it has been proved that for every band there exists a unique Wannier function satisfying the following three properties [60]:

1. It is real.
2. It is either even or odd under inversion about either $x = 0$ or $x = a_L/2$.
3. It falls off exponentially.

²One can generalize the transformation to involve multiple bands by promoting $e^{i\theta(k)}$ to a unitary matrix [59], although this is not necessary for lattices with simple band structures such as cubic lattice.

³Technically there is nothing wrong with this, as the Bloch basis states can be defined in such a way that they absorb the phase $e^{i\theta(k)}$.

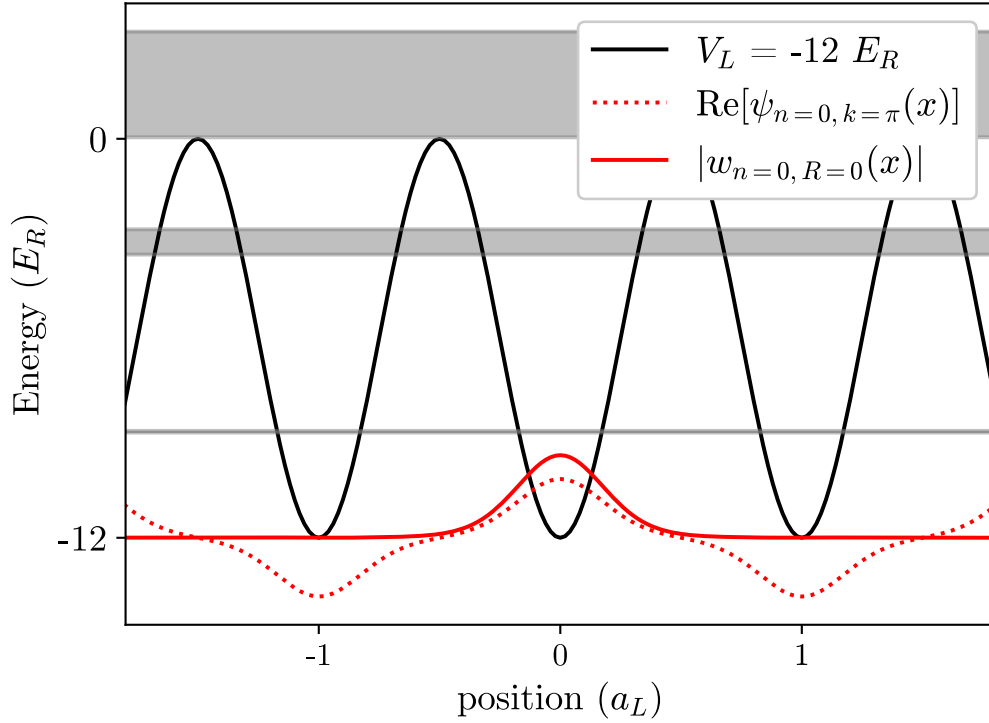


Figure 4-1: Comparison between Wannier and Bloch functions. The black solid line represents a one-dimensional lattice with lattice depth $12 E_R$ where $E_R = \hbar^2/(2m\lambda^2)$ is the recoil energy of the lattice laser. The solid red line denotes the modulus of the probability amplitude of a ground band Wannier function centered at $R = 0$. The dotted red line denotes the modulus of the probability amplitude of a ground band Bloch function with wavevector $k = \pi/a_L$. The gray bands represent the three lowest energy bands of the lattice potential, where the bandwidth is inversely related to the effective mass inside the lattice.

Furthermore, the exponential decay rate of such a Wannier function is maximal, where in the tight-binding limit the decay rate is proportional to the inverse of the length scale given by the band energy gap $\hbar/\sqrt{2mE_{\text{gap}}}$. Properties 1 and 2 suggest that the desired Wannier function for the n -th band can be simply obtained by choosing $\theta(k)$ to be conjugate to the phase angle of either $\psi_{k,n}(x=0)$ or $\partial_x \psi_{k,n}(x=0)$, depending on the symmetry of the n -th band orbitals (see Section 6 in Ref. [60]).

4.2 State-dependent optical lattice

If the atoms have a non-zero *vector* polarizability, we can generate a state-dependent lattice: atoms in different internal states experience different light shifts under the same laser, as we saw in Section 3.3. By introducing a polarization gradient along the lattice beam, we can adjust the differential light shift between two internal states. In the present context, a polarization gradient is a periodic spatial modulation of the circularity of the local polarization. There are two schemes to implement such modulation: lin- θ -lin and $\sigma^+ - \sigma^-$.

It is worth mentioning that there are important similarities and differences between polarization gradients used for state-dependent optical lattices and those used for polarization gradient cooling, which is a sub-Doppler laser cooling technique [61]. The type of polarization gradient created in the lin- θ -lin scheme is related to the one used in the lin- \perp -lin polarization gradient cooling method, where interference between a linear polarized beam and a counter-propagating beam with a rotated linear polarization creates a periodic modulation in the circularity of the local polarization. On the other hand, for the $\sigma^+ - \sigma^-$ cooling method, a σ^+ beam propagates against a counter-propagating σ^- beam, and the local polarization always stays linear but its angle rotates as it travels along the beam axis. However, in the $\sigma^+ - \sigma^-$ scheme for state-dependent lattices, the σ^+ and σ^- beams copropagate in the same direction and creates a spatial modulation in the circularity of the local polarization.

Each scheme comes with two variants. The lin- θ -lin scheme requires the use of a variable retarder, and one has the option of placing the variable retarder before or after the atom cloud. The $\sigma^+ - \sigma^-$ scheme requires two orthogonally polarized and independent beams, and one has the option of introducing either a phase offset or a frequency offset between the input beams. In our experiment, we explored the uses of the secondary option for each scheme. Below we analyze in detail the implementation of the secondary option for each scheme but also make connections to the implementations of the primary option for each scheme realized by other groups [41, 62].

4.2.1 lin- θ -lin scheme

In this scheme, the input lattice beam is linearly polarized. The input beam goes through a variable waveplate and other fixed waveplates so that the retroreflected beam has a linear polarization that is rotated with respect to the input polarization. We will discuss the physical implementations of the polarization rotation by the waveplates later in this subsection.

Assume we have a total electric field described by

$$\vec{E} = E_0 e^{-i\omega t} \left[\begin{pmatrix} 1 \\ 0 \end{pmatrix} e^{ikz} + \begin{pmatrix} \cos \theta \\ \sin \theta \end{pmatrix} e^{i\phi} e^{-ikz} \right] + \text{c.c}$$

The phase offset $e^{i\phi}$ of the retroreflected light results in a spatial offset of the intensity and polarization gradients [$x \rightarrow x - \phi/(2k)$], so we set $\phi = 0$ without loss of generality⁴. If we denote the ratio of the vector polarizability to the scalar polarizability α_F^V/α_F^S to be $2R$, then using Eq. 3.3 we can write the total light shift as

$$\delta E(\theta, z) = -|E_0|^2 \alpha_F^S \left(2 + 2 \cos(2kz) \cos \theta - 2R \cos \theta_k \sin(2kz) \sin \theta \frac{m_F}{F} \right)$$

where θ_k is the angle between the quantization axis and the lattice wavevector. If we choose two hyperfine states with $m_F = \pm F$, we can simplify the expression using the trigonometric identity $A \cos(2kz + B) = A \cos(B) \cos(2kz) - A \sin(B) \sin(2kz)$:

$$\begin{aligned} \delta E(\theta, z) &= -|E_0|^2 \alpha_F^S \left(2 + 2A(\theta) \cos \left(2kz + \frac{m_F}{F} B(\theta) \right) \right) \\ A(\theta) &= \sqrt{\cos^2 \theta + (R \cos \theta_k)^2 \sin^2 \theta} \\ B(\theta) &= \arctan(R \cos \theta_k \tan(\theta)) \end{aligned}$$

See Fig. 4-2 for an example of how different hyperfine states are spatially separated by the state-dependent lattice. Note that a smaller vector-to-scalar ratio results in a narrow tuning range for the spin separation. The product of the local intensity and

⁴However, this shows that ϕ needs to be stable, or the optical lattice has a phase noise and can give rise to a nonzero transition rate from the ground band to the first excited band [63].

the local circularity of the polarization $\mathcal{A}(x)$ acts a source for a fictitious magnetic field that separates atoms with opposite magnetic moments. The gradient of the fictitious magnetic field is strongest at the nodes and the antinodes of the intensity modulation. If $-2|E_0|^2\alpha_F^S$ is equivalent to a potential depth of 10 kHz, then the fictitious magnetic gradient at the intensity extrema seen by $|F = 1, m_F = -1\rangle$ is equivalent to 277 G/cm for $(R \cos \theta_k, \theta) = (1/8, \pi/2)$.

The simplest method to achieve polarization rotation of a retroreflected laser beam is to insert a quarter-waveplate in front of the retroreflecting mirror. However, one would have to mechanically rotate the quarter-waveplate to dynamically change the spin separation, and that is not ideal in terms of speed and stability. A common way to achieve electric control of polarization rotation is to use a voltage variable waveplate, in which the retardance along the slow axis of the waveplate can be adjusted by an external voltage. However, with a variable waveplate alone, the polarization of the retroreflected light is not linear in general, except for special values of retardances. Hence the variable waveplate needs to be combined with other fixed waveplates.

Variable waveplate after the atom cloud

A general setup for polarization rotation control with the variable waveplate placed after the cloud is described in Fig. 4-3(a). The setup has two fixed waveplates and a single variable waveplate. This setup features an extra half-waveplate (HWP) added to the setup described in [40]. The HWP controls the rotation angle of the polarization at zero voltage applied to the variable waveplate. The quarter-waveplate (QWP), whose slow axis is oriented 45° with respect to that of the variable waveplate, ensures that the output is linearly polarized. With the input polarization set to a vertically oriented linear polarization $[(E_x, E_y) = (0, 1)]$, and the angles of the slow axes as shown in Fig. 4-3, the polarization of the retroreflected beam (E_x, E_y) can be shown using Jones matrices [64] to be

$$\begin{pmatrix} E_x \\ E_y \end{pmatrix} = e^{i\eta} \begin{pmatrix} -\cos(4\theta_H + \eta) \\ \sin(4\theta_H + \eta) \end{pmatrix},$$

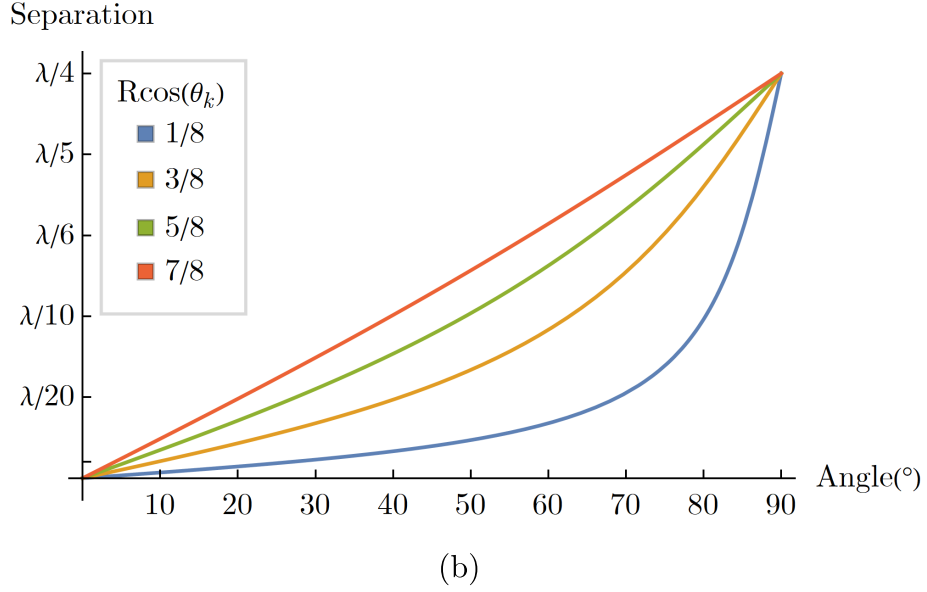
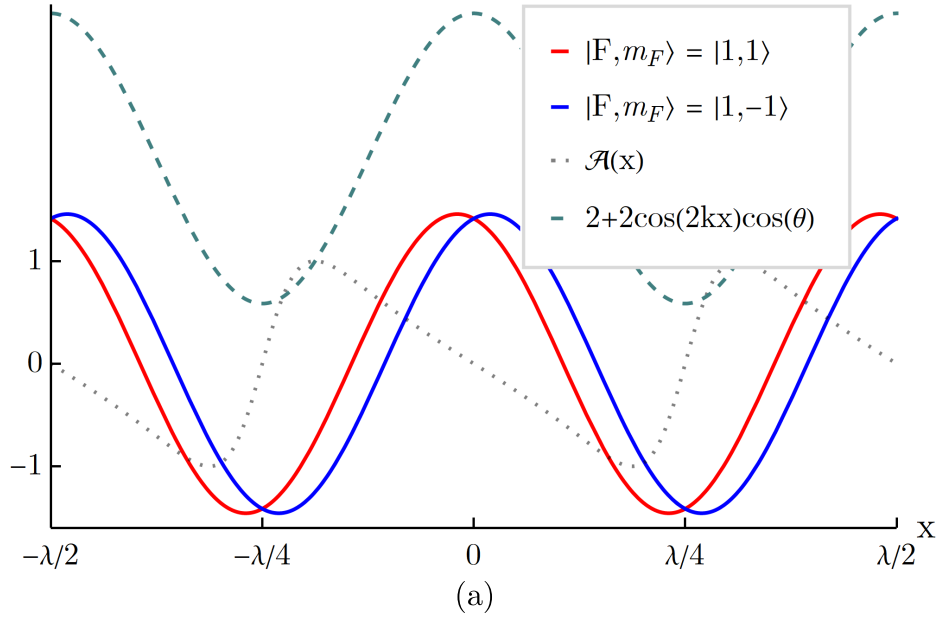
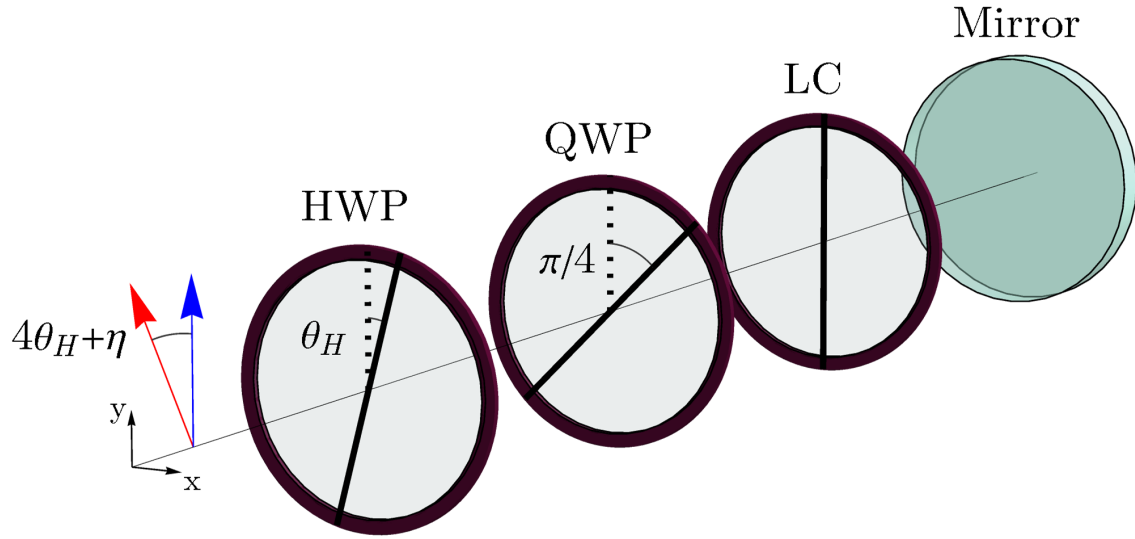
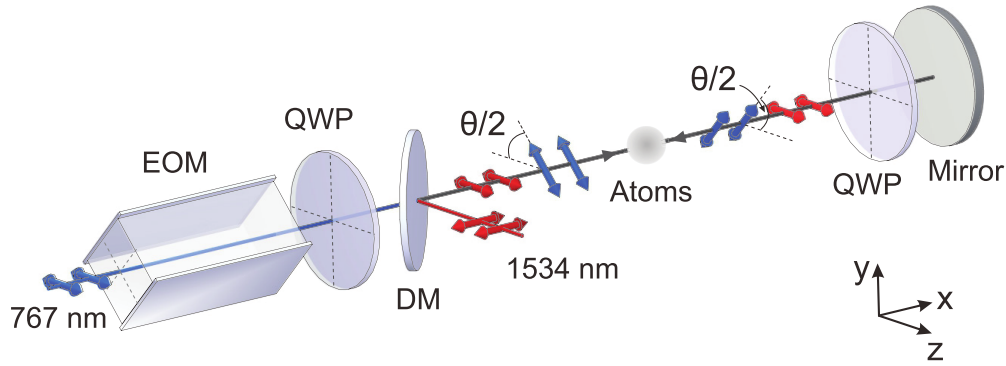


Figure 4-2: (a) Plot of $2A(\theta) \cos\left(2kz + \frac{m_F}{F}B(\theta)\right)$ for $(R \cos \theta_k, \theta) = (1/4, \pi/4)$. The red and blue lines are the modulation of the total potential seen by $|F = 1, m_F = 1\rangle$ and $|F = 1, m_F = -1\rangle$ hyperfine states. The gray dotted line is the local circularity of the polarization $\mathcal{A}(x)$. The green dashed line is the local intensity. The product of the local intensity and the local circularity acts as a fictitious magnetic field that separates atoms with opposite magnetic moments. Note that the extrema of the circularity do not exactly match the extrema of the potentials seen by the different hyperfine states. (b) Separation between $m_F = F$ and $m_F = -F$ states given by $2B(\theta)$ vs. rotation angle of the polarization, for different values of $R \cos \theta_k$.



(a)



(b)

Figure 4-3: Polarization rotation control for state-dependent lattices. (a) Variable retarder after the atom cloud. The setup consists of a half-waveplate (HWP), quarter-waveplate (QWP), and a variable retarder such as an electro-optic modulator (EOM) or a liquid crystal (LC) device. The dotted lines denote the vertical axis. The thick solid lines denote the slow axes of the waveplates. With the input polarization (blue arrow) vertically oriented and the slow axes oriented as in the diagram, the output polarization (red arrow) is linear and rotated by $4\theta_H + \eta$ from the input polarization, where θ_H is the HWP angle and η is the retardance by the LC slow axis. The output electric field also has a phase delay (not shown) of $e^{i\eta}$ with respect to the input field. (b) Variable retarder before the atom cloud. Figure adapted from Fig. 1(a) in [41].

where θ_H is the rotation angle of the HWP and η is the retardance of the slow axis of the variable waveplate. If the QWP does not provide exactly $\lambda/4$ retardance or its slow axis is not oriented 45° with respect to that of the variable waveplate, then the polarization of the retroreflected beam is elliptical in general. If α is the deviation of the QWP retardance from $\lambda/4$ and β is the deviation of the relative angle between the QWP and the variable waveplate from 45° , then one can show that E_y has an amplitude $\cos(\eta) \sin(\alpha) + \cos(\alpha) \sin(2\beta) \sin(\eta)$ in quadrature to the rest of the amplitudes. This residual quadrature amplitude forms a secondary state-independent optical lattice with the input polarization that is added in quadrature to the intensity modulation of the main optical lattice. Such a secondary optical lattice leads to a noticeable imbalance between the potential depths seen by hyperfine states with opposite m_F .

Variable waveplate before the atom cloud

One can also place the variable waveplate before the atom cloud, as it was demonstrated in the state-dependent optical superlattice experiment in Ref. [41]. The main advantage of this setup is that the variable plate does not introduce any intensity imbalance between the input beam and the retroreflected beam and the variable plate selectively rotates the polarization of one beam while not affecting that of the other beam, making it suitable for an optical superlattice experiment. Another advantage is that if the variable waveplate were to introduce fluctuations around the retardance setpoint η , it would not affect the optical path length between the atom cloud and the retroreflecting mirror⁵. The setup is described in Fig. 4-3(b). We assume the slow axes of the two QWP's are oriented vertically and the EOM slow axis is oriented $+45^\circ$ with retardance of η . After a horizontally polarized beam passes through the EOM and the two QWP's, the input polarization and the output polarization at the

⁵An LC device is susceptible to introducing fast fluctuations around the retardance setpoint because of its operation mechanism.

location of the atom cloud is

$$\begin{pmatrix} E_H \\ E_V \end{pmatrix}_{\text{in}} = e^{i\eta/2} \begin{pmatrix} \cos \frac{\eta}{2} \\ -\sin \frac{\eta}{2} \end{pmatrix}, \quad \begin{pmatrix} E_H \\ E_V \end{pmatrix}_{\text{out}} = -e^{i\eta/2} \begin{pmatrix} \cos \frac{\eta}{2} \\ \sin \frac{\eta}{2} \end{pmatrix}$$

Thus, the output polarization is rotated from the input polarization by $\pi+\eta$. Similarly to the setup with the variable waveplate after the cloud, the relative angle between the EOM and the QWP must be $\pm\pi/4$ to ensure the linearity of the polarization.

Residual elliptical polarization due to a folding mirror

Besides the imperfection in the QWP retardance and in the relative angle alignment between the QWP and the LC/EOM device, optical elements between the waveplates can impact the fidelity of the polarization control. In particular, folding mirrors can impart a nominally small phase shift between the s and p polarizations that nevertheless results in a substantial imbalance in the state-dependent potential. Figure 4-4 shows a comparison between a simulation of an additional phase shift of $\lambda/35$ between s and p polarizations due to a folding mirror (a protected silver mirror from Thorlabs) before the QWP in Fig. 4-3(a) and measured imbalance in the 810 nm lattice potential seen by $|F, m_F = 1, -1\rangle$ and $|1, 1\rangle$. We see that the added phase shift nicely explains the 20% potential imbalance we observed, which is significant in that a phase shift of $\lambda/35$ is probably negligible for most other purposes. A lattice depth imbalance of 20% results in a large imbalance in the second-order tunneling amplitudes for the two hyperfine states, due to the exponential dependence of tunneling amplitude on lattice depth. Thus it is strongly advised that the state-dependent lattice optics be kept on a single optical axis as was done in our setup for the experiments described below.

LC vs EOM

The device choice for the variable waveplate is also important for high fidelity polarization control. One can use a liquid crystal (LC) variable retarder or an electro-optic modulator (EOM). A qualitative comparison between the two devices is summarized in Table 4.1. It is immediately clear that the EOM is a superior device in terms of

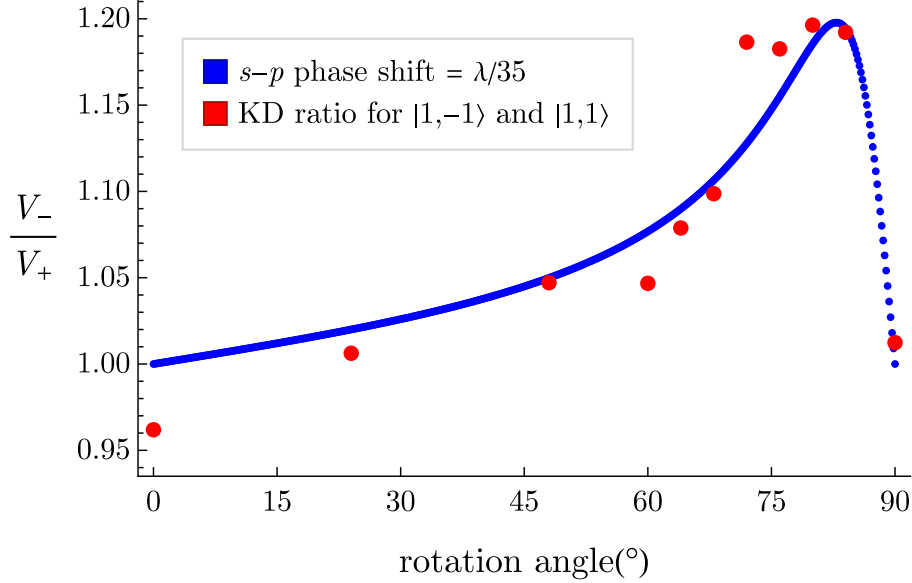


Figure 4-4: Imbalance in the state-dependent lattice potential depth caused by a folding mirror (Thorlabs ultrafast-enhanced silver mirror UM10-AG) in front of the QWP in Fig. 4-3(a). The blue dots are the estimated imbalance ratio caused by an additional phase lag of $\lambda/35$ by the s polarization. The red dots are imbalance ratios of the lattice depths estimated from Kapitza-Dirac scattering data.

Table 4.1: Comparison of LC and EOM performance

	LC	EOM
Response time	$\mathcal{O}(100 \text{ ms})$	$< 1 \text{ ms}$
Voltage control	nonlinear	linear
Intensity noise	large	small
Refractive index uniformity	good	poor

ease of control, but its major disadvantage is the refractive index inhomogeneity. As the voltage applied to the EOM changes, the curvature of the refractive index also changes and results in a deflection of the beam⁶ [18]. The inhomogeneity also leads to a worse polarization extinction ratio. It is possible to minimize the effect of the refractive index inhomogeneity by making the beam spot passing through the EOM as small as possible. However, nonlinear crystals (e.g. lithium niobate) used for the EOM may suffer from photorefractive damage at high intensity [65]. We were able to minimize the beam deflection by putting the EOM after a focusing lens and before the

⁶The device tested was Newport electro-optic amplitude modulator (Model 4102) [discontinued].

retroreflecting mirror, but the quoted threshold intensity for photorefractive damage was not high enough for our application. In principle, the beam displacement can also be minimized if the EOM is constructed with multiple units of carefully matched crystals [66]. Typical amplitude modulators are equipped with two matched crystals oriented at $\pm 45^\circ$, which cancels thermal drift due to the natural birefringence while doubling the polarization rotation [65]. If another pair of matched crystals is added⁷, the beam displacement due to a gradient in the natural birefringence may be canceled. Such a four-matched-crystal modulator is sold by QiOptiq/LINOS [67], but its main downside is that the device is rather heavy and quite bulky in size. Due to its long lead time and our limited optical breadboard space, we decided to continue using the device of our default choice, which is the LC waveplate.

Since polarization purity is of utmost importance for dynamic tuning of a state-dependent lattice, we decided to use a LC device. The main problem with the LC device is its control mechanism, which relies on reducing the inherent birefringence of the LC molecules by rapidly modulating the direction of the electric field. This unavoidably leads to intensity noise added at the modulation frequency and causes hysteresis in the switching speed (increasing the voltage leads to a faster retardance change than decreasing the voltage). It can also produce lattice phase noise by modulating the global phase $e^{i\eta}$ in the polarization of the laser but this can be prevented by placing the LC in front of the atom cloud. It is possible to change the retardance of the LC faster than its natural switching speed by forcing the control voltage higher than the desired value and then reducing it - this is known as the transient nematic effect [68]. To make use of this, we manually tune the control voltage pulse shape for every combination of initial and final retardances and ramping times.

4.2.2 $\sigma^+ - \sigma^-$ scheme

In this scheme, the state-dependent lattice is formed by a combination of two independent lattice beams with σ^+ and σ^- polarizations respectively. One has the option to add either a frequency offset or a phase offset between the two beams (Fig. 4-5).

⁷Possibly oriented at $180^\circ \pm 45^\circ$.

We first analyze the scheme with a frequency offset.

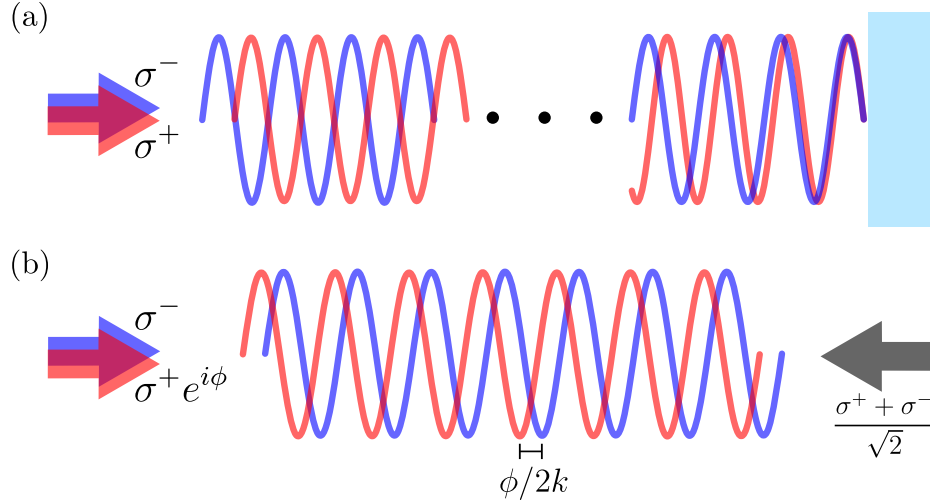


Figure 4-5: The $\sigma^+ - \sigma^-$ scheme for state-dependent lattices. A σ^+ beam (red arrow) and a σ^- beam (blue arrow) copropagate in the same direction. (a) Scheme with frequency offset. There is no lattice phase offset at the surface of the retroreflecting mirror, but a frequency offset results in an accumulated lattice phase offset at the location of the atom cloud. (b) Scheme with phase offset. Instead of a retroreflecting mirror, a linearly polarized beam (black arrow) counterpropagates against the input lattice beams. A phase offset of ϕ between the σ^+ beam and the σ^- beam results in a lattice phase offset of $\phi/(2k)$, where k is the wavevector of the input beams. The value of ϕ can be continuously ramped by an AOM [62].

Frequency offset between σ^+ and σ^- beams

A large tunable frequency offset is introduced between the two beams so that the separation between the antinodes of the two lattices can be adjusted while making sure that there is no interference between the two beams (Fig. 4-5(a)). Assume that one of the lattice beams (V_{σ^-}) has frequency f while the other lattice beams (V_{σ^+}) has frequency $f + \Delta f$. We also assume that Δf is much smaller than f while much larger than the largest energy scale associated with the external states of the atom in the optical lattice, so that we can time-average away any interference formed between

V_{σ^+} and V_{σ^-} . Then the total potential can be expressed as

$$\begin{aligned}
V_{\text{total}} &= V_{\sigma^+} \cos^2((k + \Delta k)z) + V_{\sigma^-} \cos^2(kz) \\
&= V_{\sigma^+} \cos^2(k(z_a + L) + \Delta k(z_a + L)) + V_{\sigma^-} \cos^2(k(z_a + L)) \\
&= \frac{V_{\sigma^+}}{2} (1 - \cos(2kz_a + 2kL + 2\Delta k(z_a + L))) + \frac{V_{\sigma^-}}{2} (1 - \cos(2kz_a + 2kL))
\end{aligned}$$

where $z = z_a + L$ is the distance between the observation point and the retroreflecting mirror, z_a is the distance between the observation point and the center of the atom cloud, and L is the distance between the center of the atom cloud and the retroreflecting mirror. Since atom cloud size is very small, we can ignore $2\Delta k z_a$. Then we see that V_{σ^+} has a lattice phase offset of $2\Delta k L = 4\pi(\Delta f/c)L$. In order to scan the full range of spin separation, the phase offset needs to have a tuning range of at least π . For $L = 1$ m, this requires that Δf have a tuning range of 75 MHz. Similar to what we have shown for the lin- θ -lin scheme, we can rewrite the total potential as single cosinusoidal term, so that the expression for the physical separation between different hyperfine states becomes clear. If we denote the lattice phase offset as θ , then

$$\begin{aligned}
V_{\text{total}} &= \frac{V_{\sigma^+}}{2} (1 - \cos(2kz + \theta/2)) + \frac{V_{\sigma^-}}{2} (1 - \cos(2kz - \theta/2)) \\
&= \frac{V_{\sigma^+} + V_{\sigma^-}}{2} - \frac{\sqrt{V_{\sigma^+}^2 + V_{\sigma^-}^2 + 2 \cos(\theta) V_{\sigma^+} V_{\sigma^-}}}{2} \\
&\quad \times \cos\left(2kz + \arctan\left(\frac{V_{\sigma^+} - V_{\sigma^-}}{V_{\sigma^+} + V_{\sigma^-}} \tan \frac{\theta}{2}\right)\right).
\end{aligned}$$

Recalling that we defined $2R$ to be the ratio α_F^V/α_F^S , we can write $V_{\sigma^{\pm}}$ in terms of input electric field and R . Assume that the electric field amplitude for V_{σ^+} is $E_{\sigma^+} e^{-i\omega t} (e^{ikz} + e^{-ikz}) + \text{c.c.}$ and similarly for V_{σ^-} . Then the maximum intensity for each lattice is $8\epsilon_0 c |E_{\sigma^{\pm}}|^2$. Also,

$$V_{\sigma^{\pm}} = 4|E_{\sigma^{\pm}}|^2 \alpha_F^S \left(1 \pm R \cos \theta_k \frac{m_F}{F}\right).$$

If we assume that V_{σ^+} and V_{σ^-} have equal input power, then the above expression helps us to rewrite the state-dependent position shift as

$$\arctan\left(\frac{V_{\sigma^+} - V_{\sigma^-}}{V_{\sigma^+} + V_{\sigma^-}} \tan\frac{\theta}{2}\right) = \arctan\left(R \cos\theta_k \frac{m_F}{F} \tan\frac{\theta}{2}\right).$$

If $m_F = \pm F$, then the separation between the two hyperfine states is

$$\frac{\lambda}{2\pi} \arctan(R \cos\theta_k \tan(\theta/2)).$$

At $\theta = \pi$, we achieve the maximal separation of $\lambda/4$. Just as in the lin- θ -lin scheme, we see that the physical separation of the hyperfine states is a nonlinear function of the control parameter θ , even though the separation between the antinodes of V_{σ^+} and V_{σ^-} is linear in θ . The separation becomes a linear function of θ if $|R \cos\theta_k| = 1$. In such a situation, hyperfine states respond to only one of the two circular polarizations and not to the other.

The $\sigma^+ - \sigma^-$ scheme is implemented by combining two orthogonally polarized input beams on a polarizing beam splitter and then passing the output through a quarter waveplate. One of the beams (with frequency $f + \Delta f$) is controlled by a double-pass AOM. Because of the limited double-diffraction efficiency at high RF frequency and lack of constructive interference between the two beams, the $\sigma^+ - \sigma^-$ scheme requires more optical power than the lin- θ -lin scheme. For the configuration where the two hyperfine states are merged, the $\sigma^+ - \sigma^-$ requires twice as much input power as the lin- θ -lin scheme because the circular polarization components interfere with their retro-reflections individually.

Phase offset between σ^+ and σ^- beams

So far, all of the schemes discussed are limited in the range of polarization rotation. When using an LC or EOM the retardance change is bounded, and the window over which the frequency of an AOM can be tuned is relatively narrow. While one only needs a rotation of π to go from a minimal separation to a maximal separation between

different hyperfine states, additional rotation beyond π can separate the atoms even more, resulting in a differential transport of atoms by an arbitrary distance. Such a scheme may be useful for measuring off-site correlations between different hyperfine states. In principle, a single retarder can achieve arbitrary displacement of a lattice site by doing a stick-slip motion of slow rotation followed by a rapid initialization to zero rotation. However, such control is highly diabatic and will increase the motional temperature of the atoms. It turns out that a smooth, endless polarization rotation control can be achieved with a series of multiple retarders controlled by a complex algorithm [69], but it may be difficult to accommodate all the devices for a quantum gas experiment. Robens *et al.* demonstrated a relatively simpler approach in [42, 62] where a phase ramp between a σ^+ beam and a σ^- beam counterpropagating against a linearly polarized beam (with all frequencies of the beam being equivalent) achieves state-dependent transport of atoms over an arbitrary number of lattice sites. A linear polarization can be seen as a superposition of σ^+ and σ^- polarizations, and hence the interference of the linearly polarized beam with the two independent σ^+ and σ^- beams forms a superposition of a σ^+ lattice and a σ^- lattice (Fig. 4-5(b)). By working at a wavelength where $|R \cos \theta_k| = 1$, lattice sites can be directly controlled by changing the phase offset between the input σ^+ and σ^- beams. A linear change in the phase offset as a function of time ($\phi = 2\pi\Delta f t$) can be simply implemented by introducing a tiny frequency offset Δf between the σ^+ and the σ^- beams (e.g. $\Delta f = 1$ kHz translates one lattice site per millisecond). However, this scheme is not without technical challenges as it involves not only intensity stabilization but also phase stabilization of individual lattice beams [62].

Chapter 5

The Bose-Hubbard Hamiltonian

The Bose-Hubbard Hamiltonian describes the dynamics of cold bosonic atoms in optical lattices. It was proposed by Jaksch et al. in Ref. [70] that a BEC loaded to an optical lattice realizes a Bose-Hubbard model studied in condensed matter physics [71], where at zero temperature and without disorder, the bosonic system can undergo a quantum phase transition from a superfluid state to a Mott insulating state as the strength of the repulsive interaction reaches a threshold value. The prediction of the superfluid-to-insulator quantum phase transition was validated experimentally in Ref. [7] in 2002, and since then there have been numerous experiments studying the properties of the Bose-Hubbard Hamiltonian and its extensions, along with their analogues in fermions [51]. Most importantly at present, however, the Bose-Hubbard Hamiltonian is the starting ground for the effective quantum spin Hamiltonian that we explore experimentally. In this chapter, we explain how to obtain the mean-field phase diagram of the Bose-Hubbard Hamiltonian realized in an optical lattice and use it to estimate the volume of the Mott phase within the trapped atom cloud.

5.1 Review of the derivation

Because it is crucial to understanding corrections to the Hamiltonian that will be discussed later, we briefly review the derivation of the (spinless) Bose-Hubbard Hamiltonian with single-band approximation as shown in Ref. [70]. The starting point is the

field operator description of the Hamiltonian of bosonic atoms in a periodic potential $V(x)$, interacting with a two-body interaction term $gU(x - x')$:

$$\begin{aligned}
H &= \int d^3x \hat{\psi}^\dagger(x) \left(-\frac{\hbar^2}{2m} \nabla^2 + V(x) \right) \hat{\psi}(x) \\
&+ \frac{g}{2} \int d^3x d^3x' \hat{\psi}^\dagger(x) \hat{\psi}^\dagger(x') U(x - x') \hat{\psi}(x') \hat{\psi}(x)
\end{aligned} \tag{5.1}$$

Here $\hat{\psi}(x)$ ($\hat{\psi}^\dagger(x)$) is the bosonic field annihilation (creation) operator at position x . For many atomic species the interaction is short-ranged, so we use the pseudopotential¹ $gU(x - x') = (4\pi\hbar^2 a_s/m)\delta(x - x')$. Then we make the ansatz that the field operator can be expanded in the basis of ground band Wannier orbitals $w_i(x)$, whose centers are indexed by lattice sites i :

$$\hat{\psi}(x) = \sum_i \hat{a}_i w_i(x)$$

This ansatz is valid if the atomic cloud is sufficiently cold such that all the atoms occupy the ground band. Note that the Wannier orbital $w(x)$ is actually a product of three one-dimensional Wannier orbitals for a three-dimensional cubic lattice². However, interaction may virtually admix some higher band Wannier orbitals [72–74], which will be discussed later. With this single-band approximation, and after using the bosonic commutation relations for \hat{a}_i and \hat{a}_i^\dagger , we arrive at

$$H = -t \sum_{\langle i,j \rangle} \left(\hat{a}_i^\dagger \hat{a}_j + \text{c.c.} \right) + \frac{U}{2} \sum_i \hat{n}_i (\hat{n}_i - 1),$$

¹This form does not work if the wavefunction is singular at the origin, in which case one needs to regularize the delta function, but we do not worry about it here.

²Three-dimensional Wannier orbitals are not expected to be separable for a general lattice geometry.

where $\langle i, j \rangle$ denotes neighboring pair of indices and the tunneling amplitude t and the interaction strength U are defined as

$$t = - \int d^3x w(x)^* \left(-\frac{\hbar^2}{2m} \nabla^2 + V(x) \right) w(x)$$

$$U = \frac{4\pi\hbar^2}{m} a_s \int d^3x |w(x)|^4.$$

Note that we have neglected next-nearest neighbor tunneling and interaction between neighboring atoms because such effects are very small due to the localization of the Wannier orbitals.

When $t \gg U$, the ground state of the system is a superfluid state ($|\psi_{U=0}\rangle \propto \exp(\alpha \sum_i \hat{a}_i^\dagger) |0\rangle$), where there is phase coherence between lattice sites. The local occupation number has a well-defined average with some variance around the average value. On the other hand, in the opposite limit $t \ll U$, the ground state is a Mott insulating state ($|\psi_{t=0}\rangle \propto \prod_i (\hat{a}_i^\dagger)^n |0\rangle$) which has no phase coherence between lattice sites and has integer occupation number with zero number fluctuation. The superfluid phase has a gapless excitation spectrum where the elementary excitation is a phonon. On the other hand, the Mott insulator phase has a gap in the excitation spectrum, where the elementary excitation is a quasiparticle-quasihole pair. Its excitation energy at zero momentum is zero at the phase transition but quickly grows to $\approx U$ as U/t increases beyond the critical value [75].

5.2 Mean-field phase diagram

It is instructive to use a mean-field approximation to obtain the phase diagram of the Bose-Hubbard Hamiltonian and see where the superfluid-insulator boundary lies in the parameter space. We posit that the order parameter for the phase transition is $\langle \hat{a}_i \rangle$, which is zero in the Mott insulating phase and nonzero in the superfluid phase. The operator \hat{a}_i can be expanded around this expectation value: $\hat{a}_i = \langle \hat{a}_i \rangle + \delta \hat{a}_i$. Then

the tunneling term can be approximated as

$$\begin{aligned}
\hat{a}_i^\dagger \hat{a}_j &= (\langle \hat{a}_i^\dagger \rangle + \delta \hat{a}_i^\dagger)(\langle \hat{a}_j \rangle + \delta \hat{a}_j) \\
&= \langle \hat{a}_i^\dagger \rangle \langle \hat{a}_j \rangle + \delta \hat{a}_i^\dagger \langle \hat{a}_j \rangle + \langle \hat{a}_i^\dagger \rangle \delta \hat{a}_j + \delta \hat{a}_i^\dagger \delta \hat{a}_j \\
&\approx \langle \hat{a}_i^\dagger \rangle \langle \hat{a}_j \rangle + (\hat{a}_i^\dagger - \langle \hat{a}_i^\dagger \rangle) \langle \hat{a}_j \rangle + \langle \hat{a}_i^\dagger \rangle (\hat{a}_j - \langle \hat{a}_j \rangle) \\
&= \hat{a}_i^\dagger \langle \hat{a}_j \rangle + \hat{a}_j \langle \hat{a}_i^\dagger \rangle - \langle \hat{a}_i^\dagger \rangle \langle \hat{a}_j \rangle
\end{aligned}$$

The effect of this approximation is that we neglect correlation between neighboring sites, which comes from $\delta \hat{a}_i^\dagger \delta \hat{a}_j$. The on-site correlation between occupation number basis states will be still present in general. The approximation allows us to rewrite the Bose-Hubbard Hamiltonian as a sum of local Hamiltonians. We assume the system is homogeneous so that the mean field is uniform across the sites: $\langle \hat{a}_i \rangle = \alpha$. Then

$$H \approx \sum_i h_i = \sum_i -zt (\alpha \hat{a}_i^\dagger + \alpha^* \hat{a}_i - |\alpha|^2) + \frac{U}{2} \hat{n}_i (\hat{n}_i - 1)$$

where z is the coordination number of the lattice. We insert the chemical potential μ as a Lagrange multiplier that controls the average occupation number, so that we do not have to diagonalize the Hamiltonian under the constraint of a fixed number of particles. Then to find the ground state of the system, it remains to minimize the energy of the on-site Hamiltonian $h - \mu \hat{n}$ with α as our variational parameter, under the constraint $\langle \hat{a} \rangle = \alpha$:

$$h - \mu \hat{n} = -zt(\alpha \hat{a}^\dagger + \alpha^* \hat{a} - |\alpha|^2) + \frac{U}{2} \hat{n}(\hat{n} - 1) - \mu \hat{n}$$

5.2.1 Perturbative approach

We start the analysis from a Mott insulating state with $\langle \hat{n} \rangle = n$, $\alpha = 0$ and apply perturbation theory to find the energy shift due to the $(\alpha \hat{a}^\dagger + \alpha^* \hat{a})$ term [75]. It is clear that only the even-order perturbation terms survive. We apply the perturbation

theory up to the fourth order.

$$\begin{aligned}
E(\alpha) &= a_0 + a_2|\alpha|^2 + a_4|\alpha|^4 + \mathcal{O}(|\alpha|^6) \\
a_0 &= -\mu n + \frac{U}{2}n(n-1) \\
a_2 &= \left(\frac{n+1}{\mu - nU} + \frac{n}{-\mu + (n-1)U} \right) (zt)^2 + zt \\
a_4 &= (zt)^4 \left(\frac{(n-1)n}{(2nU - 3U - 2\mu)(\mu - nU + U)^2} \right. \\
&\quad - \frac{(n+1)(n+2)}{(2nU + U - 2\mu)(\mu - nU)^2} \\
&\quad \left. - \frac{(\mu + U)}{(\mu - nU)(\mu - nU + U)} \left(\frac{n}{(\mu - nU + U)^2} + \frac{n+1}{(\mu - nU)^2} \right) \right)
\end{aligned}$$

The expansion of the variational energy in terms of powers of $|\alpha|^2$ is reminiscent of the phenomenological Landau theory of second order phase transitions, which predicts a phase transition when a_2 changes sign if a_4 stays positive [76]. More specifically, $|\alpha|^2 = 0$ for $a_2 > 0$ and $|\alpha|^2 = -a_2/(2a_4)$ for $a_2 < 0$. This is the spontaneous symmetry breaking of a continuous symmetry, which is the global U(1) symmetry ($\hat{a} \rightarrow e^{i\theta}\hat{a}$) in our problem. Before we demonstrate the positivity of a_4 , first consider the equation $a_2 = 0$ to find the phase boundary line. The equation yields the boundary lines defined by

$$\mu_{\pm}/(zt) = \frac{1}{2} \left((2n-1)\frac{U}{zt} \pm \sqrt{\frac{U}{zt} \left(-4n + \frac{U}{zt} - 2 \right) + 1 - 1} \right)$$

These boundary lines define lobe-like regions in which the system enters a Mott insulator phase with integral filling factor, as shown in Fig. 5-1. The positivity of the quartic term a_4 can be checked by looking at Fig. 5-1(a). For any choice of integer $n \geq 1$, the corresponding μ is bounded as $(n-1)U < \mu < nU$, where $(n-1)U$ and nU define the zeroth-order phase boundary lines. Given a fixed n one can apply this bound for μ to the expression of $a_4(n, U, \mu)$ and confirm that $a_4 > 0$, although the check is tedious and can be done more conveniently with a computer algebra system (e.g. using Mathematica's `Reduce` function for checking compatibility of inequalities).

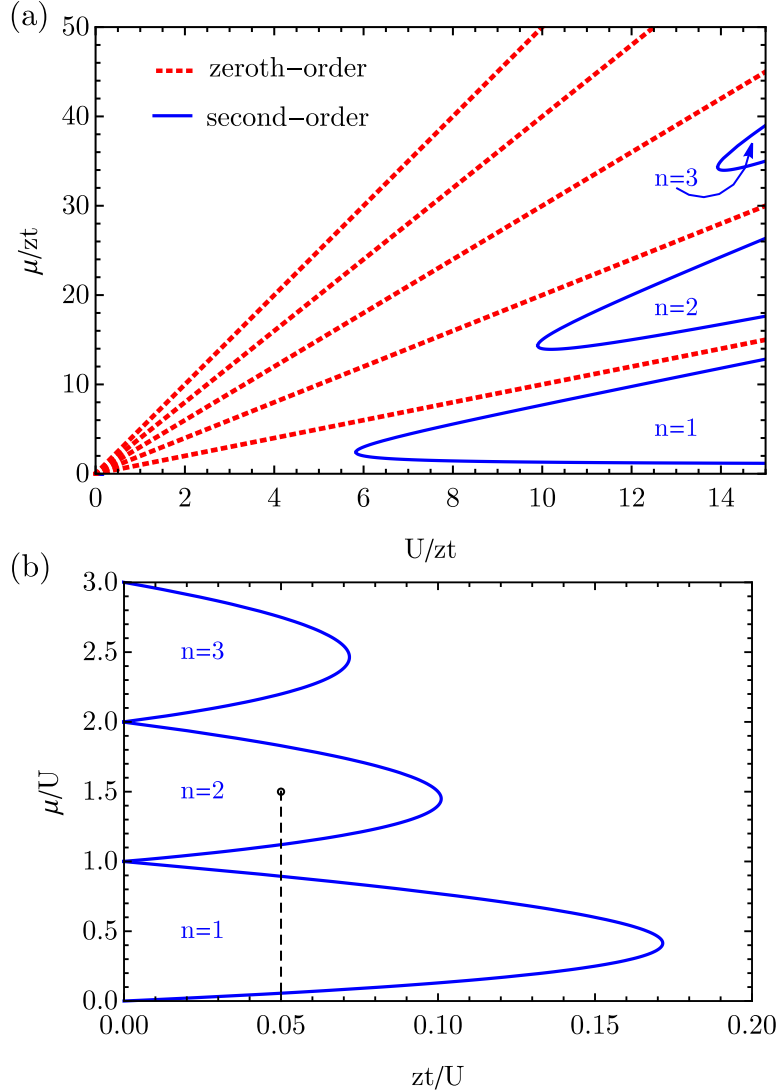


Figure 5-1: Mean-field phase diagram of the Bose-Hubbard Hamiltonian. (a) Phase diagram on the $(U/zt, \mu/zt)$ parameter space. The dotted red lines show the phase boundary lines for the zeroth-order calculation, where the lines are determined by $a_0(\mu, U, n) = a_0(\mu, U, n + 1)$. In the zeroth-order level, the filling factor n is always an integer. The solid blue lines show the phase boundary lines for the second-order calculation, where the lines are determined by $a_2(\mu, U, n) = 0$. Outside the lobe regions the superfluid order parameter takes a non-zero value and the filling factor is no longer an integer in general. (b) Phase diagram on the $(zt/U, \mu/U)$ parameter space. Outside the lobe regions the superfluid order parameter is nonzero. The black dotted line shows an example of the local chemical potential variation in an inhomogeneous system. Under the local density approximation, the local filling factor is determined by local $(zt/U, \mu/U)$ sampling the phase diagram.

The deviation of the filling factor away from an integral value in the superfluid region can be also calculated in this framework. We make use of the definition of the chemical potential as a Lagrange multiplier for the average occupation number: $\langle \hat{n} \rangle \equiv -\partial \langle H \rangle / \partial \mu = -\partial E(\alpha) / \partial \mu$. When the order parameter is zero, $E(\alpha) = E(0) = a_0$ and $\langle \hat{n} \rangle = n = 0, 1, 2, \dots$. When the order parameter is nonzero, $E(\alpha) = a_0 - a_2^2 / (4a_4)$ and thus

$$\begin{aligned} \langle \hat{n} \rangle &= n + \left(\frac{a_2}{2a_4} \right) \frac{\partial a_2}{\partial \mu} - \left(\frac{a_2}{2a_4} \right)^2 \frac{\partial a_4}{\partial \mu} \\ &= n - |\alpha|^2 \frac{\partial a_2}{\partial \mu} - |\alpha|^4 \frac{\partial a_4}{\partial \mu} \end{aligned}$$

The slope $\partial a_2 / \partial \mu$ near the phase transition can be visually inferred from the phase boundary lines in Fig. 5-1. The value of a_2 inside the lobe regions is negative, while it is positive outside those regions. By fixing (t, U) and varying μ , we scan the phase diagram vertically. As we increase μ , if we enter a lobe region from outside, $\partial a_2 / \partial \mu < 0$ and the filling factor is slightly less than the integral value associated with the lobe. On the other hand, if we exit a lobe region as we increase μ , $\partial a_2 / \partial \mu > 0$ and the filling factor is slightly larger than the integral value associated with the lobe. These two regions of $\langle \hat{n} \rangle < n$ and $\langle \hat{n} \rangle > n$ eventually merge near the tip of the $\langle \hat{n} \rangle = n$ lobe, whose location is defined by $\partial a_2 / \partial \mu = 0$. Figure 5-2 shows a perturbative calculation of $\langle \hat{n} \rangle$ around the $n = 1$ and $n = 2$ Mott lobes for $U/zt = 11$. Note that only the $\partial a_2 / \partial \mu$ contribution is kept, as the $\partial a_4 / \partial \mu$ term is highly divergent near the point $\mu = nU$. The high-order non-degenerate perturbation theory we employed does not work near the zeroth-order phase boundaries $\mu = nU$ because of energy degeneracy between n and $n + 1$ phases at those boundaries [75].

5.2.2 Numerical diagonalization

The perturbative approach to the mean field phase diagram yields closed-form expressions that give many insights into the Bose-Hubbard Hamiltonian, but in order to obtain more accurate results, especially near the degeneracy points $\mu = nU$, we

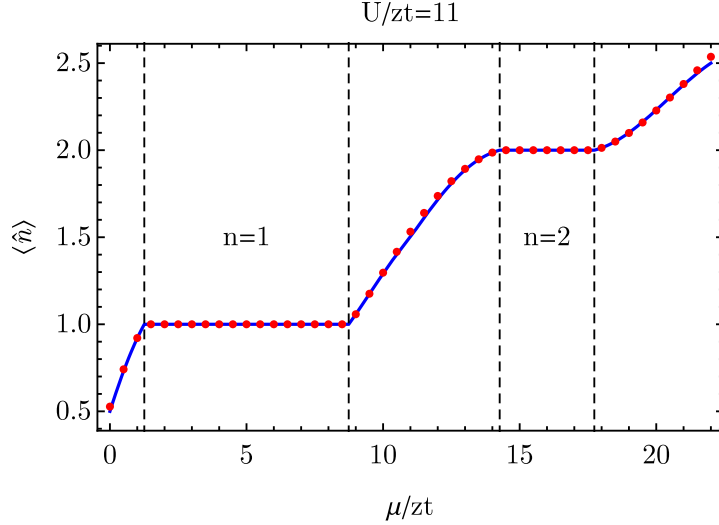


Figure 5-2: Calculation of the average filling factor $\langle \hat{n} \rangle$ around the $n = 1$ and $n = 2$ Mott lobes, for $U/zt = 11$. The blue solid line represents the perturbative calculation and the red dots are from the numerical diagonalization as described in Section 5.2.2, which agrees well with the perturbative calculation. However, for the (nondegenerate) perturbative calculation, the $\partial a_4 / \partial \mu$ contribution is ignored as it has a highly singular behavior near the degeneracy point $\mu = nU$. The dotted lines mark the Mott lobe regions where the average filling factor is an integer. In an inhomogeneous system, the local chemical potential varies from a maximal value at the center to zero at the edge, and thus the radial profile of the system has a “wedding cake” structure of alternating superfluid and Mott-insulating regions [77–80].

have to employ numerical diagonalization of the Hamiltonian matrix. We assume a variational wavefunction of the form $|\Psi_{MF}\rangle = \prod_i \sum_{n=0}^{\infty} f_n |n\rangle$. The Hamiltonian matrix takes the form

$$zt \begin{pmatrix} |\alpha|^2 & -\alpha & 0 & \cdots & 0 \\ \alpha^* & -\tilde{\mu} + |\alpha|^2 & -\sqrt{2}\alpha & \cdots & \vdots \\ 0 & -\sqrt{2}\alpha^* & -2\tilde{\mu} + \tilde{U} + |\alpha|^2 & \cdots & \vdots \\ \vdots & \vdots & \vdots & \ddots & -\sqrt{n}\alpha \\ 0 & \cdots & \cdots & -\sqrt{n}\alpha^* & -n\tilde{\mu} + \frac{\tilde{U}}{2}n(n-1) + |\alpha|^2 \end{pmatrix}$$

where $(\tilde{\mu}, \tilde{U}) = (\mu/zt, U/zt)$. The idea is to truncate the matrix at $n = n_{\max}$ and vary α until the lowest eigenvalue of the matrix reaches a minimal value for a given (μ, U) input [81]. The maximum occupation number n_{\max} is also increased until the

optimal value of α found converges to a steady value. For low filling numbers n_{\max} does not need to be higher than 5 unless U/zt is set to be very low (deep into the superfluid phase). An example of the calculation for $U/zt = 11$ is shown in Fig. 5-2, which actually agrees pretty well with the perturbative calculation.

5.2.3 Comparison to experiments

Because of the Gaussian envelopes of the lattice beams and the harmonic traps for confining atoms, the system is inhomogeneous, and the parameters (t, U, μ) vary across the atom cloud. As long as the variation is not too strong (relative changes being small over a lattice constant length scale), we can invoke a local density approximation and use the mean-field phase diagram to estimate quantities such as $\langle \hat{n} \rangle$. With the numerical diagonalization technique, we can generate a detailed map of $\langle \hat{n} \rangle$ as a function of μ/U and zt/U . In many BEC experiments, the BEC is initially trapped in a harmonic trap and is eventually loaded to an optical lattice. The variation of the local chemical potential, which follows the shape of the harmonic trap in the Thomas-Fermi regime, will be present in the atomic cloud at the onset of the phase transition. We can estimate how many distinct Mott lobes are present and how many atoms are within each lobe by integrating the average filling factor across the phase diagram. To do the integration, we traverse the $(\mu/U, zt/U)$ trajectory made when one moves from the center of the trap towards the edge, such as the dotted line in Fig. 5-1(b) or the x -axis in Fig. 5-2. The computation of the estimated atom numbers in the different Mott lobes is summarized as follows:

1. Construct a lookup table of lattice parameters $(V_L, t, \int |w(x)|^4 dx)$. V_L denotes optical lattice depth in units of recoil energy E_R . The lookup table can be generalized by interpolation to a function with V_L as the argument. The quantity $\int |w(x)|^4 dx$ is used to compute the local value of U once the three-dimensional coordinate in the optical lattice is provided.
2. Construct a lookup table of Bose-Hubbard parameters $(zt/U, \mu/U, \langle \hat{n} \rangle)$ with the numerical diagonalization technique.

3. Provide the harmonic confinements due to the Gaussian laser beams and the background magnetic field. To find the Gaussian beam contributions to the overall confinement, one needs an accurate knowledge of one of either combination: input power and Gaussian beam waist, or input power and dipole oscillation frequencies. The dipole oscillation frequencies can be easily measured by kicking the atom cloud with a displaced version of each beam. Since frequency can be more easily and precisely measured than beam waist, we usually use the latter combination. We can also infer the corresponding Gaussian beam waist from the said combination, and we make sure the inferred value is consistent with the optical layout.
4. Construct a function that calculates the local variation of $(zt/U, \mu/U)$ from the value at the center of trap. The μ/U variation is directly given by the change in the total potential depth, and zt/U is computed from the change in the lattice depth.
5. Integrate $\langle \hat{n} \rangle$ as a function of local $(zt/U, \mu/U)$ throughout the volume inside the trap.

Many quantum simulation experiments that use a Mott insulating phase as the restricted Hilbert space require a strict bound on the maximal filling factor. There are experimental techniques such as interaction-induced clock shift spectroscopy [77], spin-changing collisions [78], interaction blockade [79], and quantum gas microscopy [80], that can directly show the *in-situ* distribution of the filling factor. However, such techniques require special setups or time-consuming data acquisitions. The value of the numerical simulation of the filling factor distribution is that it gives a quick estimate of the maximal filling factor based on the total atom number measured by imaging.

We have checked the computation procedure by using the provided lattice depths and beam profile data in Ref. [79] and reproducing the same simulation result as shown in Fig. 4(a) of the reference. For comparison against our own experiment, see Fig. 5-3. In the Figure, we estimate the Mott lobe populations in a three-dimensional lattice

formed by 1064 nm beams with lattice depths of $20 E_R$. Although the experiment makes use of a deeper lattice depth ($35 E_R$), a lower lattice depth was chosen as the density is expected to be frozen before the ramp-up of the lattice depths completes. By using the measurement protocol described in Section 7.1, the result of the simulation can be compared to the experiment by measuring the atom number at which $\langle \hat{n} \rangle = 2$ lobe disappears, and also by measuring the rate at which the $\langle \hat{n} \rangle = 2$ lobe fraction or the total doublon fraction grows as a function of total atom number. However, as Fig. 5-3(b) shows, we could not bring the measured non-singlon fraction of the Mott insulator into an agreement with the estimated value as a function of measured total atom number - we had to introduce a “fudge factor” of two into the atom number calibration to produce a better agreement. One could argue that an incorrect effective absorption cross section was used for the number calibration, but we made independent estimates of the atom number by measuring the released energy from BEC expansion, and the independent estimates were in good agreement with the absorption imaging estimates. A likely explanation for the discrepancy is that the lattice loading procedure is not adiabatic and hence the density distribution frozen in the Mott insulating phase is not in equilibrium, resulting in higher non-singlon fractions.

It must be emphasized that the mean-field approximation becomes unreliable at low dimensions where correlations become more important [76]. Indeed, the one-dimensional superfluid to Mott insulator transition happens much earlier at $(t/U)_c \approx 0.3$ instead of ≈ 0.086 as predicted by the mean-field calculation [82]. Also, the Mott lobe regions appear sharply pointed.

5.3 Corrections due to higher bands

We are interested in the corrections to Hubbard parameters because the parameters of the effective spin models we would like to study depend sensitively on t and U . In particular, the spin exchange parameter is $J = 4t^2/U$. Typically the calculation of t and U uses Wannier orbitals $w(x)$ calculated from the lowest Bloch band of the

lattice in the absence of interaction. However, on-site interactions modify the Wannier orbitals if a site is occupied by more than one atom [73,74]. An intuitive picture is that the repulsive interaction energy encourages atoms to separate, flattening the density distribution near the center of the lattice site. This modified density distribution can also be interpreted as the on-site wavefunction being a superposition of Wannier orbitals from different Bloch bands. In the case of a cubic lattice, the expansion of the field operator in Section 5.1 is now generalized to

$$\hat{\psi}(\vec{r}) = \sum_i \sum_{m_x, m_y, m_z}^{m_{\max}} \hat{a}_{(m_x, m_y, m_z), i} w_{(m_x, m_y, m_z), i}(\vec{r}) \quad (5.2)$$

where i is the lattice site index, and $w_{(m_x, m_y, m_z), i}(\vec{r}) = w_{m_x, i}(x)w_{m_y, i}(y)w_{m_z, i}(z)$ is the three-dimensional Wannier orbital at lattice site i constructed from the m_α^{th} Bloch band for $\alpha = x, y, z$. For practical purposes we introduce a cutoff for the maximum band number in each direction, denoted by m_{\max} . Because of the three-dimensional nature of the interaction, inclusion of Bloch bands beyond the ground band leads to an exponentially growing on-site Hilbert space. For n atoms in a single lattice site, each atom can occupy any of the m_{\max}^3 available states. The total number of distinct many-body states of n atoms in a single lattice site is

$$\frac{(n + m_{\max}^3 - 1)!}{n!(m_{\max}^3 - 1)!}$$

If $m_{\max} = 4$, then the dimension of the on-site Hilbert space is 2080 for $n = 2$ and 45760 for $n = 3$. A physical argument for setting m_{\max} low is that the higher Bloch bands are not classically bound (e.g. the third band in Fig. 4-1) and are prone to loss due to lack of confinement, and hence they contribute minimally to the renormalization of the on-site density distribution [83].

The full exact diagonalization of the on-site problem is computationally challenging³. However, standard second-order perturbation theory can be used, and its use is justified because the final answer yielded by the calculation does not show a strong

³For more information on how to implement the numerical diagonalization, see Ref. [84]

modification of the Hubbard parameters for typical experimental conditions [85]. The on-site interaction energy modified by the inclusion of higher-band Wannier orbitals is

$$U^{(2)} = U^{(0)} - \sum_{\vec{m}_1, \vec{m}_2} \frac{g^2}{4(E_{bg} - \Delta E_U^{(0)})} \left(\int w_{\vec{m}_1}^*(r) w_{\vec{m}_2}^*(r) [w_{(0,0,0)}(r)]^2 d^3r \right)^2 \\ \times |\langle 1_{\vec{m}_1}, 1_{\vec{m}_2}, (n-2)_{(0,0,0)} | \hat{a}_{\vec{m}_1}^\dagger \hat{a}_{\vec{m}_2}^\dagger \hat{a}_{(0,0,0)} \hat{a}_{(0,0,0)} | n_{(0,0,0)} \rangle|^2$$

where n is the number of atoms at the site, $\vec{m}_i = (m_{x,i}, m_{y,i}, m_{z,i})$ are the new band indices for two atoms after the interaction, E_{bg} is the sum of the energy band gaps from all three directions, and $\Delta E_U^{(0)}$ is the magnitude of the change in the zeroth-order interaction energy of m atoms after promoting 2 atoms to (possibly) different Wannier orbitals. Note that \vec{m}_1 and \vec{m}_2 cannot be simultaneously be equal to $(0, 0, 0)$. Also note that the provided expressions are only valid for spin-polarized systems. For spinful systems, g is generalized to $g_{\sigma\sigma'}$ and appropriate changes also need to be made to the bosonic stimulation factor $\langle \dots | \hat{a}^\dagger \hat{a}^\dagger \hat{a} \hat{a} | \dots \rangle$. Note that E_{bg} is typically much larger than $U^{(0)} = gn(n-1)/2 \int |w(r)_{(0,0,0)}|^4 d^3r$ and the resulting smallness of $g^2(\int \dots)^2/(E_{bg})$ ensures that we stay in the regime of validity for second-order perturbation theory.

The calculation can be simplified by making use of the inversion symmetry of the Wannier orbitals in a cubic lattice. The Wannier orbitals are even under inversion if the band index is even, and odd if the band index is odd. Therefore, only the band indices \vec{m}_1, \vec{m}_2 that satisfy $m_{\alpha,1} + m_{\alpha,2} \equiv 0 \pmod{2}$ ($\alpha = x, y, z$) enter into the calculation. Also, the calculation of the bosonic stimulation factor $\langle \dots | \hat{a}^\dagger \hat{a}^\dagger \hat{a} \hat{a} | \dots \rangle$ can be reduced to four special cases:

1. $\vec{m}_1 = \vec{m}_2 = (0, 0, 0)$: the factor is $n(n-1)$.
2. $\vec{m}_1 = \vec{m}_2$ and $\vec{m}_1 \neq (0, 0, 0)$: the factor is $\sqrt{2n(n-1)}$.
3. $\vec{m}_1 \neq \vec{m}_2$ and [$\vec{m}_1 = (0, 0, 0)$ or $\vec{m}_2 = (0, 0, 0)$]: the factor is $\sqrt{n(n-1)}$.
4. $\vec{m}_1 \neq \vec{m}_2$ and $\vec{m}_{1,2} \neq (0, 0, 0)$: the factor is $\sqrt{n(n-1)}$.

The computation of $\Delta E_U^{(0)}$ is straightforward in principle but can be lengthy in formulation into a code. However, calculations suggest that its contribution to the final answer is negligible ($E_{bg} \gg \Delta E_U^{(0)}$) and can be ignored for simplicity.

We show the result of the perturbative calculation for the correction to U in Figure 5-4. We see that for two ($n = 2$) or three atoms ($n = 3$) per site, the change in U is within 10%. The dominant contributions to the energy correction come from processes where one of the atoms jumps to a band with index number 2 or two of the atoms jump to a band with index number 1. As for a comparison to an exact diagonalization solution, we note that if we use $V_{\text{transverse}} = V_{\text{longitudinal}} = 35 E_{R,754\text{nm}}$, $a_s/\lambda = 0.007$, and $m_{\text{max}} = 4$, we obtain the correction to U be 0.93, 0.91, 0.89 for $n = 2, 3, 4$ whereas Ref. [72] obtains 0.9, 0.875, 0.85 for $n = 2, 3, 4$. So second order perturbation theory misses 3 to 4% extra correction but nonetheless yields a good estimate of the magnitude of the corrections.

We now consider corrections to the tunneling parameter t . There are two main corrections: the first correction is the so-called bond-charge tunneling [73] and the second correction is the multi-orbital tunneling due to the admixture of higher-band orbitals. The bond-charge effect arises from the terms of the form $(g/2)\hat{a}_i^\dagger(\hat{a}_j^\dagger\hat{a}_j)\hat{a}_j$ when we insert Eq. 5.2 into Eq. 5.1. We note that the bond-charge tunneling is still present without the inclusion of higher bands and was simply ignored in the derivation of the Bose-Hubbard Hamiltonian in Sec. 5.1 in order to keep the parameters density-independent. The contribution of the bond-charge effect to the tunneling t without inclusion of the higher-band orbitals is

$$-g \left(\int w(r - \delta r)^* w(r)^* w(r) w(r) d^3r \right) (\hat{n}_i + \hat{n}_j - 1)$$

where i, j are lattice site indices for nearest neighbors and δr is a translation by one lattice constant along one of the three directions. For the lattice parameters specified in Fig. 5-4, the bond-charge effect enhances t by 17 to 18% for $n_i = n_j = 2$ as the longitudinal lattice depth is varied. The inclusion of higher-band orbitals into the on-site wavefunctions allows multi-orbital tunneling and also corrects the bond-charge

effect. The admixture of higher-band orbitals can be determined again by second order perturbation theory, and the modified onsite wavefunction $|\tilde{n}_{(0,0,0)}\rangle$ is expressed as:

$$|\tilde{n}_{(0,0,0)}\rangle = |n_{(0,0,0)}\rangle - \sum_{\vec{m}_1, \vec{m}_2} \frac{g}{2(E_{bg} - \Delta E_U^{(0)})} \left(\int w_{\vec{m}_1}^*(r) w_{\vec{m}_2}^*(r) [w_{(0,0,0)}(r)]^2 d^3r \right) \hat{a}_{\vec{m}_1}^\dagger \hat{a}_{\vec{m}_2}^\dagger (\hat{a}_{(0,0,0)})^2 |n_{(0,0,0)}\rangle$$

Note that \vec{m}_1 and \vec{m}_2 cannot be simultaneously be equal to $(0, 0, 0)$. For our typical lattice conditions (see Fig. 5-4) with two atoms per lattice site, the total population in the excited bands is between 0.1 and 0.2%. For the multi-orbital tunneling, we only consider tunneling processes between equal orbitals (equal band indices)⁴. With this constraint, the matrix element of the multi-orbital tunneling process for $|\tilde{n}_L, \tilde{n}_R\rangle \rightarrow |\tilde{n}_L - 1, \tilde{n}_R + 1\rangle$ can be expressed as follows:

$$t_{\tilde{n}_L, \tilde{n}_R}^{MO} = \frac{1}{\sqrt{n_L(n_R + 1)}} \sum_{\vec{m}} t_{\vec{m}} \langle \tilde{n}_R + 1 | \hat{a}_{R, \vec{m}}^\dagger | \tilde{n}_R \rangle \langle \tilde{n}_L - 1 | \hat{a}_{L, \vec{m}} | \tilde{n}_L \rangle$$

where $\hat{a}_{\vec{m}}$ is the annihilation operator for a Wannier orbital with band index \vec{m} and $t_{\vec{m}}$ is the zeroth-order tunneling matrix element for Wannier orbitals with band index \vec{m} , which becomes exponentially larger as the band index increases along the considered tunneling direction. For $\tilde{n}_L = \tilde{n}_R = 2$, $t_{2,2}^{MO}$ is evaluated to be

$$t_{\vec{0}} + \sum_{\vec{m} \neq \vec{0}} 8t_{\vec{m}} c_{\vec{0}, \vec{m}}^{(2)} c_{\vec{0}, \vec{m}}^{(3)*}$$

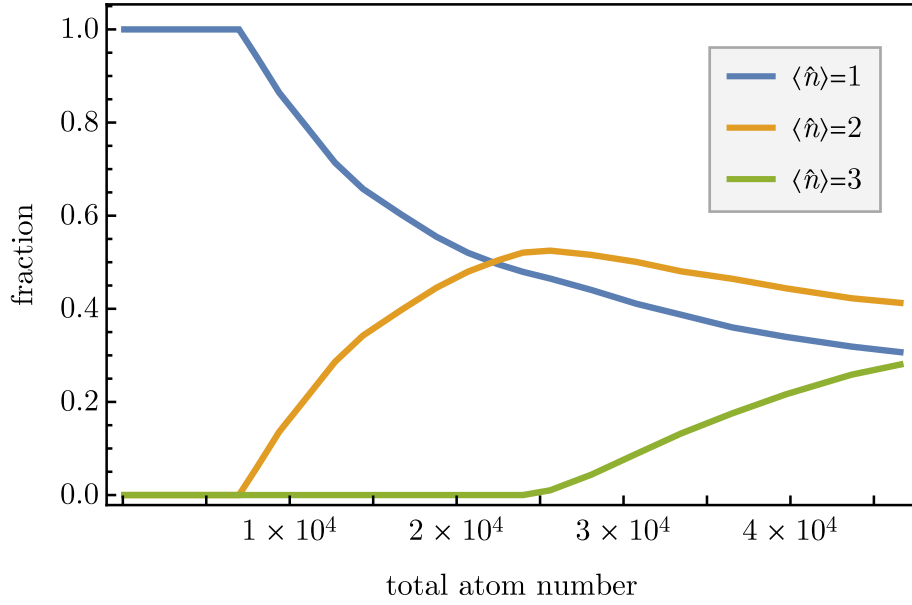
where $\vec{0} = (0, 0, 0)$ and $c_{\vec{0}, \vec{m}}^{(n)}$ is the short-hand symbol for the admixture coefficient calculated for n atoms per site:

$$-\frac{g}{2(E_{bg} - \Delta E_U^{(0)})} \left(\int w_0^*(r) w_{\vec{m}}^*(r) [w_{(0,0,0)}(r)]^2 d^3r \right)$$

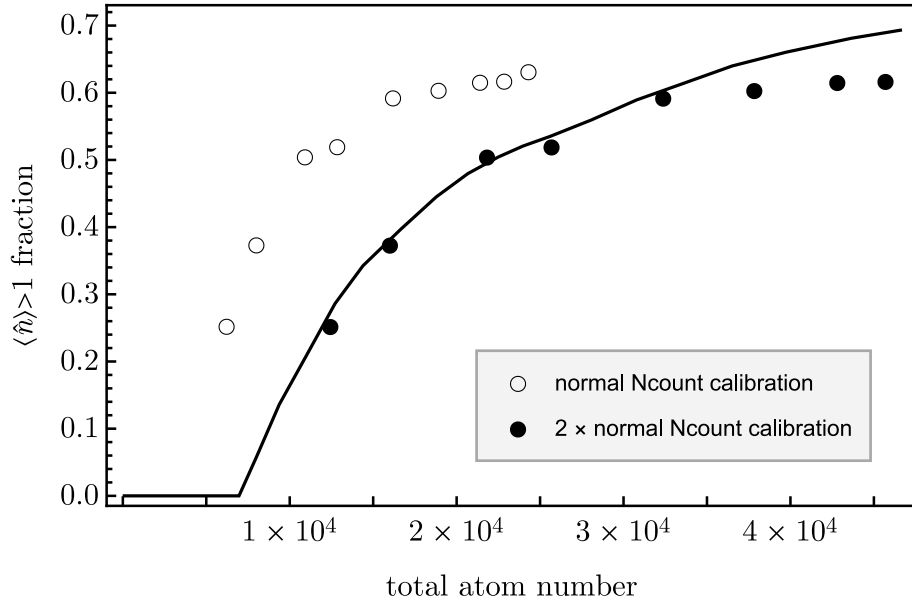
⁴Ref. [73] claims that tunneling between unequal orbitals is zero because of orthogonality relations between the Wannier orbitals. However, this is not true; orthogonality relations only hold for overlaps between Wannier orbitals. The insertion of the tunneling Hamiltonian $-\hbar^2/2m\nabla^2 + V(r)$ inside the overlap integral no longer yields zero for unequal orbitals. However, we expect tunneling between unequal orbitals to be highly off-resonant because of the large energy band gaps, and hence it is appropriate to ignore them.

The dependence of $c_{0,\vec{m}}^{(n)}$ on the atom number n is hidden in the denominator $E_{bg} - \Delta E_U^{(0)}$. The result is plotted in Fig. 5-5 as a function of the longitudinal lattice depth.

As a result of the correction, the spin exchange $4t^2/U$ is likely to be enhanced by 20 to 30% compared to the bare value in typical lattice depths. However, such a deviation can be also explained by less than 10% uncertainty in the lattice depth, since t depends exponentially on the lattice depth. Therefore, we do not consider the corrections in the following discussions given the noisiness of the data, but they need to be taken into account once the data is precise enough and if one wants to check the scaling of the exchange parameter with respect to the lattice depth.



(a)



(b)

Figure 5-3: Simulation of the Mott lobe populations in three-dimensional $20 E_{R,1064 \text{ nm}}$ lattice. The $1/e^2$ beam waists for the lattice beams are: $w_{\text{Tool}} = 145 \mu\text{m}$, $w_{\text{Closest}} = 147 \mu\text{m}$, $w_{\text{Vertical}} = 268 \mu\text{m}$. The $1/e^2$ beam waists for the crossed dipole trap are $w_{\text{XODT}} = (528 \mu\text{m}, 50 \mu\text{m})$, $w_{\text{VD}} = 94 \mu\text{m}$ (see Fig. 2-2 for the beam geometries). (a) Total atom number vs. Mott lobe populations. (b) Measured non-singlon ($\langle \hat{n} \rangle > 1$) fraction as a function of atom number vs. simulated non-singlon fraction based on beam parameters. A fudge factor has to be applied to the atom number conversion to bring the experiment and the simulation to a better agreement, although there is no evidence to suggest that the absorption imaging calibration is off.

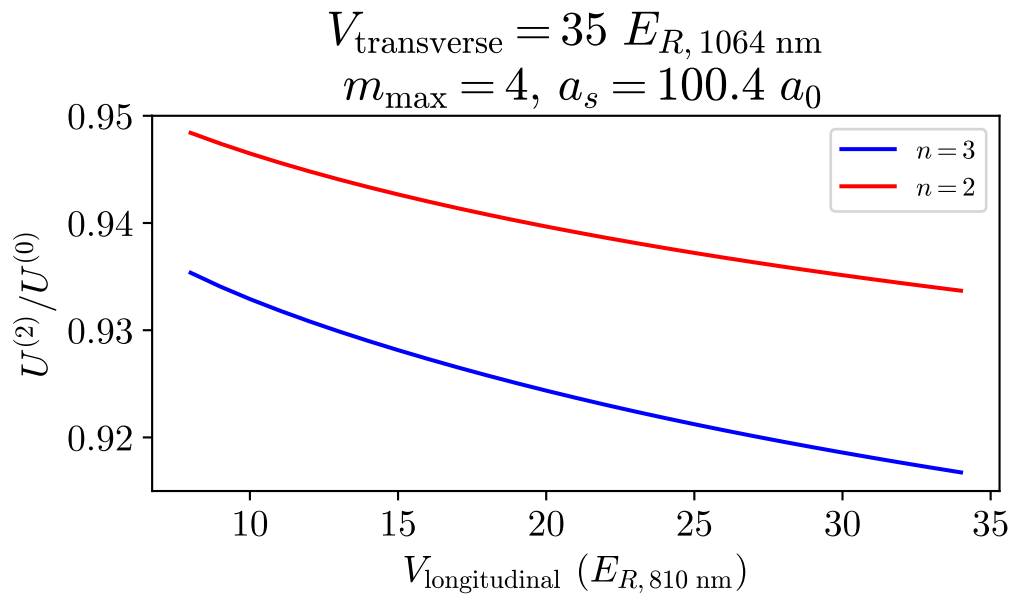


Figure 5-4: Perturbative calculation of correction to Hubbard interaction energy U due to inclusion of higher-band Wannier orbitals. The lattice depth is fixed to $35 E_{R, 1064 \text{ nm}}$ along the transverse directions and is varied along the longitudinal direction, where the 810 nm lattice is installed. The highest band index n_{max} we allow is 4, and the number of atoms occupying a single lattice is either 2 (red) or 3 (blue).

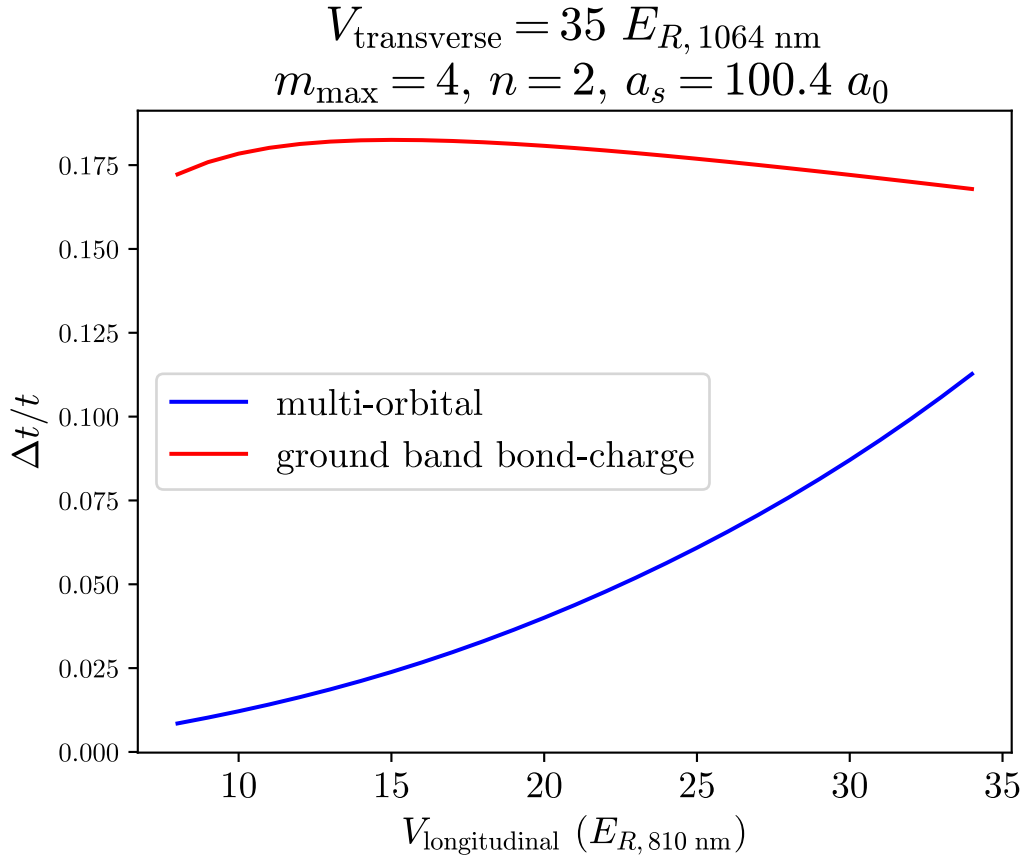


Figure 5-5: Perturbative calculation of correction to tunneling amplitude t due to inclusion of higher-band Wannier orbitals and the bond-charge effect. We do not consider multi-orbital correction to the bond-charge effect. The assumed atom number per site is two.

Chapter 6

Quantum Magnetism

Quantum magnetism is a vast field of study that investigates magnetic phenomena where quantum effects play an important role. It is highly relevant to the study of strongly correlated systems with strong interactions and has inspired many new theoretical methods as well as experiments [86, 87]. Often the physics of quantum magnetism is distilled into spin models with several parameters, such as exchange interaction strength and anisotropy strength. A spin model is classical if the spin is treated as a classical vector, whereas it is quantum mechanical if the spin is treated as a quantum spin operator (e.g. Pauli matrices for spin-1/2). Because of the non-commutativity of the spin operators, quantum fluctuations play an important role in spin ordering within quantum spin models, whereas classical spin models have no fluctuation at zero temperature, by definition.

While classical spin models constitute a rich subject on their own [76], quantum spin models intersect with many modern research areas of physics such as quantum phase transitions [10], quantum integrability [11], and quantum simulation [88]. This chapter will focus on introducing the quantum Heisenberg spin model and its realization with neutral atoms in optical lattices [20, 21].

6.1 Derivation of an effective Hamiltonian

We are interested in deriving a Heisenberg spin model. For spin-1/2 a canonical model is

$$H = J_{xy} \sum_{\langle i,j \rangle} (S_{i,x}S_{j,x} + S_{i,y}S_{j,y}) + J_z \sum_{\langle i,j \rangle} S_{i,z}S_{j,z} - h_z \sum_i S_{i,z}$$

which is known as the *XXZ* spin-1/2 model, and for spin-1 a canonical model is

$$H = J \sum_{\langle i,j \rangle} \vec{S}_i \cdot \vec{S}_j + D \sum_i (S_{i,z})^2 - h_z \sum_i S_{i,z}$$

where $S_{i,\alpha=x,y,z}$ are spin operators in the three orthogonal directions at the site i . Note that the spin-1/2 model can have an anisotropy in the exchange strength (i.e. $J_{xy} \neq J_z$), whereas the spin-1 model has a type of anisotropy known as the single ion-type anisotropy (SIA) in material science literature [89]. The anisotropy term $(S_{i,z})^2$ cannot exist in spin-1/2 because it evaluates to a constant term. For completeness, the $(S_z)^2$ term is known as uniaxial single ion anisotropy; another SIA term is $(S_{i,x}^2 - S_{i,y}^2)$, which evaluates to a null term in spin-1/2. While previous studies on the effective spin-1 model for a $\langle \hat{n} \rangle = 2$ bosonic Mott insulator considered an isotropic exchange interaction in combination with the SIA term [21–23], we show in Section 6.1.3 that an exchange anisotropy is also possible. We mention in passing that there are other but less common interactions such as the Kitaev exchange interaction on a honeycomb lattice [90] or the Dzyaloshinskii-Moriya interaction [91] but we do not consider those terms here.

6.1.1 Kinetic Exchange

When atoms in two distinct internal states ($|a\rangle$ and $|b\rangle$) are loaded into a deep optical lattice such that they enter a Mott insulating phase, first-order tunneling is prohibited by the high on-site interaction energy cost. The local density at each site is fixed to be an integer, meaning that if there are n atoms, it would require an energy of nU

to add an atom, where U is the on-site interaction energy. However, the spatial distribution of the $|a\rangle$ and $|b\rangle$ states can freely change by second-order tunneling, as shown in Fig. 6-1. This gives rise to a mapping from the low energy Hilbert space of the two-component Bose-Hubbard Hamiltonian to a quantum spin Hamiltonian. It is not difficult to see that if there are $n = n_a + n_b$ atoms per site, the on-site Fock state can be mapped to a spin with $S_z = (n_a - n_b)/2$. Second-order tunneling allows swapping of one $|a\rangle$ and one $|b\rangle$ between neighboring sites, and this process can be mapped to a spin flip-flop process described by the operator $S_i^+ S_j^- + \text{c.c.}$ In the field of quantum simulation with ultracold atoms, this exchange process by second-order tunneling has become to be known as superexchange [92], but in the field of solid-state physics the term superexchange technically refers to a fourth-order tunneling process, where electrons from separated transition metal ions hop to an intermediate oxygen atom bridging the two ions to exchange spins [93]. In accordance with the convention in solid state physics, we use the term kinetic exchange to describe the second-order tunneling process.

6.1.2 On-site anisotropy

In the limit of a very deep lattice where even the second-order tunneling becomes negligible, the many-body ground state is a product of \hat{S}_z eigenstates. Each \hat{S}_z eigenstate is associated with a spin-dependent on-site interaction energy $U_{\sigma\sigma'}$, ($\sigma, \sigma' \in a, b$). In the spin-model, the difference in the on-site interaction energies can be expressed by the sum of a single-ion anisotropy term and a fictitious magnetic field, $D(S_{z,i})^2 - h_z S_{z,i}$ (Fig. 6-2). Hence the realization of the $(S_z)^2$ term with ultracold atoms is rather simple, whereas in material science, the origin of the single-ion anisotropy term is more complicated as it involves second-order perturbation by spin-orbit coupling [89].

6.1.3 Formal mapping

With an intuitive idea of how a spin exchange operation is realized by second-order tunneling, we are ready to understand the formal procedure for deriving an effective

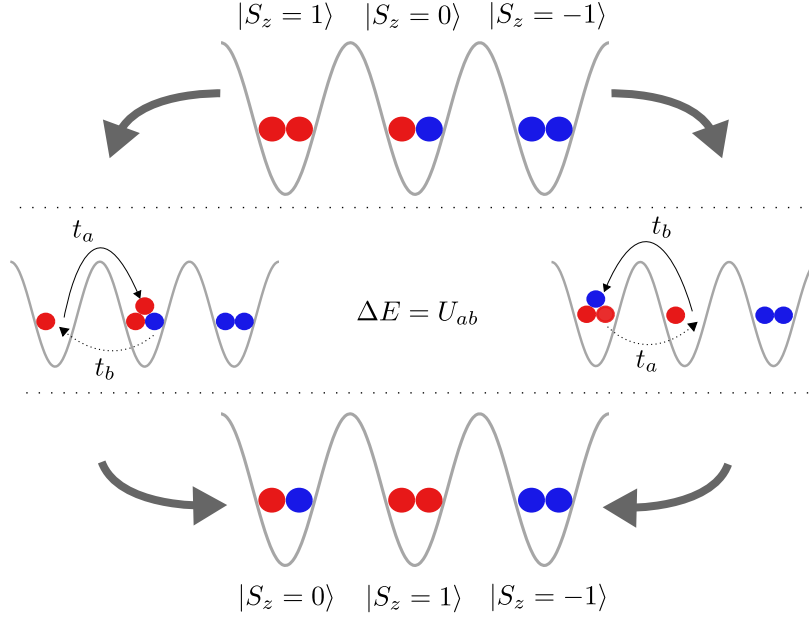


Figure 6-1: Kinetic exchange mechanism in a two-component Mott insulator with filling factor $\langle \hat{n} \rangle = 2$. Each atom can be in two internal states, $|a\rangle$ (red) or $|b\rangle$ (blue). The longitudinal spin S_z is given by $(n_a - n_b)/2$. The left well and the center well can exchange spins by second-order tunneling, for which there are two processes: either the $|b\rangle$ atom from the center tunnels to the left and then an $|a\rangle$ atom from the left tunnels to the center, or an $|a\rangle$ atom from the left tunnels to the center and then the $|b\rangle$ atom from the center tunnels to the left. For both processes, the second-order tunneling amplitude is $-2t_a t_b / U_{ab}$ where U_{ab} is the interaction energy between $|a\rangle$ and $|b\rangle$, and the net interaction can be summarized as a ferromagnetic spin exchange coupling with strength $J = -4t_a t_b / U_{ab}$.

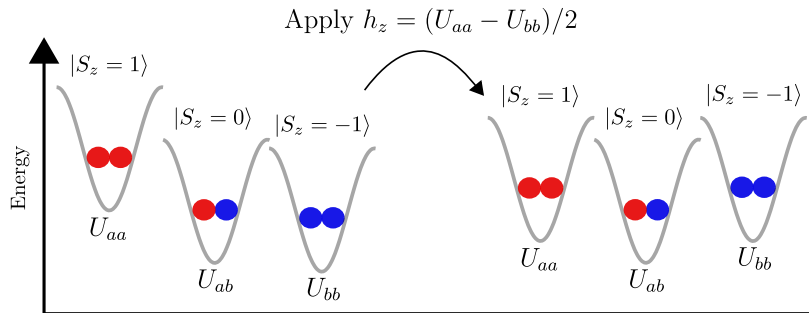


Figure 6-2: On-site anisotropy in a two-component Mott insulator with filling factor $\langle \hat{n} \rangle = 2$. In general, $U_{aa} \neq U_{bb}$. By applying a fictitious magnetic field $h_z = (U_{aa} - U_{bb})/2$ to the model, the energies of the different S_z states with respect to the reference energy U_{ab} can be expressed as $D(S_z)^2$, where $D = (U_{aa} + U_{bb})/2 - U_{ab}$.

spin Hamiltonian from the underlying Bose-Hubbard Hamiltonian¹.

¹Derivation of an effective Hamiltonian can be understood as a form of degenerate perturbation theory [94], and there are many different approaches. Here we just use one of them.

First, we can perform a unitary transformation from the original Hamiltonian to an effective Hamiltonian H_{eff} that does not have matrix elements between states that belong to different energy manifolds [95]. In the current context, the lowest energy manifold α consists of many-body states that do not have any quasiparticle-quasihole excitations. The higher energy manifolds β consist of states with different numbers of elementary excitations in the Mott phase, separated by an energy scale U . Assuming that the appropriate unitary transformation operator exists, we can express the matrix elements of the effective Hamiltonian for the lowest energy manifold H_{eff}^α up to second order in the off-diagonal term V ,

$$\begin{aligned} \langle i, \alpha | H_{\text{eff}}^\alpha | j, \alpha \rangle &= E_i \delta_{ij} + \langle i, \alpha | V | j, \alpha \rangle \\ &+ \frac{1}{2} \sum_{\beta \neq \alpha} \langle i, \alpha | V | k, \beta \rangle \langle k, \beta | V | j, \alpha \rangle \left(\frac{1}{E_i - E_k} + \frac{1}{E_j - E_k} \right) + \mathcal{O}(V^3) \end{aligned} \quad (6.1)$$

where the notation $|i, \alpha\rangle$ denotes the i -th state in the energy manifold α . In the current context, the zeroth-order energy E_i refers to the sum of chemical potential and interaction energy from all sites, and the off-diagonal operator V refers to the nearest-neighbor tunneling operator. This expansion has the same condition of validity as standard second-order perturbation theory, which is that the matrix elements of V be far smaller than the energy gap between the different energy manifolds. It must be noted that although H_{eff}^α has the same eigenenergy spectrum for the low energy subspace as the original Hamiltonian, its eigenstates will not be the same, as the excited states have been adiabatically eliminated in some sense. In the current context, even though the admixture of virtual particle-hole pairs is essential for second-order tunneling process to happen, it does not appear in the eigenstates of the effective Hamiltonian. Although this seems rather trivial, it can affect the validity of the effective Hamiltonian if the excited states are known to be lossy, e.g. due to three-body collisions.

We can view the basis states $|j, \alpha\rangle$ in two ways: as a basis state for the Bose-Hubbard Hilbert space with zero particle-hole pairs, or as a basis state for a spin Hamiltonian. For example, in a one-dimensional double-well system, $|j, \alpha\rangle$ could be

a Fock state with one $|a\rangle$ atom and one $|b\rangle$ atom per each site. If we use the mapping $S_z = (n_a - n_b)/2$, then this Fock state is equivalent to a $|S = 1, S_z = 0\rangle$ on each site of the double-well. If we evaluate $\langle i, \alpha | H_{\text{eff}}^\alpha | j, \alpha \rangle$ with respect to the Fock states using the second-order expansion above, the same number can be equated to a matrix element of a spin Hamiltonian between \hat{S}_z eigenstates [96]. Thus for each matrix element, we establish an equation between the Bose-Hubbard parameters and the Heisenberg spin model parameters:

$$f(t_a, t_b, U_{aa}, U_{ab}, U_{bb}) + Nc = g(J_{xy}, J_z, h_z, D, \dots) \quad (6.2)$$

where c is an energy offset we can add and N is the number of sites². Since interaction only happens between nearest neighbors, the set of equations for matrix elements between many-body states can be reduced to a set of equations for matrix elements between states spanning over two sites. For example, consider a diagonal matrix element where we reduce the triple well in Fig. 6-1 to the left-center double well and the final state is the same as the initial state shown. The equation we obtain is

$$U_{aa} + U_{ab} - t_b^2/U_{ab} - 4t_a^2/U_{ab} - 3t_a^2/(2U_{aa} - U_{ab}) + 2c = -h_z + D$$

Using such an approach, one can arrive at an exact mapping between the second-order expansion for the Bose-Hubbard Hamiltonian and the XXZ spin-1/2 Heisenberg Hamiltonian. The spin parameters for the spin-1/2 Hamiltonian are expressed as [97]

$$\begin{aligned} J_{xy} &= -4 \frac{t_a t_b}{U_{ab}} \\ J_z &= \frac{2(t_a^2 + t_b^2)}{U_{ab}} - 4 \left(\frac{t_a^2}{U_{aa}} + \frac{t_b^2}{U_{bb}} \right) \\ h_z &= 2z \left(\frac{t_a^2}{U_{aa}} - \frac{t_b^2}{U_{bb}} \right) \\ c &= z \left(\frac{t_a^2 + t_b^2}{4U_{ab}} + \frac{t_a^2}{2U_{aa}} + \frac{t_b^2}{2U_{bb}} \right) \end{aligned}$$

²This offset only appears on the diagonal matrix elements.

Note z is the number of nearest neighbors. However, that is not the case for spin-1, where the failure of an exact mapping is caused by having more constraints of the form $f(\dots) = g(\dots)$ than there are independent variables in the Heisenberg Hamiltonian. It may seem daunting to derive an effective spin-1 Hamiltonian that still holds approximately true. However, Jepsen *et al.* showed that the mapping to an XXX spin-1 Hamiltonian is approximately true at the degeneracy point defined by $t_a = t_b = t$, $U_{ab} = (U_{aa} + U_{bb})/2$ if the relative interaction imbalance $\delta = (U_{aa} - U_{bb})/(U_{aa} + U_{bb})$ remains small [97]. Furthermore, the error term to the spin Hamiltonian scales with δ^2 . If we define $1/U = 1/(2U_{aa}) + 1/(2U_{bb})$, the spin parameters for the spin-1 models at the degeneracy point $U_{ab} = (U_{aa} + U_{bb})/2$ are expressed as

$$\begin{aligned}
J &= -\frac{4t^2}{U} \\
D &= \frac{U_{aa} + U_{bb}}{2} - U_{ab} = 0 \\
h_z &= -U\delta \left(1 + z\frac{6t^2}{U^2}\right) \\
c &= -U + z\frac{4t^2}{U}
\end{aligned} \tag{6.3}$$

The full expressions for the second-order matrix elements calculated in Ref. [85] are shown in Fig. 6-3.

For our experiments, $\delta = 0$ but D can vary over a large range. As D deviates from zero, the SIA term $\propto \sum_i (S_{z,i})^2$ becomes active. We define $d = (U_{aa} + U_{bb})/2 - U_{ab}$ as the deviation from the degeneracy point $(U_{aa} + U_{bb})/2 = U_{ab}$, and obtain an expression for the strength of the SIA term D in terms of d and t^2/U . The full set of parameters,

consistent with Eq. 6.2 up to first order in d and zeroth order in δ are as follows:

$$\begin{aligned}
J_{xy} &= -\frac{4t^2}{U} \left(1 + \frac{d}{U}\right) = -\frac{4t^2}{U} \left(2 - \frac{U_{ab}}{U}\right) \\
J_z &= -\frac{4t^2}{U} \left(1 - \frac{d}{U}\right) = -\frac{4t^2}{U} \left(\frac{U_{ab}}{U}\right) \\
D &= d \left(1 - z \frac{2t^2}{U^2}\right) = \left(\frac{U_{aa} + U_{bb}}{2} - U_{ab}\right) \left(1 - z \frac{2t^2}{U^2}\right) \\
h_z &= 0 \\
c &= d - U + z \frac{4t^2}{U} = -U_{ab} + z \frac{4t^2}{U}
\end{aligned}$$

What is noticeable is the appearance of an exchange anisotropy, where $J_{xy} \neq J_z$, and a relative correction of order $(t/U)^2$ to the bare SIA strength $(U_{aa} + U_{bb})/2 - U_{ab}$ used in Refs. [21–23, 97].

$ n\rangle$ initial	$ m\rangle$ final	$\langle m H_{\text{eff}} n\rangle$	$\langle m H_{\text{eff}} n\rangle$ at degeneracy point	$\langle m H_{\text{eff}} n\rangle$ express as function of delta	$\langle m H_{\text{eff}} n\rangle$ adding overall energy offset E_0	$\langle m H_{\text{eff}} n\rangle$ substitute J	$\langle m H_{\text{eff}} n\rangle$ add fictitious magnetic field
		$\frac{12t^2}{U_{\uparrow\uparrow}}$	$\frac{12t^2}{U_{\uparrow\uparrow}}$	$-\frac{12t^2}{U}(1-\delta)$	$-\frac{4t^2}{U}(1-3\delta)$	$J(1-3\delta)$	J
		$-\left(\frac{4t^2}{U_{\uparrow\uparrow}} + \frac{4t^2}{U_{\downarrow\downarrow}}\right)$	$-\frac{8t^2}{U}$	$-\frac{8t^2}{U}$	0	0	0
		$\frac{12t^2}{U_{\downarrow\downarrow}}$	$\frac{12t^2}{U_{\downarrow\downarrow}}$	$-\frac{12t^2}{U}(1+\delta)$	$-\frac{4t^2}{U}(1+3\delta)$	$J(1+3\delta)$	J
		$-\left(\frac{3t^2}{2U_{\uparrow\uparrow}-U_{\uparrow\downarrow}} + \frac{5t^2}{U_{\downarrow\downarrow}}\right)$	$-\left(\frac{3t^2}{2U_{\uparrow\uparrow}-U_{\uparrow\downarrow}} + \frac{5t^2}{U_{\downarrow\downarrow}}\right)$	$-\frac{t^2}{U}(8-6\delta+4\delta^2+\dots)$	$\frac{4t^2}{U}\left(\frac{3\delta}{2}-\delta^2+\dots\right)$	$J(-3\delta/2+\delta^2+\dots)$	$J(\delta^2+\dots)$
		$-\left(\frac{3t^2}{2U_{\downarrow\downarrow}-U_{\downarrow\uparrow}} + \frac{5t^2}{U_{\uparrow\uparrow}}\right)$	$-\left(\frac{3t^2}{2U_{\downarrow\downarrow}-U_{\downarrow\uparrow}} + \frac{5t^2}{U_{\uparrow\uparrow}}\right)$	$-\frac{t^2}{U}(8+6\delta+4\delta^2+\dots)$	$-\frac{4t^2}{U}\left(\frac{3\delta}{2}+\delta^2+\dots\right)$	$J(3\delta/2+\delta^2+\dots)$	$J(\delta^2+\dots)$
		$-\left(\frac{2t^2}{2U_{\uparrow\downarrow}-U_{\uparrow\uparrow}} + \frac{2t^2}{2U_{\downarrow\uparrow}-U_{\downarrow\downarrow}}\right)$	$-\frac{4t^2}{U}$	$-\frac{4t^2}{U}$	$+\frac{4t^2}{U}$	$-J$	$-J$
		$\frac{4t^2}{U_{\uparrow\downarrow}}$	$\frac{4t^2}{U_{\uparrow\downarrow}}$	$-\frac{4t^2}{U}(1-\delta^2)$	$-\frac{4t^2}{U}(1-\delta^2)$	$J(1-\delta^2)$	$J(1-\delta^2)$
		$-\frac{4t^2}{U_{\downarrow\uparrow}}$	$-\frac{4t^2}{U_{\downarrow\uparrow}}$	$-\frac{4t^2}{U}(1-\delta^2)$	$-\frac{4t^2}{U}(1-\delta^2)$	$J(1-\delta^2)$	$J(1-\delta^2)$
		$-\left(\frac{2t^2}{U_{\uparrow\downarrow}+(U_{\uparrow\uparrow}-U_{\uparrow\downarrow})/2} + \frac{2t^2}{U_{\downarrow\uparrow}+(U_{\downarrow\downarrow}-U_{\downarrow\uparrow})/2}\right)$	$-\frac{4t^2}{U}$	$-\frac{4t^2}{U}$	$-\frac{4t^2}{U}$	J	J

Figure 6-3: Table of second-order matrix elements for a $\langle \hat{n} \rangle = 2$ Mott insulator. Figure 5 adapted from Ref. [97]. The arrow pointing up corresponds to the state $|S_z = 1\rangle = |a\rangle|a\rangle$ and the arrow pointing down corresponds to the state $|S_z = -1\rangle = |b\rangle|b\rangle$. The filled circle corresponds to the state $|S_z = 0\rangle = (|a\rangle|b\rangle + |b\rangle|a\rangle)/\sqrt{2}$.

For more general points in the parameter space where $\delta \neq 0$ and $d \neq 0$, one cannot arrive at a mathematically consistent set of parameters for the diagonal elements (processes described in the first six rows of Fig. 6-3) because Eq. 6.2 becomes overdetermined. A heuristic approach is to obtain an approximate solution to the overdetermined system of linear equations $A\vec{x} = \vec{b}$ by minimizing the difference $|A\vec{x} - \vec{b}|$.

The least-square solution obtained in such a way can be regarded as minimizing the overall energy difference between the spectrum of the proposed effective Hamiltonian and that of the true Hamiltonian. Using this approach, we obtain a set of parameters that are approximately true up to first orders of δ and d :

$$\begin{aligned}
J_{xy} &= -\frac{4t^2}{U} \left(1 + \frac{d}{U}\right) \\
J_z &= -\frac{4t^2}{U} \left(1 - \frac{d}{U}\right) \\
D &= d \left(1 - z \frac{2t^2}{U^2}\right) \\
h_z &= -U\delta \left(1 + z \frac{6t^2}{U^2} - z \frac{12}{5} \frac{t^2}{U^2} \frac{d}{U}\right) \\
c &= d - U + z \frac{4t^2}{U}
\end{aligned} \tag{6.4}$$

See Appendix C for the derivation. The only major difference from the ($d \neq 0, \delta = 0$) result is the appearance of a nonzero h_z , which scales linearly with δ . Indeed, if we set $d = 0$, we obtain the same result as Eq. 6.3. With this approximate solution, the error terms in the Hamiltonian scale with d^2 , δ^2 or $d\delta$. In Fig. 6-4 we demonstrate the effectiveness of the derived spin-1 model by comparing the numerically obtained low-energy eigenvalues to those of the corresponding Bose-Hubbard model. We see that after introducing the correct energy offset to the Bose-Hubbard eigenvalues, the low energy spectra from the two models agree well.

In the actual experiments, the number of $|a\rangle$ and $|b\rangle$ atoms are conserved, so $\sum_i S_{i,z}$ is preserved. If the system is homogeneous, we are allowed to drop the bias term h_z as it acts a global energy offset. However, if the system is inhomogeneous, the inhomogeneous bias term has a true physical effect and cannot be neglected anymore [85]. The effect of the inhomogeneity is more pronounced in the spin-1/2 models as all parameters scale with t^2/U , which can vary substantially in a tightly focused lattice beam.

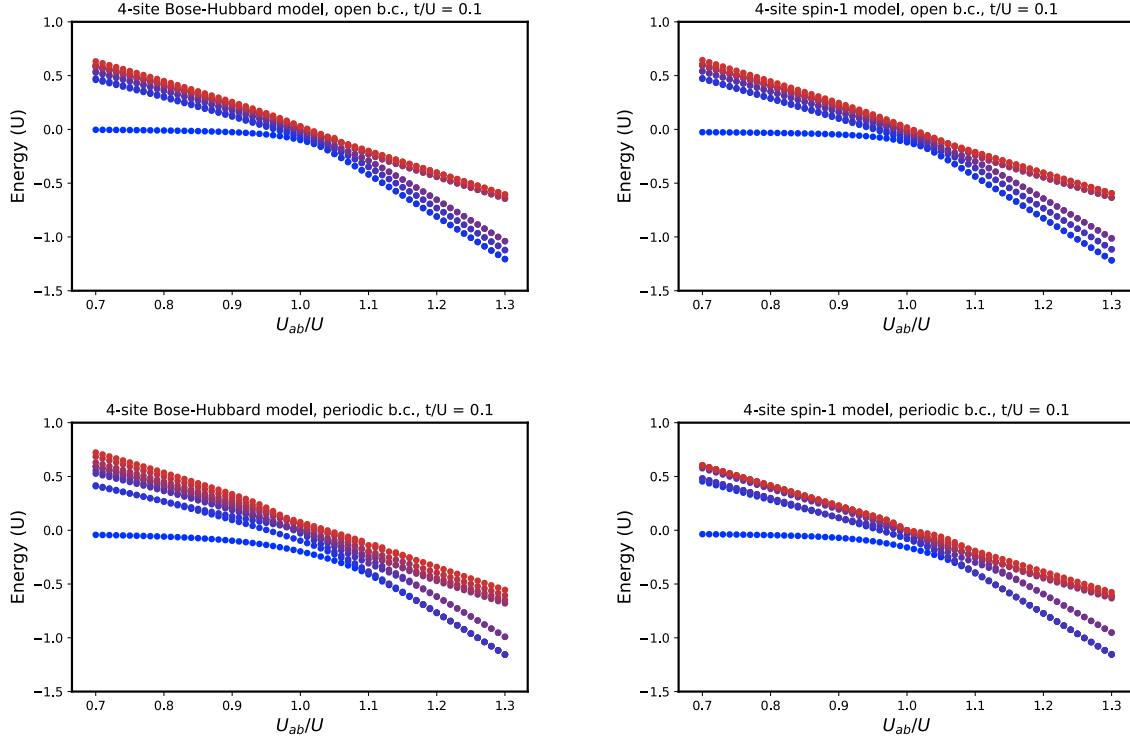


Figure 6-4: Comparison of energy spectrum between the Bose-Hubbard model (left column) and the effective spin-1 model (right column). The respective plots show the ten lowest eigenenergies for the given parameters and the boundary condition. The physical system considered is a chain of four sites, filled with four $|a\rangle$ and four $|b\rangle$ atoms, which is equivalent to the constraint $\sum_i S_{z,i} = 0$ for the spin model. The dimension of the Hilbert space for the Bose-Hubbard model is 1225 whereas it is 19 for the effective spin-1 model. We assume the Bose-Hubbard parameter of $t/U = 0.1$. The spin-1 model uses parameters from Eq. 6.4. Here we assume $\delta = 0$ but allow non-zero $d = U(1 - U_{ab}/U)$. We also consider two different boundary conditions (open for the top row and periodic for the bottom row). An additional energy offset expressed in Eq. 6.4 has been added to the Bose-Hubbard spectra. The spectra agree well, although there is more discrepancy between the higher energy spectra for the periodic boundary condition.

6.2 Magnetic phases in spin-1

The magnetic phase diagram of spin-1 differs from that of spin-1/2 in that it features a phase transition from a gapped to a gapless phase [22]. In fact, the phase transition is analogous to the superfluid-to-Mott insulator transition in the charge sector. When the anisotropy energy D is much higher than the exchange strength J , the ground state is a product state of $S_z = 0$. This state is called a spin Mott state. When the

exchange strength dominates over D , the energy can be lowered by increasing the fluctuations away from $S_z = 0$. This state, where the average value of S_z is still zero but its variance is nonzero, is called a spin superfluid state or a spin-1 xy ferromagnetic state, where we expect to see a quasi-long range order (characterized by an algebraic decay of the order parameter) in the transverse spin [23]. In both magnetic phases, there is no density transport but superfluid spin transport becomes possible within the spin superfluid phase. Such a motion is also known as counterflow superfluidity [21]. The spin Mott state is a useful initial state from which we can perform an adiabatic

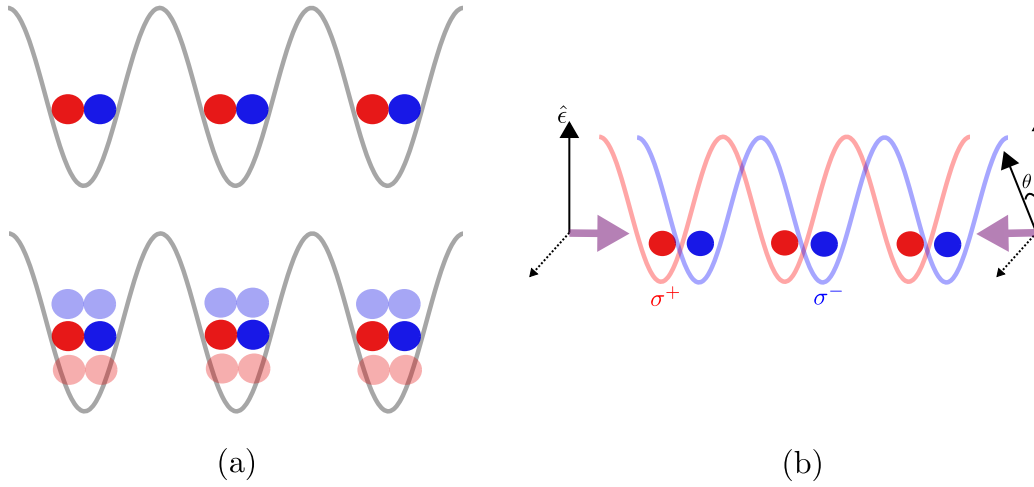


Figure 6-5: Magnetic phases of a ferromagnetic spin-1 chain. (a) Top: spin Mott state ($D/J \ll 1$). All sites are occupied by $|S_z = 0\rangle$, which is a perfect pairing between $|a\rangle$ and $|b\rangle$ atoms. Bottom: spin superfluid or xy-ferromagnetic state ($D/J < 1$). Quantum fluctuation develops around the \hat{S}_z eigenstate with $S_z = 0$. There is a definite phase coherence between the neighboring spins. (b) One can attempt an adiabatic passage from one state to the other by ramping the control parameter D/J . A state-dependent lattice can control the value of D by changing the wavefunction overlap between $|a\rangle$ and $|b\rangle$ and thereby changing U_{ab} . Note that such control is bounded by $|D| \leq |U_{aa} + U_{bb}|/2$.

passage toward the spin superfluid state because the spin Mott phase features an energy gap between the ground state and a band of excited states (Fig. 6-4) that reduces to zero as U_{ab}/U ramps from zero to one. Density matrix renormalization group (DMRG) calculation for an one-dimensional Bose-Hubbard chain shows that for $t/U = 0.1$, a phase transition is expected to occur around $U_{ab}/U = 0.956$ [23]. If our constituent atoms for the pseudo-spin-1 have opposite magnetic moments, we can

use a state-dependent optical lattice to control the separation between the two atoms and thereby control the spin-dependent interaction U_{ab} . To initialize into a spin Mott state, the two-component atom cloud is loaded into a state-dependent lattice with a large separation between the different hyperfine states so that a very large D/J is achieved while the lattices ramp up to their final value and the atom cloud enters into the Mott insulator phase. The spin Mott state is a state that features perfect pairing between two different hyperfine states, and in the extreme anisotropy limit ($U_{ab} \approx 0$) it can be regarded as a sum of two independent $\langle \hat{n} \rangle = 1$ Mott insulators. Another method to obtain the spin Mott state in a deep optical lattice is to start with a spin polarized Mott insulator with $|F = 1, m_F = 0\rangle^{\otimes 2}$ occupying the $\langle \hat{n} \rangle = 2$ Mott phase, and then use resonant spin-changing collisions that transform a $|F = 1, m_F = 0\rangle^{\otimes 2}$ pair into a pair of $|F = 1, m_F = -1\rangle$ and $|F = 1, m_F = 1\rangle$ [98]. However, this technique requires a low bias field and a careful tuning of microwave Stark shift, which is necessary for reducing the detuning of the oscillation³.

6.3 Spin-1/2 vs spin-1 realizations

Interaction and anisotropy

We note that the most important difference between the spin-1/2 model and the spin-1 model is the presence of a diagonal on-site interaction. In the spin-1/2 model, which is realized within a $\langle \hat{n} \rangle = 1$ Mott insulator phase, all on-site interactions are virtual. On the other hand, the anisotropy in the on-site interaction directly shows up as a magnetic anisotropy in the spin-1 model. Since on-site interactions are usually much greater than second-order tunneling amplitudes in the Mott-insulating phase, even a small anisotropy in the on-site interaction can easily become comparable to the exchange strength. Indeed, for ^{87}Rb , $U_{aa} \approx U_{bb} \approx U_{ab}$ within 1% [99], and the spin-1/2 model is mapped to the isotropic XXX model [100, 101]. However, in our

³The very same spin-dependent interaction responsible for the spin-changing collision is also responsible for this detuning. If we regard the spin-dependent interaction as a $\vec{S}_1 \cdot \vec{S}_2$ term, the transverse coupling $S_{x,1}S_{x,2} + S_{y,1}S_{y,2}$ gives rise to the Rabi frequency of the oscillation whereas $S_{z,1}S_{z,2}$ gives rise to the detuning.

experiment we make use of the 1% difference between the interactions to access a wide range of values for $|D/J|$ in the spin-1 model.

Observables

In the exploration of ordered magnetic phases, we are interested in measuring spin correlation functions such as the longitudinal correlation $\langle S_{z,i} S_{z,j} \rangle$ or the transverse correlation $\langle S_i^+ S_j^- \rangle$, which can be measured under a quantum gas microscope. To transform a longitudinal correlation measurement $S_{z,i} S_{z,j}$ into a transverse correlation measurement, one needs the transformation

$$S_z \rightarrow e^{-i\frac{\pi}{2} S_y} S_z e^{i\frac{\pi}{2} S_y} = S_x$$

For both spin-1/2 and spin-1 models, the unitary transformation is realized by a $\pi/2$ pulse that puts the atoms into a superposition of $|a\rangle$ and $|b\rangle$ states. In terms of the actual atom density being detected by imaging, the longitudinal correlation can be expressed as

$$\begin{aligned} \langle S_{z,i} S_{z,j} \rangle &= \frac{1}{4} \langle (\hat{n}_a - \hat{n}_b)_i (\hat{n}_a - \hat{n}_b)_j \rangle \\ &= \frac{1}{4} (\langle \hat{n}_{a,i} \hat{n}_{a,j} \rangle + \langle \hat{n}_{b,i} \hat{n}_{b,j} \rangle - \langle \hat{n}_{a,i} \hat{n}_{b,j} \rangle - \langle \hat{n}_{b,i} \hat{n}_{a,j} \rangle) \end{aligned}$$

We can make use of the identity

$$\begin{aligned} n^2 &= \langle (\hat{n}_a + \hat{n}_b)_i (\hat{n}_a + \hat{n}_b)_j \rangle \\ &= \langle \hat{n}_{a,i} \hat{n}_{a,j} \rangle + \langle \hat{n}_{b,i} \hat{n}_{b,j} \rangle + \langle \hat{n}_{a,i} \hat{n}_{b,j} \rangle + \langle \hat{n}_{b,i} \hat{n}_{a,j} \rangle \end{aligned}$$

where n is the local occupancy of the Mott insulator. To summarize, the longitudinal spin correlation can be connected to intra-spin density correlations $\langle \hat{n}_{a,i} \hat{n}_{a,j} \rangle$ and $\langle \hat{n}_{b,i} \hat{n}_{b,j} \rangle$ as follows:

$$\langle \hat{n}_{a,i} \hat{n}_{a,j} \rangle + \langle \hat{n}_{b,i} \hat{n}_{b,j} \rangle = 2\langle S_{z,i} S_{z,j} \rangle + \frac{n^2}{2} \quad (6.5)$$

On the other hand, we can also express the longitudinal spin correlation in terms of inter-spin density correlations $\langle \hat{n}_a \hat{n}_b \rangle$:

$$\langle \hat{n}_{a,i} \hat{n}_{b,j} \rangle + \langle \hat{n}_{b,i} \hat{n}_{a,j} \rangle = \frac{n^2}{2} - 2\langle S_{z,i} S_{z,j} \rangle$$

We provide an example calculation for the spin-1/2 model. If we assume a product state of the form $\bigotimes_i (\hat{a}^\dagger + e^{i\phi} \hat{b}^\dagger) / \sqrt{2} |0\rangle_i$, then Eq. 6.5 yields

$$\frac{1}{4} + \frac{1}{4} = 2\langle S_{z,i} S_{z,j} \rangle + \frac{1}{2}$$

which shows that the longitudinal spin correlation is zero, as expected. On the other hand, if we apply a $\pi/2$ rotation⁴ before measuring the density-density correlations, we obtain

$$\sin^4\left(\frac{\phi}{2}\right) + \cos^4\left(\frac{\phi}{2}\right) = 2\langle S_{z,i} S_{z,j} \rangle + \frac{1}{2}$$

If we average over the spin superfluid phase⁵ ϕ , then we obtain $\langle S_{x,i} S_{x,j} \rangle = \langle S_{y,i} S_{y,j} \rangle = 1/8$ and thus $\langle S_i^+ S_j^- \rangle = 1/4$, which is what we expect for a chain of spin-1/2 lying on the equator of the Bloch sphere and pointing in the same direction. The same result can be obtained by calculating the inter-spin density correlations.

The intra-spin density correlations can be measured directly under a microscope. In principle, one can obtain some information about the intra-spin density correlations without a microscope, by performing spatial quantum noise interferometry⁶ on the $|a\rangle$ atom cloud and the $|b\rangle$ atom cloud separately after time of flight [103, 104]. Another method to detect transverse spin correlation without high-resolution imaging is the measurement of an enhanced fluctuation in $n_a - n_b$ after applying a $\pi/2$ pulse. If

⁴Here we assume it is realized as a transformation $\exp(-i(\pi/2)S_y)$ in order to measure $\langle S_{x,i} S_{x,j} \rangle$. A rotation with S_x operator yields a different expression for the density correlations but the final result for the spin correlation does not change, which is consistent with the axial symmetry of the input state.

⁵One could also average over the rotation direction and obtain the same answer, which is independent of ϕ .

⁶To be specific, one obtains a *Fourier transform* of the density correlation, assuming translational invariance of the correlation $\langle \hat{n}_i \hat{n}_j \rangle = f(|i - j|)$. See Section 5.1.1 in Ref. [102].

there were no spin correlation, the fluctuation is described by shot noise, where the variance scales with the atom number, but if all parts of the cloud are correlated, one could see the variance scale with the square of the atom number. However, the measured signal can also be affected by parts of the atom cloud that are not mapped to the spin model under study, such as superfluid shells or the outer $\langle \hat{n} \rangle = 1$ Mott plateau in the case of the spin-1 model realization. The advantage of a quantum gas microscope is that one can take a direct look at the core of the cloud and obtain a measurement of the correlation operator without worrying about the surroundings of the core.

Finally, spin-1 has an observable that is not available to spin-1/2, and that is $\langle S_z^2 \rangle$, which amounts to a constant in spin-1/2. We make use of this observable heavily to infer the nature of the quantum state inside our spin-dependent lattice.

Chapter 7

Spin-1 physics with a two-component Bose gas

In the preceding chapters we have extensively explained how we realize a spin-1 model with two-component bosons in a deep three-dimensional optical lattice, where the bosons reside in a Mott insulating phase at the center of the trap. By making one axis of the optical lattice to be state-dependent, we can control the interaction between atoms in different hyperfine states. It is also possible to study spin-1 physics in a state-independent lattice by choosing an appropriate set of hyperfine states and making use of the small anisotropy in the spin-dependent interactions between atoms. In this chapter we summarize our experimental observations of spin-1 physics in a state-independent lattice and also in a state-dependent lattice.

7.1 Measurement of local spin pairing

A spin observable that we can measure reliably is the average spin pairing fraction f , or the fraction of $|S_z = 0\rangle = |a\rangle|b\rangle$ pairs among all pairs in the $\langle \hat{n} \rangle = 2$ Mott insulator. Formally f is equivalent to $1 - \langle S_z^2 \rangle$, where $\langle \dots \rangle$ represents averaging over all sites in a spin chain. Ideally, we would like to image and then count just the $|a\rangle|b\rangle$ pairs in the system. However, that requires many experimental prerequisites. First, the $|a\rangle|b\rangle$ pairs need to be transferred to a different state before imaging while the

$|a\rangle|a\rangle$ and $|b\rangle|b\rangle$ pairs remain in their original states and stay invisible to the imaging beam. Furthermore, the new state to which the $|a\rangle|b\rangle$ pairs are transferred needs to be collisionally stable so that the pairs do not decay after the transfer and before the imaging step. Finally, because not all the atoms in the optical lattice form pairs (see Fig. 5-2), we need to normalize the number of $|a\rangle|b\rangle$ pairs by the number of all pairs, and we would like to have a single experimental technique that can detect pairs in both state-sensitive and state-insensitive ways.

A relatively simple technique that can measure pairs is detection by an induced loss, where the induced loss can be either state-sensitive or state-insensitive. Then the number of pairs is estimated by taking the difference between the atom numbers before and after the induced loss. We induce losses in pairs by using narrow Feshbach resonances for $|F = 1, m_F = 1\rangle$ and $|F = 2, m_F = -2, -1, 0\rangle$ around a bias field of 9 G [105]. Around the resonances, the inelastic two-body collision rate is greatly enhanced. After such a collision, the initial pair of a $F = 1$ atom and a $F = 2$ atom exits as a pair of two $F = 1$ atoms that maintain the total magnetic quantum number $\sum m_F$, and the large hyperfine energy splitting ($h \times 6.8$ GHz) between the $F = 2$ and $F = 1$ manifolds is released as a kinetic energy, promptly kicking the pair out of the system¹.

In our experiment we make use of two Feshbach resonances: the $|1, 1\rangle|2, -2\rangle$ resonance at 9.0918 G and the $|1, 1\rangle|2, 0\rangle$ resonance at 9.0448 G. Both resonances have narrow widths (<2 mG) [105]. Our experiments are performed at a bias field of 8.916 G, and we provide an additional current to the bias coil from a high precision power supply (Keysight E3616A) to reach the Feshbach resonances. Before inducing the loss, we make sure that all the atoms are either in state $|1, -1\rangle$ or $|1, 1\rangle$, and then transfer $|1, -1\rangle$ to either $|2, -2\rangle$ or $|2, 0\rangle$ (Fig. 7-1). After the transfer, we turn on the additional current to reach the desired resonance and modulate the bias field around the resonances with a peak-to-valley amplitude of 10 mG, which is larger than the resonance widths. The modulation is done at the frequency of 300 Hz while the

¹Such a mechanism is called spin-exchange relaxation. To understand how a $F = 2$ state is flipped to a $F = 1$ state during the collision, consult Chapter 5 in Ref. [106].

atoms are held inside the optical lattices. After some hold time (<100 ms), all the pairs sensitive to the selected Feshbach resonance have been removed from the system and the bias field is reduced back to 8.916 G, at which any remaining $F = 2$ atom is transferred back to a $F = 1$ state. Then the remaining number of atoms is measured.

For the $|1, 1\rangle|2, -2\rangle$ resonance, which is used to selectively remove $|a\rangle|b\rangle$ pairs, all $|a\rangle|b\rangle$ are removed within 10 ms of hold time inside a deep three-dimensional optical lattice with lattice depth of 35 recoil energy in each direction. The $|a\rangle|a\rangle = |1, 1\rangle|1, 1\rangle$ and $|b\rangle|b\rangle = |2, -2\rangle|2, -2\rangle$ pairs remain intact as they are collisionally stable. On the other hand, for measuring all pairs, we have to apply a special trick as a Feshbach resonance itself is state-sensitive. We employ a continuous and diabatic Landau-Zener sweep between $|1, 1\rangle$ and $|2, 0\rangle$ so that all pairs ($|1, 1\rangle|1, 1\rangle$, $|2, 0\rangle|2, 0\rangle$, and $|1, 1\rangle|2, 0\rangle$) are admixed with a $|1, 1\rangle|2, 0\rangle$ pair wavefunction and gain a non-zero decay rate. The center of the diabatic sweep is set to the $|1, 1\rangle \rightarrow |2, 0\rangle$ resonance at 9.0448 G and the sweep scans a range of ± 140 kHz around the center with 1 kHz sweep rate in a triangular waveform². All pairs are seen to decay within 30 ms of hold time at the Feshbach resonance with this technique.

The average local spin pairing fraction is estimated from measurement of three numbers. One first measures the number of all atoms N_a before the induced losses. Then one measures N_p , the number of atoms left after removing $|a\rangle|b\rangle$ pairs, and N_d , the number of atoms left after removing all pairs. The pairing fraction can then be expressed as

$$f = \frac{N_a - N_p}{N_a - N_d}$$

For absorption imaging, we have to measure N_a , N_p , and N_d separately as the imaging process is destructive. Hence, a single datum of the pairing fraction measured this way requires three experimental cycles. Because f is a ratio of differences, number fluctuations measured in each of N_a , N_p , N_d can lead to a large error once propagated. So it is crucial that the atom number preparation is as stable as possible. A possible

²The optimal sweep range and sweep rate will in general depend on the Rabi frequency for the $|1, 1\rangle \rightarrow |2, 0\rangle$ transition, which is estimated to be $\mathcal{O}(10$ kHz) in our experiment.

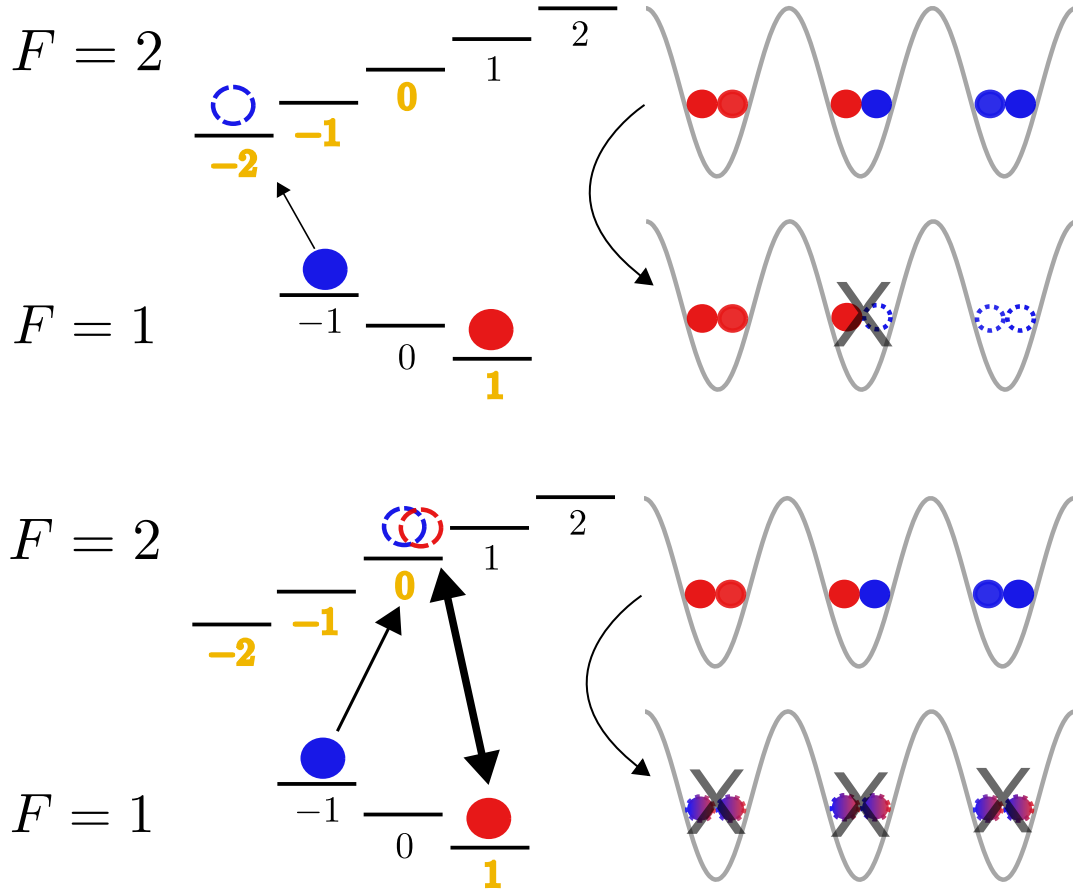


Figure 7-1: Measurement of local spin pairing by inducing spin-selective decay. We make use of narrow Feshbach resonances around $B = 9$ G [105]. Each resonance occurs for a pair of $|F = 1, m_F = -1\rangle$ state and one of $|F = 2, m_F = 0, -1, -2\rangle$ states (relevant states highlighted in yellow). (a) Measurement of $|a\rangle|b\rangle$ pairs by removal. First, $|b\rangle = |1, -1\rangle$ is mapped to $|2, -2\rangle$. Then the bias is tuned to the Feshbach resonance for the $|1, 1\rangle, |2, -2\rangle$ pair. (b) Measurement of all pairs by removal. First, $|b\rangle = |1, -1\rangle$ is mapped to $|2, 0\rangle$. Then the bias is tuned to the Feshbach resonance for the $|1, 1\rangle, |2, 0\rangle$ pair. With a continuous diabatic Landau-Zener sweep between $|1, 1\rangle$ and $|2, 0\rangle$, we ensure that every pair ($|a\rangle|a\rangle, |b\rangle|b\rangle, |a\rangle|b\rangle$) is admixed with a decaying component.

improvement would be to use a nondestructive in-trap imaging, such as polarization rotation imaging or phase shift imaging, that we can use to image the same sample consecutively and obtain (N_a, N_p, N_d) whose fluctuations are correlated. We actually tried both techniques, but a persistent problem was a small loss of atoms from the lattice after each exposure, as nondestructive imaging does impart recoil momenta to the atoms, and we could not ascertain any correlation between the measured $N_a - N_p$ and $N_p - N_d$. After several months of investment into the nondestructive imaging setup, we were forced to fall back on absorptive imaging. To obtain a decent estimate of f , we take three to four measurements each for N_a , N_p , and N_d . On a passing note, the most consistent data for pairing fraction was obtained when the lattice alignments were done with utmost precision, which suggests that the fidelity of the spin physics inside the lattice may be sensitive to the initial lattice loading conditions. If there were misalignments, it is possible that the density distribution prepared is not in equilibrium and does not match the expected distribution for a Mott insulator.

For convenience, in the following discussion we use a variable named spin alignment $A = S(S + 1) - 3\langle S_z^2 \rangle$ in lieu of f . The variable is equivalent to $3f - 1$. By definition, spin alignment is zero when the spin system is at infinite temperature ($f = 1/3$).

7.2 Observation of exchange in spin-1 model

In this section we summarize our study of non-equilibrium dynamics in the spin-1 model, where we observe exchange-induced relaxations in the spin alignment after a quench in the anisotropy-to-exchange ratio D/J (with J changing from zero to a non-zero value). An unexpected result is that the relaxation is most pronounced when the anisotropy and the exchange are on an almost equal footing ($|D/J| \approx 2$). We note that this experiment is performed in a state-independent lattice (all lattice beams have wavelength of 1064 nm), and hence D/J is changed not by changing D but primarily by changing J through a variation of the lattice depth. Although Eq. 6.4 predicts a nonzero exchange anisotropy and a correction to the single-ion anisotropy

in general, because both d/U and $(t/U)^2$ are less than 1% in this experiment, such corrections can be ignored. The main result has been published in Ref. [24], a copy of which is provided in Appendix B. In the following we also provide more details for the experimental conditions not mentioned in the publication.

7.2.1 Idea behind the experiment

The original idea behind the experiment was to find a signature of spin exchange in our $\langle \hat{n} \rangle = 2$ Mott insulator by preparing a non-equilibrium distribution of $|a\rangle|b\rangle = |S_z = 0\rangle$ and monitoring its relaxation toward the equilibrium. If the dynamics inside the Mott insulator is governed by kinetic exchange, then we expect the relaxation rate to scale with $|J| = 4t^2/U$ as a function of lattice depth along the spin chain direction. Because J scales exponentially with lattice depth (Fig. 7-2), we expected a monotonic change in the relaxation rate as a function of lattice depth and hoped to see a constant coefficient after normalizing the different relaxation rates by J . However, as it is explained later, such a conclusion was erroneous because we did not consider the effect of the single-ion anisotropy term in our model at all³.

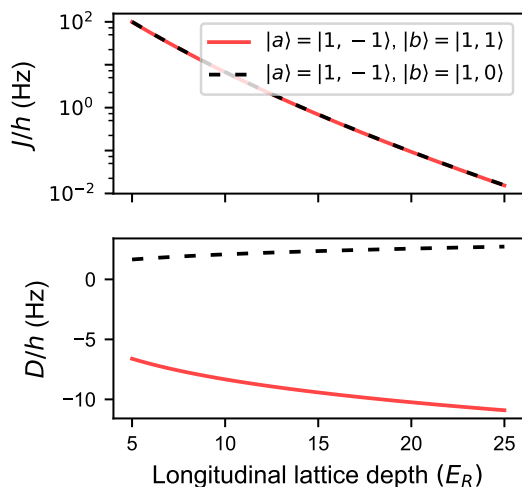


Figure 7-2: Variation of $-J$ and D with respect to the longitudinal lattice depth. The transverse lattices are set to $35 E_R$. The lattice laser wavelength is 1064 nm.

³Julius de Hond, our postdoctoral associate, noted first that the SIA term might be important after performing numerical simulations.

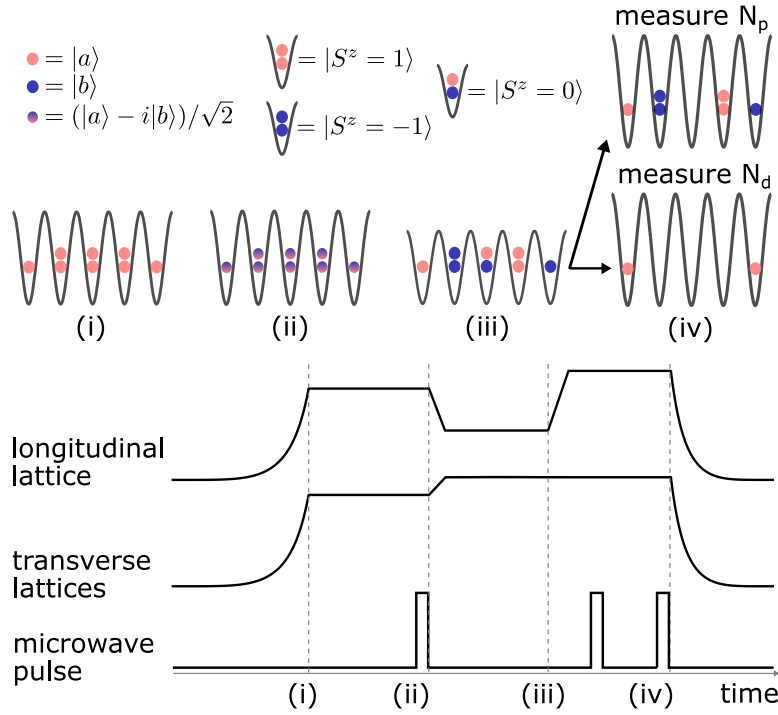


Figure 7-3: Experimental sequence for the measurement of spin alignment and doublon fractions. (i) The lattices are ramped up to initialize a single-component Mott insulator with a maximal site occupancy of two. (ii) Microwave pulses prepare a superposition of two hyperfine states $(|a\rangle - i|b\rangle)/\sqrt{2}$. Ramping down the longitudinal lattice initiates spin exchange dynamics. (iii) Ramping up the lattices stops the exchange dynamics. Microwave pulses transfer the two components to a pair of states with a Feshbach resonance. (iv) Either $|ab\rangle$ doublons or all doublons are removed with the help of Feshbach-enhanced inelastic losses. Remaining atoms are transferred back to the $F = 1$ hyperfine states and are counted via absorption imaging to measure N_p or N_d .

7.2.2 Experimental sequence

The experimental sequence is described in Fig. 7-3. A spin-polarized Mott insulator with all the atoms in the $|a\rangle$ state receives a $\pi/2$ pulse that puts $|a\rangle$ into a superposition with $|b\rangle$. Then the initial average fraction of $|a\rangle|b\rangle$ pairs in the $\langle \hat{n} \rangle = 2$ Mott insulator is 0.5, and hence the initial spin alignment is $3(0.5) - 1 = 0.5$. During this state preparation, all lattices are deep and hence J is negligible. We have two possible choices⁴ for $|a\rangle$ and $|b\rangle$. The first choice realizes a negative value of D , which is $|a\rangle = |1, -1\rangle$ and $|b\rangle = |1, 1\rangle$. The second choice realizes a positive value of D , which is $|a\rangle = |1, -1\rangle$ and $|b\rangle = |1, 0\rangle$. The scattering lengths for different combinations of the hyperfine states can be found in Appendix B. For both choices, the state preparation begins with a diabatic Landau-Zener sweep of $|1, -1\rangle$ to $|2, 0\rangle$ that transfers roughly 50% of the population into the latter state. Then the $|2, 0\rangle$ state can be adiabatically transferred to either $|1, 1\rangle$ or $|1, 0\rangle$. Because $|2, 0\rangle$ can undergo spin-exchange relaxation when partnered with a $F = 1$ atom, the second and adiabatic sweep is performed quickly after the first and diabatic sweep. The typical two-body decay rate κ for $|2, 1\rangle$ is $\mathcal{O}(10^{-13} \text{ cm}^3/\text{s})$ [107], and we assume that $|2, 0\rangle$ decays at a similar rate. For a peak on-site density of $1.4 \times 10^{14}/\text{cm}^3$ in a three-dimensional lattice with depth $30 E_{R,1064\text{nm}}$, we expect roughly a 5% loss during a 5 ms sweep⁵.

Once the initial state preparation is finished, the lattice depth is quickly reduced to a lower value along the longitudinal direction, so that the Mott insulator can be regarded as a two-dimensional array of isolated one-dimensional spin chains. This quench step happens over several milliseconds, so that it is highly diabatic with respect to the exchange J but adiabatic with respect to the on-site interaction energy U so that we do not create quasiparticle-quasihole excitations from the Mott insulator ground state. A reverse quench to a deep three-dimensional lattice is performed after a variable hold time in the lowered longitudinal lattice, in order to carry out the

⁴Note that we previously referred to $|1, -1\rangle$ as $|b\rangle$, e.g. in Fig. 7-1. For convenience, we now refer to it as $|a\rangle$.

⁵The main limitation was the relatively small Rabi frequency for the $|2, 0\rangle \rightarrow |1, 1\rangle$ transition. The Landau-Zener sweep for $|2, 0\rangle \rightarrow |1, 0\rangle$ transition can be replaced by a short Rabi π pulse due to its relative insensitivity to bias fluctuation.

Feshbach-enhanced loss measurement of pairs.

7.2.3 Result and analysis

To our surprise, we discovered that the spin alignment changed noticeably faster not at the lowest lattice depth at which we can hold onto the Mott insulator, but at some intermediate lattice depth (Fig. 7-4). Furthermore, the sign of the change in the spin alignment follows the sign⁶ of $D/|J|$. The latter point can be intuitively understood by considering that spins prefer to be in $|S_z = 0\rangle$ (higher spin alignment) when $D > 0$ and $|S_z = \pm 1\rangle$ (lower spin alignment) when $D < 0$. If there were any source of external heating rate that can disorder the spin chain, the spin alignment would reduce from the initial value of 0.5 to zero and produce a signal that looks similar to the $D < 0$ result. Thus, the observation of an increase in the spin alignment for $D > 0$ is strong evidence of exchange dynamics within the spin chain.

The intermediate lattice depths at which the spin alignment is seen to have extremal changes correspond to $|D/J| \approx 2$. This can be qualitatively understood by considering a two-site model. In a two-site model, the only states of the Hilbert space that can contribute to a change in the spin alignment are $|S_{z,1}, S_{z,2}\rangle = |0, 0\rangle$ and $(|1, -1\rangle + |-1, 1\rangle)/\sqrt{2}$. Thus, the dynamics is reduced to that of a two-level system. If we picture the dynamics of the two-level system on a Bloch sphere (Fig. 7-5), with $|0, 0\rangle$ acting as the north pole, we see that the Hamiltonian is represented by a fictitious field of strength $-(J+2D)$ on the z-axis and $-2\sqrt{2}J$ on the x-axis. Thus, the total fictitious field has a strength of $\sqrt{8J^2 + (J+2D)^2} = \sqrt{9J^2 + 4DJ + 4D^2}$ and its axis is oriented away from the north pole by an angle θ where $\tan \theta = 2\sqrt{2}J/(J+2D)$. Our initial state, when projected to the reduced Hilbert space, corresponds to

$$\frac{\sqrt{6}}{4} \left(\sqrt{\frac{2}{3}}|0, 0\rangle + \sqrt{\frac{1}{3}} \frac{|1, -1\rangle + |-1, 1\rangle}{\sqrt{2}} \right)$$

On the Bloch sphere, this projected state precesses around the axis of the total fictitious field, and thus the total fraction in $|0, 0\rangle$ oscillates with a peak-to-valley

⁶Note $J = 4t^2/U$ in Ref. [24] as the exchange interaction is defined as $-J\vec{S}_i \cdot \vec{S}_j$ there.

amplitude of

$$2 \left(\frac{(D/J)}{9 + 4(D/J) + 4(D/J)^2} \right)$$

This amplitude is zero when $D/J = 0$ and has maximal values at $D/J = \pm 3/2$. At zero anisotropy, the initial state is simply a rotated version of the ferromagnetic state where all spins point up ($S_z = 1$) and hence it is an eigenstate of the isotropic spin-1 model, meaning that there is no temporal change in the spin alignment. Indeed, this situation corresponds to the projected initial state being parallel to the total fictitious field on the Bloch sphere. On the other hand, if the anisotropy is extreme ($|D/J| \gg 1$), the total fictitious field on the Bloch sphere points along the z-axis, and hence the projection onto the north pole (population in $|0, 0\rangle$) does not change. Physically, a large anisotropy makes spin exchange off-resonant and prevents $|1, -1\rangle$ from converting into $|0, 0\rangle$ and vice versa. So it is natural to conclude that an extremal change in the spin alignment occurs when $|D/J|$ is somewhere between zero and a large value. Without anisotropy, no dynamics can be induced by a simple rotation of the initially spin-polarized state, but the anisotropy has to be small enough to allow spin exchange to occur. As you increase the number of sites in the spin chain, we expect a variety of precession frequencies arising from Hilbert subspaces with different total S_z values, and hence a single-frequency oscillation in the two-site model changes into a relaxation.

7.2.4 Possible effects of magnetic gradient

A source of perturbations that can couple to the spin dynamics is the residual magnetic gradient, whose strength we denote as Δ . It creates a magnetic energy offset between neighboring sites. If the gradient is strong enough, it can reverse the sign of the change in the spin alignment, so that the spin alignment is reduced for $D > 0$ and enhanced for $D < 0$. This can be also understood by considering the two-site model (Fig. 7-6). In the presence of a gradient, the Hilbert subspace that is responsible for a change in the spin alignment consists of three states: $|0, 0\rangle$, $|1, -1\rangle$, and $|-1, 1\rangle$.

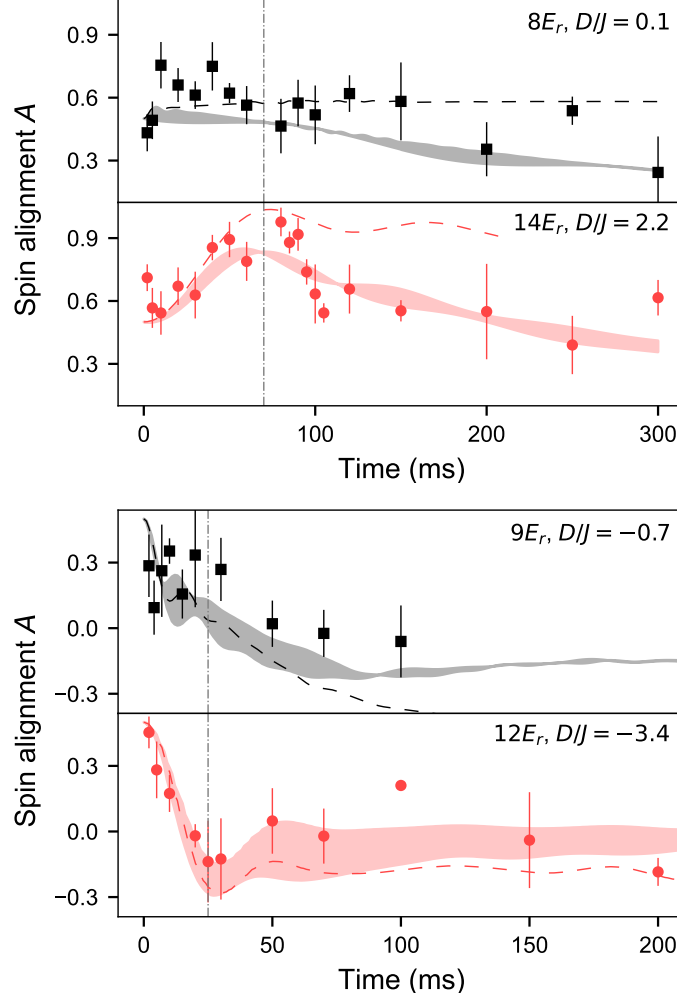


Figure 7-4: Coherent dynamics of the spin alignment A after a quench in D/J . Varying the hold time at characteristic lattice depths for both positive and negative values of D/J (top and bottom pairs of panels, respectively) reveals that strong transients in A only occur at intermediate lattice depth for which D and J are comparable. Dashed lines are the results of the MPS-TEBD simulation. The shaded regions denote the MPS-TEBD results with $\pm 0.5 E_R$ uncertainty in the lattice depths, and include exponential decay towards a thermal spin state with $A = 0$ with empirical $1/e$ times of 350 ms ($D > 0$) and 175 ms ($D < 0$), the ratio of which reflects the relative sensitivity to ambient magnetic field fluctuations of the pairs.

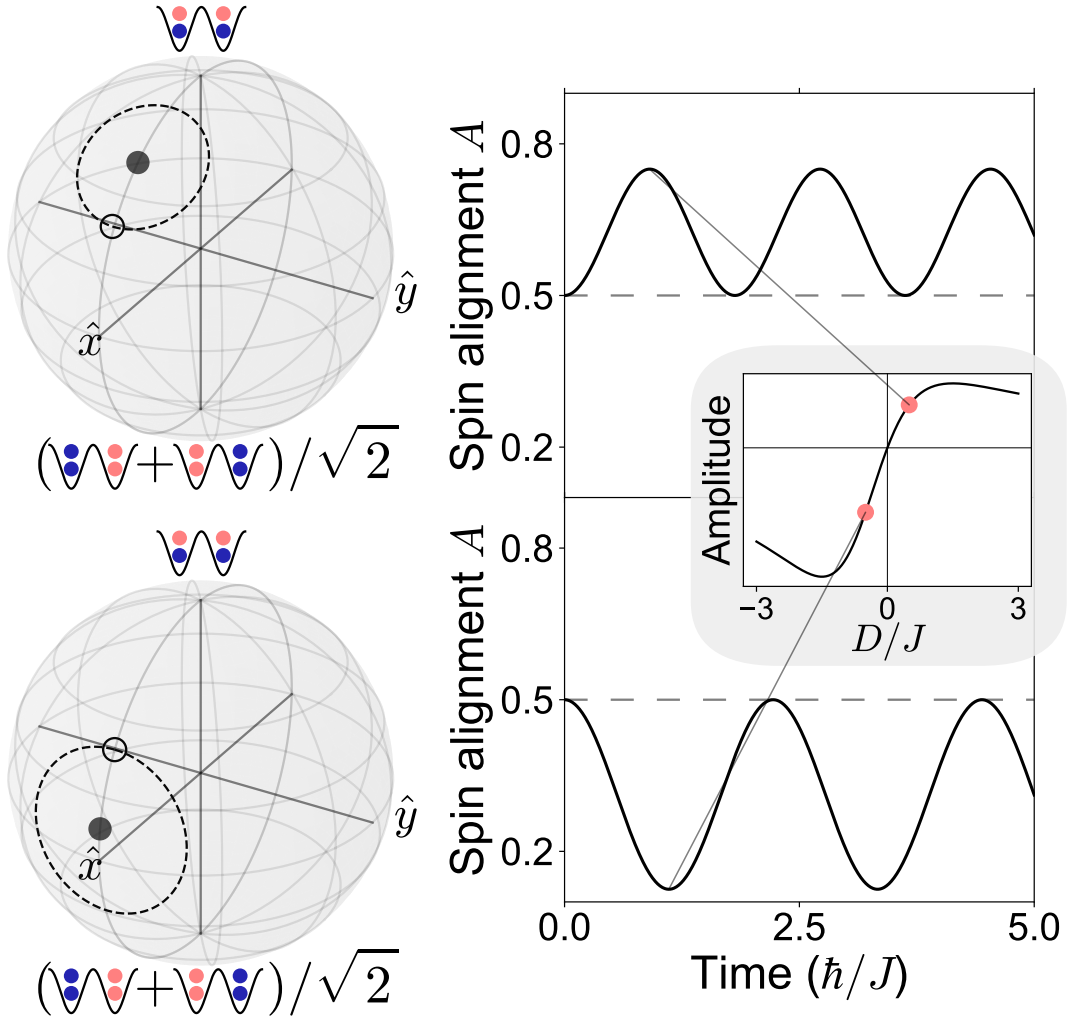
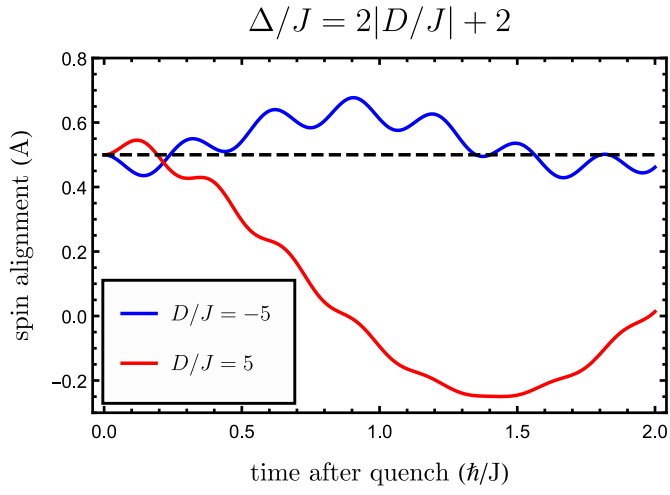
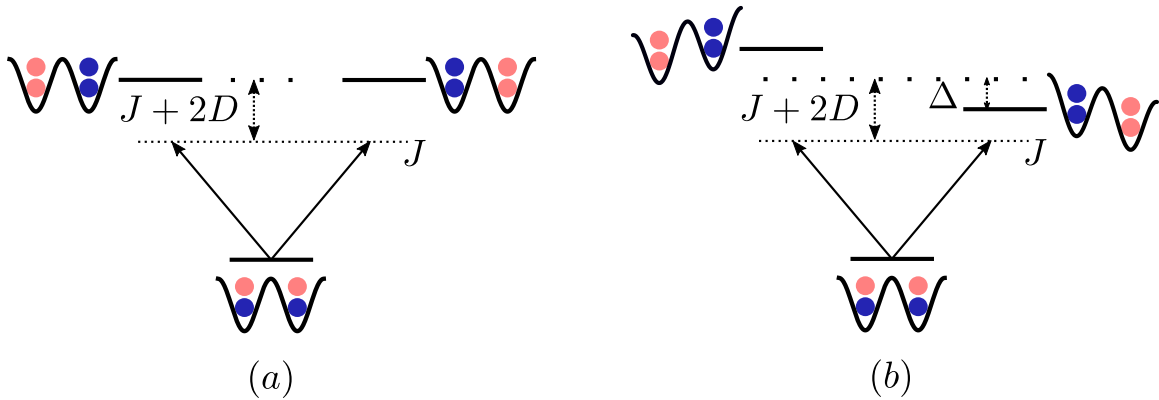


Figure 7-5: Coherent spin oscillations in a two-site model. While the full basis contains nine states, the oscillations in the spin alignment A involve only a 2×2 block of the Hamiltonian. This allows us to illustrate the dynamics on Bloch spheres (left), where the initial state is represented by the open circle. If $J = 0$ the effective magnetic field points along \hat{z} , and the purely azimuthal precession will not change A . If $J > 0$ the effective magnetic field is tilted, resulting in a precession along the dashed circle which is observed as an oscillation in A (right). The frequency of the oscillation, in units of J/\hbar , is given by $\Omega = \sqrt{9 + 4D/J + 4(D/J)^2}$, and its peak-to-peak amplitude is $6(D/J) / [9 + 4D/J + 4(D/J)^2]$ (see inset). This shows that the direction of oscillation depends on the sign of D/J (compare top and bottom rows, where $D/J = 0.5$ and -0.5 , respectively). Note that while the initial value of A for this subspace is 1, the contribution of other states sets the initial A of the whole system to $1/2$.

At zero gradient, $|1, -1\rangle$ and $|-1, 1\rangle$ are degenerate and the transitions from $|0, 0\rangle$ to those states are equally detuned. However, if $\Delta = \pm(J + 2D)$, we obtain a resonant transition between $|0, 0\rangle$ and either $|1, -1\rangle$ or $|-1, 1\rangle$. Similarly to the zero gradient case, we can restrict ourselves to a two-level system to obtain a better analysis. In this case the Bloch sphere corresponding to the two-level system consists of $|0, 0\rangle$ on the north pole and either $|1, -1\rangle$ or $|-1, 1\rangle$ on the south pole. Without loss of generality, we assume $|1, -1\rangle$ is on the south pole. On the Bloch sphere, the fictitious field is $(B_x, B_z) = (-2J, \pm\Delta - J - 2D)$. The orientation (v_x, v_z) of the projection of the initial state onto the Bloch sphere is $(4/5, 3/5)$. If $(\pm\Delta - J - 2D) = -3/2J$, then the fictitious field becomes anti-parallel to the projection of the initial state. So if we set the gradient to $\pm\Delta = 2D - J/2$, we expect no dynamics other than a highly detuned oscillation between $|0, 0\rangle$ and the leftover state $|-1, 1\rangle$. By perturbing the gradient value around this point, we can tilt the axis of the fictitious field away from the initial state orientation and guide its axis either closer to or farther away from the north pole, so that one may expect, for example, an increase in the spin alignment for $D < 0$ if the gradient is strong enough. Indeed, numerical simulations show that for longer chains, $\Delta/J \approx 2|D/J| + 2$ provides a noticeable reversal of the spin alignment change. In our experiment, the value $2|D| + 2J$ for $|D/J| = 2$ is $2\pi \times 6$ Hz for $D > 0$ and $2\pi \times 36$ Hz for $D < 0$. Such gradient strengths correspond to 0.16 G/cm for $D > 0$ and 0.5 G/cm for $D < 0$, given the experimental conditions. We make sure that our residual gradient level is far below such numbers after shimming the fields and checking the Ramsey coherence lifetime of a field-sensitive superposition state (Fig. 2-4) and thus we conclude that our main observation is not affected by the residual magnetic gradient.

7.2.5 Conclusion

In conclusion, our observation of the correspondence of the sign of the spin alignment change to the sign of the anisotropy D and of an enhanced change in the spin alignment near $2J \approx |D|$ strongly suggests that we have observed a coherent spin-1 dynamics within our $\langle \hat{n} \rangle = 2$ Mott insulator. Because of the smallness of the exchange



(c)

Figure 7-6: Effect of magnetic gradient on a two-site spin-1 model. (a) No gradient. (b) Finite gradient. If $\Delta \approx J + 2D$, one can see a large change in the $|0, 0\rangle$ state population even in the presence of a large anisotropy. (c) Simulation of spin alignment evolution in a two-site spin-1 model augmented by a magnetic gradient $-\Delta \sum_i i S_{z,i}$. Here $\Delta/J = 2|D/J| + 2$. The initial state is $\prod_{i=1}^2 \left(\frac{|a\rangle_i + |b\rangle_i}{\sqrt{2}} \right)^{\otimes 2}$. The dynamics with negative (positive) anisotropy now produces an upward (downward) trend in the spin alignment change, which is opposite to the trend shown in the zero gradient case.

strength ($< 2\pi \times 10$ Hz in our experiment), one expects a very low spin entropy in the system as a prerequisite for studying the physics of coherent exchange, and our results show that the spin entropy stays low for at least an exchange period. Our data analysis also demonstrated the usefulness of simple models such as effective two-level systems for studying coherent spin dynamics. On a broader outlook, simulation of non-equilibrium spin-1 physics with arbitrarily prepared initial states using ultra-cold atoms may be quite useful for providing a clean study of complicated effects observed in magnetic materials, such as the renormalization of interactions between spin excitations (magnons) at high densities in a spin-1 ferromagnet [108].

7.3 Investigation of the spin Mott phase

In this section we summarize our study of the ground state properties of the spin-1 model. Primarily, we focus on the spin Mott state ($D/J \gg 1$) and we rely on a state-dependent lattice along the bias field direction to tune D/J over a wide range. In the limit of extremely high D/J , the spin Mott can be thought of as an overlay of two independent spin-polarized $\langle \hat{n} \rangle = 1$ Mott insulators. While this is no longer true for a finite interaction between different spins ($U_{ab} > 0$), the analogy to a regular charge Mott insulator is useful, as we show in the following discussions. However, the spin Mott state is more than just an analogue to the density Mott state, as it allows an adiabatic passage toward the fragile spin superfluid state (Fig. 7-7). Since the the spin superfluid phase is characterized by a very low energy scale, the adiabatic ramp is also a form of adiabatic cooling within the Mott insulating state. We have characterized the properties of the spin Mott phase in various ways.

7.3.1 Adiabatic passage with a state-dependent lattice

The primary role of the spin Mott state is to use its high energy gap to prevent the spin entropy from increasing while performing an adiabatic ramp to another spinful state. Within the deep spin Mott phase, spin entropy can be measured by counting how many sites do not have a pairing between two opposite hyperfine states. However,

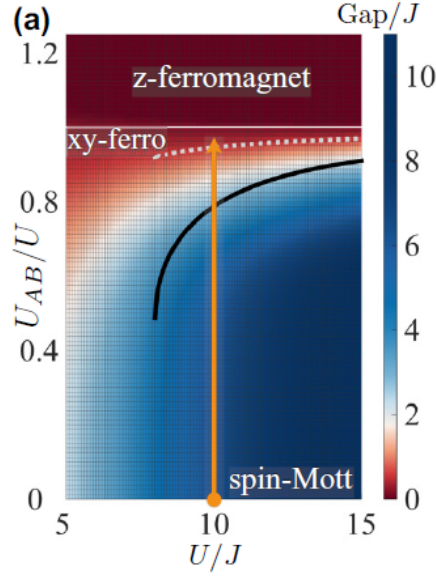


Figure 7-7: Phase diagram of the spin model. Figure adapted from Fig. 1 in Ref. [23]. The white dashed line is the phase boundary between the spin Mott phase and the spin superfluid phase calculated by 1D DMRG.

one can also demonstrate the effect of spin entropy in a more macroscopic sense, by measuring the reduction of the condensate fraction of a BEC in a spin superposition state which then undergoes decoherence. We present both approaches and we first expound on the condensate fraction measurement experiment.

Spin entropy and BEC condensate fraction

A BEC in a spin superposition state without any dephasing can be considered a spin-polarized cloud. However, after dephasing, the BEC turns into a mixture of two smaller BECs, and the entropy of mixing leads to a decrease in the overall condensate fraction. To probe this effect, a spin polarized cloud is initialized into a $\langle \hat{n} \rangle = 1$ Mott insulator. To create a superposition state with a long coherence time, we used the clock state pair $|1, -1\rangle + |2, 1\rangle$ around the bias field of 3.23 G, where the state becomes first-order insensitive to ambient field fluctuations. The superposition state was created by a $\pi/2$ two-photon pulse. On the other hand, other superposition states such as $|1, 1\rangle + |2, -1\rangle$ or $|1, -1\rangle + |1, 1\rangle$ are sensitive to ambient field fluctuations and dephase rather quickly. By ramping down the Mott insulator back to BEC and

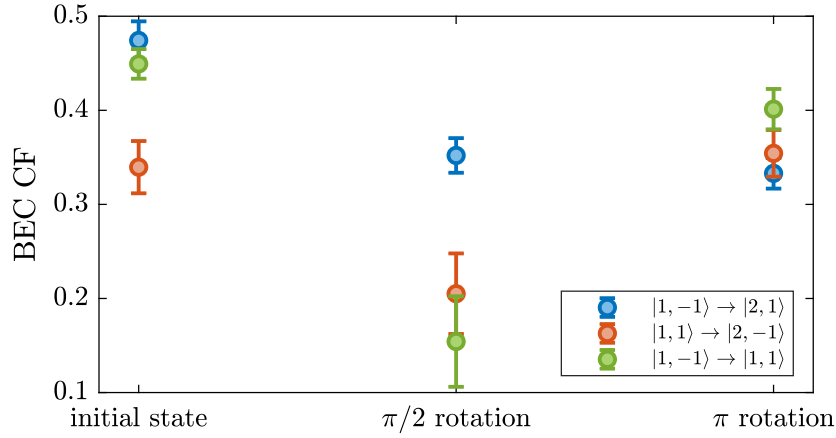


Figure 7-8: Demonstration of an increase in condensate fraction due to the spin entropy from spin dephasing. A spin polarized cloud of $|1, -1\rangle$ (or $|1, 1\rangle$) is prepared into a $\langle \hat{n} \rangle = 1$ Mott insulator held in a 3D $25 E_{R,1064 \text{ nm}}$ lattice (first column). The condensate fraction is measured after ramping down the lattice and transforming the Mott insulator back to BEC. After a $\pi/2$ pulse, each atom is put into a spin superposition state (second column). The pair $|1, -1\rangle + |2, 1\rangle$ is insensitive to field fluctuations in first order around bias field of 3.23G, while other combinations dephase quickly under field fluctuations. The field sensitive superposition states result in a visible drop in the retrieved condensate fraction. On the other hand, if we complete the spin flip with a π pulse (third column) before the dephasing can take place, the original condensate fraction is largely recovered.

measuring the retrieved condensate fraction, we noticed a visible reduction in the condensate fraction in the case of field-sensitive superposition states, whereas the field-insensitive superposition state suffers less reduction (Fig. 7-8). The reason for the rather low initial values of the condensate fraction is due to the very low atom number required to reduce $\langle \hat{n} \rangle$ and the limited time over which the lattices can be ramped down smoothly. Because of spin exchange relaxation between $F = 1$ and $F = 2$ states, as soon as the Mott insulator melts and the atoms can interact with each other, the atom cloud undergoes a fast decay. Hence, the Mott insulator had to be ramped down as quickly as possible while allowing a few tunneling times for phase coherence to build up between the atoms [109].

The condensate fraction measurement demonstrates that without a state-dependent potential, atoms in different hyperfine states are free to mix around, resulting in a large spin entropy (lack of spin ordering). In the next subsection, we demonstrate how the spin entropy of the two-component atom cloud can stay minimized by loading the cloud into a state-dependent potential.

Spin entropy and state-dependent lattice control

We use a state-dependent lattice at the wavelength of 810 nm, which provides a vector-to-scalar ratio $2R = \alpha_V/\alpha_S = 1/4$ (see Eq. 3.3 and Sec. 4.2.1). The 810 nm lattice beam is generated by a continuous-wave, narrow linewidth (<50 kHz) Ti:sapphire laser (M Squared SolsTiS 5W). The hyperfine states used are $|F = 1, m_F = -1\rangle$ and $|F = 1, m_F = 1\rangle$. The experimental sequence is described in Fig. 7-9. If we were to ramp an atom cloud of spin mixture directly into a deep optical lattice without any state-dependent potential, the atoms will in general require some density redistribution (for the formation of a Mott insulator) and also spin redistribution (for the formation of a spin superfluid if the inherent D is smaller than J) in order to stay in the ground state of the system. The presence of a large fictitious magnetic gradient from the state-dependent lattice ensures that the atoms find it energetically favorable to organize themselves in a simple spin density distribution, where different hyperfine states are interleaved with each other [step (ii) in Fig. 7-9]. Within the spin

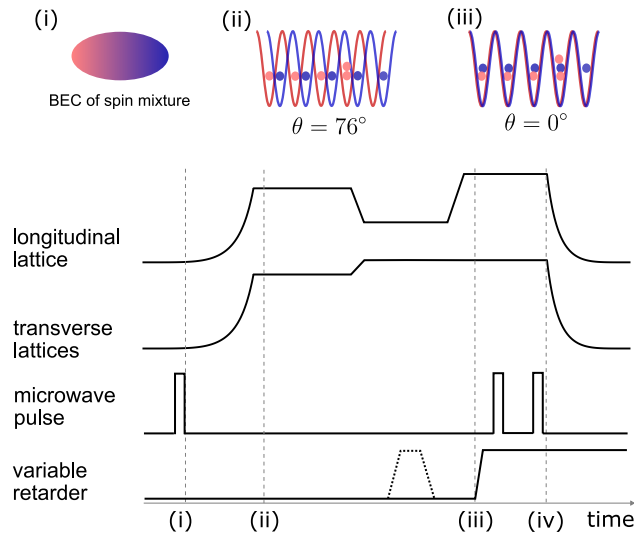


Figure 7-9: Experimental sequence for the measurement of spin alignment after a ramp into a state-dependent lattice. The longitudinal lattice is the state-dependent lattice. (i) Before the lattice ramp, an initially spin-polarized atom cloud is transformed into a superposition of two different hyperfine states with opposite magnetic moments. (ii) The atom cloud is ramped into a deep three-dimensional optical lattice, with a non-zero polarization gradient along the state-dependent lattice direction. The wavefunction overlap between the different hyperfine states is reduced. After the ramp the variable retarder can further change the polarization gradient or stay at the present setting. (iii) After a variable hold time, the variable retarder ramps the polarization gradient to zero and the initially separated states are merged. (iv) Spin pairing fraction measurement is performed as described in Sec. 7.1.

Mott phase, the spin entropy of the system can be inferred from the deviation of the spin pairing fraction from the ideal value of one⁷.

The experimental data is shown in Fig. 7-10(a), where we initialize a spin Mott in a very deep optical lattice with depths $35 E_{R,1064\text{nm}}$ in the transverse directions and $15 E_{R,810\text{nm}}$ in the longitudinal direction, along which we have $U/t = 58$. After the initialization we adiabatically ramp down the anisotropy to a final value (parametrized by U_{ab}/U). The ramp happens over many tens of milliseconds, and we compensate the lattice intensity so that the state-dependent lattice stays constant while the contrast of the polarization gradient is reduced by the variable retarder. We see that we maintain a very high pairing fraction characteristic of the spin Mott phase until $U_{ab}/U = 0.85$. According to a full numerical simulation of the one-dimensional Bose-Hubbard model [Fig. 7-10(b)], we expect to maintain a high pairing fraction until we get very close to the isotropy point $U_{ab}/U = 1$ in this deep lattice, but we start to lose the pairing fraction early on. If the ramp were an adiabatic process, we expect to recover the loss in the pairing fraction when we ramp back to the high anisotropy region (low U_{ab}/U). However, we have seen no sign of such recovery, suggesting that the loss in the pairing fraction is a real increase in spin entropy within the state-dependent lattice. Some experimental concerns so far are

1. A large change in the overall confinement during the lattice-depth-compensated polarization gradient ramp due to the tight Gaussian envelope of the 810 nm.
2. Highly non-equilibrium density loading of the Mott insulator. The mismatch between the estimated $\langle \hat{n} \rangle = 2$ Mott insulator size and the actual atom number is even bigger for the 810 nm lattice than it was for the 1064 nm lattice (Fig. 5-3).
3. Light-scattering limited lifetime. We expect that every atom will have scattered a photon on average after a 1 s hold time in a lin-90°-lin lattice of 810 nm [see

⁷For a finite exchange strength, the ground state spin alignment will be slightly less than one.

Fig. 3-2].

4. Noise from the liquid crystal (LC) variable retarder. The LC device can impart both lattice intensity noise and lattice phase noise. The lattice phase noise issue can be solved by placing the retarder before the atom cloud (see Sec. 4.2.1).

Although the current state-dependent lattice in use is not fully adequate, it does provide some degree of protection from an increase in spin entropy. If we load the spin mixture atom cloud directly into the state-dependent lattice with a final U_{ab}/U value, without any spin Mott initialization at a lower U_{ab}/U , then we see that it always returns a reduced spin pairing fraction [red data points in Fig. 7-10(a)]. When we load the cloud at the isotropy point $U_{ab}/U = 1$, we expect to see a pairing fraction of $1/3$, which is the value consistent with a uniformly random spin ordering inside the $\langle \hat{n} \rangle = 2$ Mott insulator. However, we see deviations from that value, and the deviation depends on the time between the end time of the lattice ramp and the end time of the mixture creation, suggesting that some complicated spin density dynamics is triggered within the BEC after the creation of the mixture⁸.

In conclusion, we have demonstrated a basic feature of the spin Mott state, which is the protection from spin entropy (maintenance of a high spin pairing fraction) at high anisotropy values (low U_{ab}/U values). While the goal is to use the spin Mott state as a stepping stone to reach the spin superfluid state, more work needs to be done to improve the robustness of the spin Mott state where the anisotropy strength is relatively weak ($U_{ab}/U \approx 0.9$). Based on the listed experimental concerns, it is possible that the background Mott insulating state needs to be carefully examined to see if the $\langle \hat{n} \rangle = 2$ phase within the cloud is in equilibrium.

⁸In particular, because $|F = 1, m_F = -1\rangle$ and $|F = 1, m_F = 1\rangle$ are very close to the miscibility/immiscibility boundary, and the effective potential seen by each hyperfine state is very small. Thus the Thomas-Fermi approximation no longer holds for individual spin densities; it only holds for the total density [110].

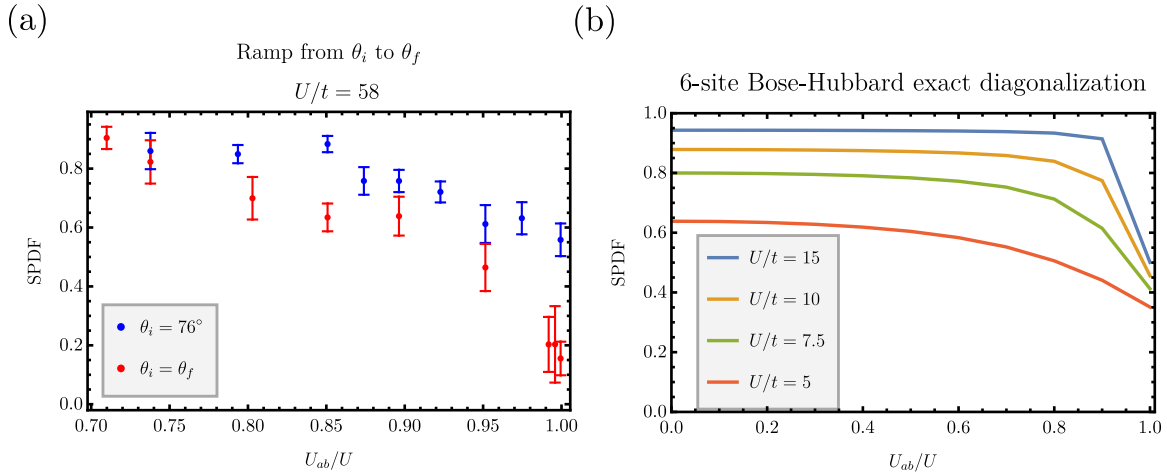


Figure 7-10: Measurement of spin alignment as a function of $U_{ab}/U = 1 - D/U$. (a) Blue: the atom cloud is loaded into a lin- θ -lin polarization gradient with $\theta = 76^\circ$ and then θ is reduced to a final value. Reduction in θ is equivalent to an increase in U_{ab}/U . [see the curve for $R \cos \theta_k = 1/8$ in Fig. 4-2(b)]. The spin pairing fraction stays high until $U_{ab}/U = 0.85$. Red: the atom cloud is loaded directly into a state-dependent lattice with the final value of θ . The spin pairing fraction monotonically decreases as U_{ab}/U increases. At $U_{ab}/U = 1$, we expect a pairing fraction of $1/3$ for a uniformly random spin ordering. (b) Numerical simulation of the full Bose-Hubbard model on a six-site chain. At higher U/t , the transition from the spin Mott (pairing fraction ≈ 1) to the spin superfluid (pairing fraction ≈ 0.5) happens more abruptly near $U_{ab}/U = 1$. Data kindly provided by Julius de Hond.

7.3.2 Adiabatic passage with a magnetic gradient

In the previous subsection, we have described our efforts on making an adiabatic passage toward the spin superfluid state by tuning the state-dependent lattice. However, one can also perform an adiabatic passage to a different but still interesting state, and it is performed by tuning an external magnetic gradient. We start with an analogy between the spin Mott state and the density Mott state to motivate the experiment to be described. Unlike the superfluid state, the density Mott state is robust against a potential gradient. However, as the strength of the gradient increases to the point where the energy offset between neighboring sites equals the Hubbard interaction U , then an initial $\langle \hat{n} \rangle = 1$ Mott state becomes energetically degenerate with a state with an alternating pattern of doublons and holons: $|2, 0, 2, 0, \dots\rangle$. If the gradient is swept adiabatically, it is possible to induce a transition between the two states. What is interesting is that this physics can be mapped to an antiferromagnetic transverse Ising model [111], where the effective Ising interaction is provided by the constraint that atoms are free to hop onto a neighboring site if the neighbor atom has not yet tunneled (the constraint energy scale is equivalent to the Hubbard interaction U) and the transverse field is provided by the tunneling amplitude. Another way to describe such a motion is that the restored first-order tunnelings are correlated by the aforementioned constraint.

Analogously, we can expose the spin Mott state, which is visualized as a chain of $|S_z = 0\rangle$, to a steep magnetic gradient. When the magnetic gradient strength is such that the energy offset becomes comparable to $2(J + D)$, two neighboring $|S_z = 0\rangle$'s will flip to pairs of $|S_z = -1\rangle$ and $|S_z = 1\rangle$, which can be detected as a reduction in the measured pairing fraction. The spin flip is performed by second-order tunneling, which is robust against the presence of a gradient. Similar to the case of the density Mott, the second-order tunneling or magnetic exchange has to be correlated in the sense that a spin can freely exchange with its neighbor as long as the neighbor has not already exchanged with some other spin. Thus, the demonstration of an adiabatic sweep from a spin Mott state to an antiferromagnetic texture will

be an interesting example of correlated magnetic exchanges and also accentuate the close analogy between the density Mott and the spin Mott.

The energy diagram for a six-site spin chain described by the anisotropic spin-1 model augmented by a magnetic gradient $\Delta \sum_i iS_{z,i}$ is shown in Fig. 7-11. The initial spin Mott state gets lost in a forest of intermediate states as we increase the gradient from zero. However, if we directly jump to intermediate values of the gradient ($\Delta/U \approx 0.2$ or $\Delta/U \approx 0.5$), the spin Mott state can be mapped to an excited state that has a relatively high pairing fraction. We can then make a transition toward the state with an antiferromagnetic spin texture (represented by the red coloring) either by starting from $\Delta/U \approx 0.3$ and increasing the gradient, or by starting from $\Delta/U \approx 0.5$ and decreasing the gradient. We note that the center of the largest avoided crossing is roughly around $\Delta/U = 0.3$, which is close to $2(D + J)/U$.

Since the Hubbard interaction energy scale U is typically $\mathcal{O}(1 \text{ kHz})$, in order to access a gradient strength of $\Delta/U = 0.5$, we need to provide an energy offset of approximately 500 Hz between neighboring sites. For $|a\rangle = |F = 1, m_F = -1\rangle$ and $|b\rangle = |F = 1, m_F = 1\rangle$ trapped in an 810 nm optical lattice, we need a magnetic gradient strength of 8.8 G/cm. While this is a modest gradient by any standard, because our side coils are located relatively far away from the atom cloud [28], we require a huge current [$\mathcal{O}(100 \text{ A})$] to achieve the required gradient. Nonetheless, we installed an extra power supply with a maximum rating of 250 A to the bias coil connections. The bias coil connections are set up so that before the gradient is enabled, a switch stops the current running in half of the Helmholtz pair, and then another switch enables the addition of the huge extra current running in an anti-Helmholtz fashion. Note that this leads to a reduction of the total bias and a possible rotation of the bias field. Because our total field consists of 8 G in the Tool direction and 3 G adding in quadrature, we expect the bias field to rotate by $\arctan(3/4) - \arctan(3/8) = 16^\circ$. We expect the effective vector-to-scalar ratio $R \cos \theta_k$ (see Sec. 4.2.1) to drop by 16%. At the time of this writing, we are still searching for an optimal gradient ramp.

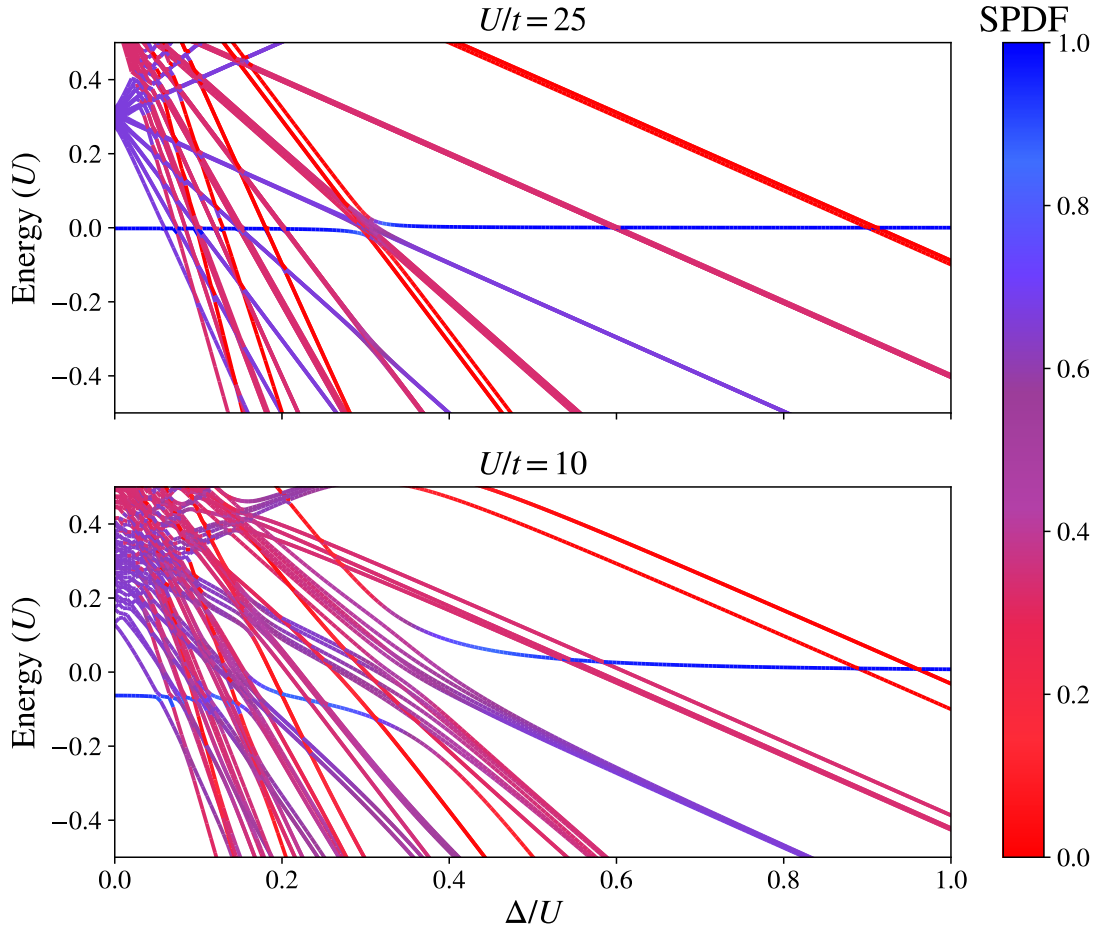


Figure 7-11: Energy diagram of the spin-1 model augmented by a magnetic gradient term $\Delta \sum_i i S_{z,i}$. The number of sites is 6, and $U_{ab}/U = 0.85$. $\sum_i S_{z,i}$ is constrained to zero. The Bose-Hubbard parameters are converted to the spin model parameters using Eq. 6.4. The coloring represents the average spin pairing fraction of the state. Top: $J_{xy} = 0.007 U$. The avoided crossings are very narrow. Bottom: $J_{xy} = 0.046 U$. The avoided crossings are visibly wider for certain transitions. If the transverse lattice depths are $35 E_{R,1064\text{nm}}$, $U/t = 25$ ($U/t = 10$) corresponds to $11.5 E_{R,810\text{nm}}$ ($8 E_{R,810\text{nm}}$). The interaction energy U at such lattice depths is typically $2\pi \times 1.2$ kHz.

Chapter 8

Conclusion

From an experimenter's point of view, quantum simulation with ultracold atoms requires many prerequisites to yield successful¹ results. It requires smooth and consistent operations of many different hardware devices (optics, electronics, and even something as mundane as air conditioners) and an acceptable understanding of a wide range of theoretical subjects in physics so that the signal (observable) of interest is defined and carefully measured. This thesis tries to convey some sense of the effort required to observe and report original studies of quantum many-body physics with ultracold atoms.

Chapter 2 describes in detail how the current rubidium quantum gas machine is run and has been incrementally improved over the years. It also points out many issues that need to be addressed in a future upgrade of the vacuum science chamber, such as the need for a precise feedback/feedback control of currents flowing through magnetic coils and prevention of hysteretic materials around the chamber. The chapter also has some useful details for beginning graduate students, such as independent methods to carefully calibrate the number of atoms in the prepared atom cloud.

Chapter 3 and 4 describes the theory of non-scalar light shift and how the resultant non-scalar light shift is used to control the interaction between different spin states within an optical lattice. The derivation of the non-scalar polarizability presented in

¹We generally define success here as an acceptable agreement between theory and experiment. Of course, not every disagreement is a failure! It could be a sign of a new discovery.

this thesis is unique in the sense that it tries to semi-rigorously explain the coupling of the circular polarizations to a vectorial light shift by analyzing the minimal mathematical structure for a light shift in the Cartesian basis, without delving directly into the formalism of spherical tensors. Chapter 4 provides a short but more detailed explanation of how to compute the Wannier basis for optical lattices and a wide survey of currently known experimental techniques for generating a state-dependent lattice potential. It is hoped that the details presented in Chapter 4 will be useful for future researchers trying to do high-fidelity state-dependent control with polarization gradients within optical lattices.

Chapter 5 describes the basic physics of the Bose-Hubbard model and presents an useful guide on how to compute the estimated volumes of the Mott phases within the atom cloud given the experimental settings. It is important that the atoms are initialized into the ground state of the Mott insulating phase before effective spin models can be studied within the Mott phase, and one way to verify that is to compare the equilibrium density distribution inside a Mott insulator to the measured density distribution inside the optical lattice. The discrepancy between the calculation and the measurement mentioned in the chapter shows that more work needs to be done on optimal lattice ramps. The chapter also provides some calculation of the corrections to the Hubbard parameters due to the interaction-induced admixture of higher-band orbitals into the on-site wavefunction. While the corrections are not taken into account for our spin model experiment, it will need to be taken into account when a quantitatively accurate analysis is due for experimental data with low noise.

Chapter 6 describes how the low energy physics of a Mott insulator is captured by an effective spin model. The chapter explains how to obtain the spin model parameters from the Bose-Hubbard parameters in a systematic manner and derives corrections to the spin-1 model parameters that have not been discussed elsewhere. The chapter concludes with a discussion of how one may obtain spin-1 correlations from density correlation measurements without high-resolution imaging, although experimental hurdles are likely to be just as high while only returning a reduced signal.

The derivations and detailed explanations of the preceding five chapters are put into good use in Chapter 7, which describes two different studies of the spin-1 model: non-equilibrium dynamics in a state-independent lattice and ground state control in a state-dependent lattice. Study of coherent spin exchange was a long standing goal of the rubidium lab, and the accumulated efforts in hardware improvement and theoretical understanding lead to the first observation of magnetic exchange in a spin-1 model realized with ultracold atoms. The chapter also discusses the on-going investigation of the spin Mott phase and provides useful calculations and suggestions for the remaining work to be done.

There are still many discrepancies between measurements and calculations to be resolved. It is hoped that the imminent upgrade of the vacuum science chamber and the surrounding optical layouts will transform the experiment into a more consistent and stable platform. The jewel of the planned upgrade is the new high-resolution objective that will allow us to see individual atoms in lattice sites and give us a better idea of what is actually going on inside the optical lattice. Also, single-site addressing capability enabled by such an objective will be a useful tool for studying spin physics. A unique capability of quantum simulation experiments with ultracold atoms is the ability to prepare a variety of initial states not accessible in other settings such as traditional condensed matter experiments. The objective can be used to inject carefully calibrated spin excitations into the spin system and perform a precise study of non-equilibrium spin dynamics. Although I have been involved in the planning for the proposed upgrade to a quantum gas microscope for a long time, it will be in the hands of the junior and future graduate students of the rubidium lab to implement the upgrade - and the lab is in good hands for the upgrade.

In terms of the scientific outlook, the main contribution of the rubidium lab will continue to be the study of two-component physics in the $\langle \hat{n} \rangle = 2$ Mott insulator phase, which has not received as much as attention as the $\langle \hat{n} \rangle = 1$ Mott phase as an experimental platform. The presence of the on-site interaction is essential for the single-ion anisotropy (SIA), and it turns out that the SIA leads to qualitatively something new in the spin model. Specifically, for a negative value of the SIA strength,

magnons (visualized as a spin flip to $|S_z = 0\rangle$ in a ferromagnetic background of $|S_z = 1\rangle$) can form a bound state (a pair of neighboring $|S_z = 0\rangle$) where an effectively attractive interaction is provided by the SIA, via tunneling of the paired $|S_z = 0\rangle^{\otimes 2}$ into $|S_z = 1\rangle|S_z = -1\rangle$ and $|S_z = -1\rangle|S_z = 1\rangle$ and hence lowering of the total energy [108]. This is a new type of magnon interaction that is not possible in the often studied spin-1/2 model. There is experimental evidence from solid state physics that the strength of this effective magnon-magnon interaction is renormalized at higher magnon densities [108], and it would be interesting to study the dynamics of the spin-1 model with a precisely calibrated density of magnons injected into the chain. For this, local addressing by a quantum gas microscope will be essential. The local addressing capability may be also crucial for improving the understanding of our adiabatic ramp from the spin Mott state to the spin superfluid state. We may be actually able to carve out a single chain of doubly-occupied sites, so that we do not have to worry about the effects of surrounding $\langle \hat{n} \rangle = 1$ Mott phase or superfluid shells during the adiabatic ramp. Another useful tool to add in the future is resonant spin-changing collision [98], which can initialize a spin Mott state in a deep lattice with no physical separation between the two-component atoms. Such an initialization avoids all the complications of ramping a two-component atomic gas into a Mott insulator, and one can still use the state-dependent lattice to control the spin-dependent interaction after the initialization. However, one will need a flexible magnetic field control that can change the bias field for more than 8 G without any hysteresis or substantial eddy currents. Some care must be put into the microwave control as well in order to make the spin changing process fully resonant. The sum of all the suggested additions to the experiment makes up a challenging upgrade, but for a “conventional” atomic species like rubidium, it would be good to have all the “unconventional” tools at disposal to have a chance of discovering new physical phenomena with the quantum simulator.

Appendix A

Quantum Gas Microscope

In this appendix we describe some of the technical challenges for the installment of a quantum gas microscope system and provide some suggestions for solutions.

A.1 Optical aberration

High numerical aperture imaging requires stringent minimization of wavefront aberration as the collected fluorescent light goes through various optical surfaces. Not only must the microscope objective be of high quality and must it be tested to be diffraction-limited in its performance, but surfaces such as vacuum windows, mirrors and filters must impart as little wavefront deformation as possible. It is possible that while the optical component itself has good flatness, its quality may be degraded by mechanical stress from poor mounting or bonding. While high-quality mirrors, filters and optomechanical components can be bought from vendor catalogs, high-quality vacuum windows in vacuum flanges require custom orders and may not preserve their flatness despite the vendors' best efforts. Therefore, it is important to understand how much degradation can be caused by vacuum window deformation.

Before we explain the subtleties of vacuum window deformation, it is important to understand the different types of aberration that may be present. In geometric optics, the wavefront error of a rotationally symmetric imaging system can be shown to only depend on object height and exit pupil polar coordinates [112], yielding a power

series expansion of the wavefront error function in those three variables. The first two terms, which are quadratic in the variables, are focus and tilt, which can be always adjusted away. The next five terms, which are quartic in the variables, are known as primary or Seidel aberrations and consist of spherical aberrations, coma, astigmatism, field curvature and distortion. Their effects on geometrical beam spot are described in [112]. Spherical aberration is special in that it only depends on the exit pupil radius. Because of its independence from objective height and exit pupil angle, a single corrector plate at the exit pupil can compensate the aberration for all locations on the object plane. On the other hand, the other primary aberrations are dependent on both objective height and exit pupil coordinates, and thus a corrector plate at the exit pupil can only correct the image of an object at a specific location. The conclusion is that axially symmetric deformation is acceptable to some degree, but asymmetric deformation must be avoided if possible as it cannot be easily compensated.

Unfortunately, vacuum windows are likely to have axially asymmetric deformations. Vacuum windows are typically bonded to a metal alloy sleeve, which is then welded to the stainless steel flange. If there is asymmetric radial stress during either glass-to-metal bonding or sleeve-to-metal welding, the window will bend preferentially along some direction, yielding a saddle-like deformation. The window will still maintain its thickness and hence preserves its transmission wavefront error, so that the deformation poses no problem for collimated light. However, since the vacuum window is the first optical surface through which the diverging cone of fluorescent light from atoms passes, the deformation, as measured by reflection wavefront error in interferometers, can impart a substantial effect.

Without understanding the internals of a high numerical aperture (NA) imaging objective, we can derive the acceptable level of window surface deformation given the working distance and the specified NA of the objective, and the thickness of the window. Consider the geometry in Fig. A-1, where fluorescing atoms are placed working distance away from the vacuum side of the window. Our assumption is that for any given ray emanating from the atoms, the objective as a blackbox adjust the total optical path lengths (OPL) so that the ray arrives at the focal point by

a fixed but practically unknown amount of time. In other words, we assume that the objective itself is a perfect imaging system and we apply Fermat's principle for propagation of light.

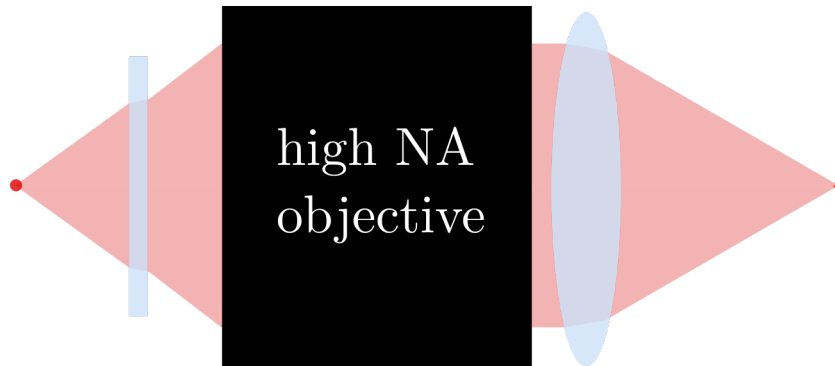


Figure A-1: Objective as a perfect blackbox imaging system. While the finite thickness of the front vacuum window can impart aberrations such as spherical aberration, the blackbox compensates for such effects so that all the rays from the atoms that can fit inside the exit pupil of the blackbox are focused onto the focal point. In other words, the blackbox does whatever it needs to do so that Fermat's principle holds for all the rays with the start point at the atom and the end point at the focal point.

Once the vacuum window starts to deform as in Fig. A-2(b), the balance of OPL performed by the blackbox is broken, and some rays do not focus onto the previous focal point anymore. We assume that the deformation is small enough so that the rays exiting the window do not significantly change in their angles and positions. In experience, high-quality vacuum windows in metal flanges come with peak-to-valley deviation of a few wavelengths over the clear aperture, so this is a reasonable assumption. If the ray angle and position were to change greatly after the deformed window, then the blackbox output cannot be easily predicted as it was built to compensate for specific aberrations caused by the originally flat window. In other words, we assume the change in the OPL inside the window glass is the only substantial perturbation by the deformation.

If a ray strikes a flat window at an angle θ as in Fig. A-2(a), the OPL inside the glass is

$$OPL_g(\theta) = \frac{n_g d}{\sqrt{1 - \sin^2 \theta / n_g^2}}$$

where n_g is the refractive index of the glass and d is the thickness of the window. If the window starts to bend, the incidence angle of the ray at the window deviates from θ . Now we assume the deformation of the window is described by a parabola $(PV)r^2/R^2$, where PV is the peak-to-valley deformation in units of wavelengths, $R = WD \tan(\arcsin \text{NA})$ is the radius of the clear aperture over which the deformation is measured, and $r = WD \tan \theta$ is the radial position where the ray strikes the glass. The slope of the parabolic deviation is

$$\delta\theta = 2\frac{PV}{R^2}WD \tan \theta$$

. Thus, the change in the OPL inside the glass is

$$\Delta OPL_g(\theta) = OPL_g(\theta) - OPL_g(\theta - \delta\theta)$$

If the surface deformation is parabolic and axially symmetric, the resulting aberration is a defocus term that can be fully compensated. However, because of the aforementioned saddle-shaped deformation, we assume the sign of the parabola is different between the two orthogonal axes on the surface. This is the essence of astigmatism: different focal lengths between x-axis and y-axis. Figure A-2(c) plots $\Delta OPL_g(\theta)$ in units of wavelength for $PV = 1\lambda$ and for two different values of WD: 6.5 mm (that of the new BEC4 objective) and 2.5 mm. The Rayleigh criterion¹ for diffraction-limited imaging states that a the wavefront deformation must be less than $\lambda/4$ [112]. Note that this condition is necessary but not sufficient for diffraction-limited imaging [113]. We see that for WD = 6.5 mm we lose diffraction-limited imaging performance around NA = 0.57, which is close to what Zemax simulation of the actual objective and the aberrated window predicts (around NA \approx 0.6). On the other hand, WD = 2.5 mm shows a higher likelihood of maintaining diffraction-limited imaging up to the specified NA of 0.8. The conclusion is that for high-NA objectives with long working distance, peak-to-valley deformation must be less than $\lambda/4$, and if this specification

¹A heuristic argument is that wavefront deviation beyond $\lambda/4$ leads to destructive information between Huygens wavelets at the focus.

cannot be met, the objective needs to be designed for a shorter working distance, at the cost of a reduced optical access to the atoms from the side.

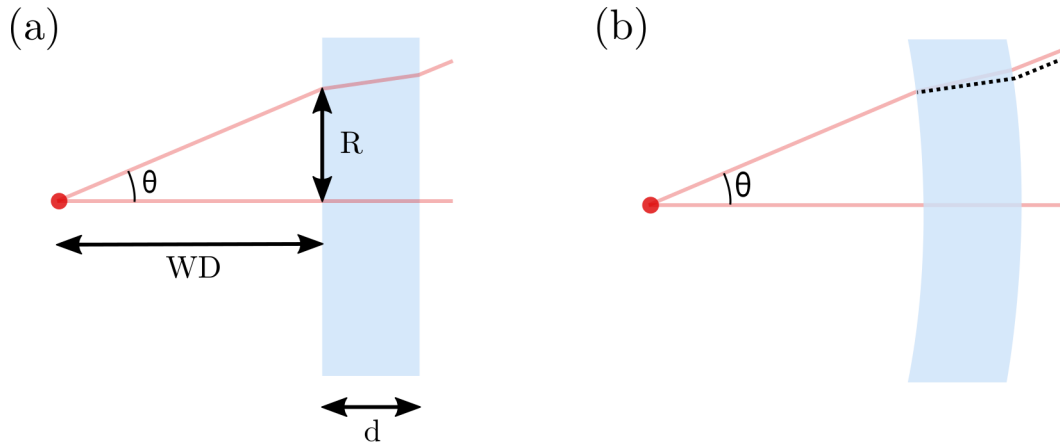
A.2 Strategy for a high-flatness vacuum window

Usually the vacuum window glass is bonded to a metal alloy that forms a ferrule, and the ferrule is later joined to a metal alloy sleeve that is connected to the rest of the metal flange (Fig. A-3). The selection of the ferrule material is important, as the use of more flexible materials reduces the possibility of deformations. For example, using a tantalum sleeve resulted in a much better deformation [(reflection wavefront error of $\mathcal{O}(\lambda)$] than an Inconel sleeve [$\mathcal{O}(100\lambda)$], although the improvement could have also come from a smaller welding area between the sleeve and the ferrule for the tantalum sample. The choice of materials is severely constrained by the requirements that the material be non-magnetic and easily weldable.

If the windows end up deformed, the next option is to polish the glass. In principle, it is straightforward and fairly standard to polish a glass down to peak-to-valley deviation of $\lambda/20$ or better. However, the requirement is that the polishing tool can access the entire surface of the glass and have the room to move from one edge to the other [114]. Magnetorheological fluid (MRF) polishing can correct the surface deformation over an arbitrary aperture in principle, but the final quality and ease of polishing still depends on the initial flatness of the window. In our experience, all MRF polishers have refused to work on our deformed windows because it is hard to access the full area of the glass and would take too much time (and hence opportunity cost) to polish the glass down to the specified level. There is a contact-free polishing technique called ion beam figuring (IBF) but convincing a vendor to work on the sample despite the opportunity cost was also an issue.

If the high-end polishing techniques are not available, then making a home-made vacuum window is an option, as some other cold atom groups have done by gluing a glass to a metal flange [115]. We are currently pursuing this option, but the main challenge is to prevent a slow rise in the vacuum pressure, possibly due to some

components in the epoxy.



(c) $\lambda = 0.780 \text{ nm}, n = 1.45$
 $D = 5 \text{ mm}, R = 8.67 \text{ mm}$

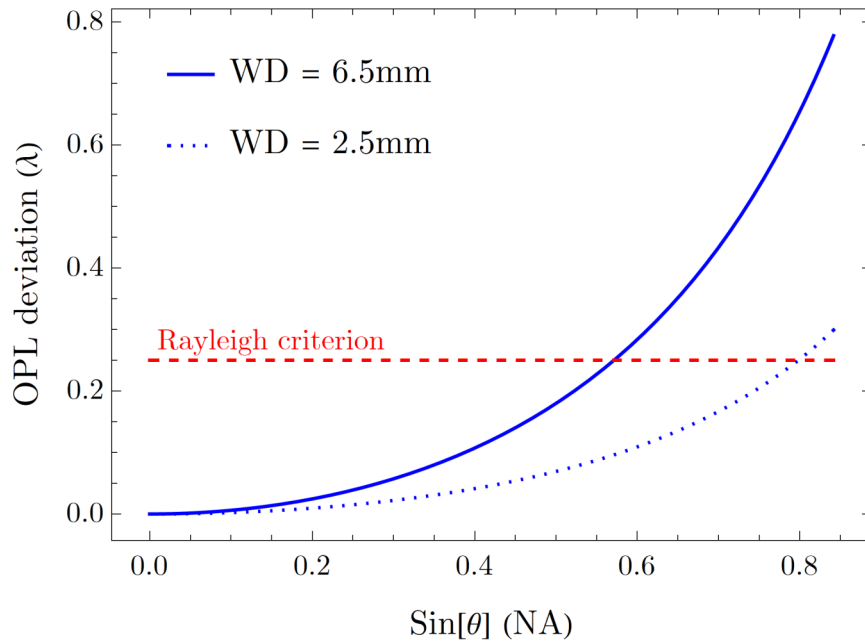


Figure A-2: Effect of vacuum window deformation on wavefront error. (a) Geometry of the setup. “WD” stands for working distance, “d” thickness of the vacuum window, and “R” the radius of the area illuminated by the light cone from the atom. (b) When the vacuum window curves under stress, the optical path length (OPL) inside the glass deviates from the original value (black dotted line). Note the terminal separation between the new trajectory and the old trajectory is greatly exaggerated for clear view. (c) Calculation of the change in the OPL inside the glass induced by a parabolic deviation from a flat surface (peak-to-valley error of λ over $2R = 17.3 \text{ mm}$). For $WD = 6.5\text{mm}$, the objective is no longer diffraction limited around $NA = 0.55$. For a smaller WD of 2.5 mm , diffraction-limited performance may be maintained up to high NA.

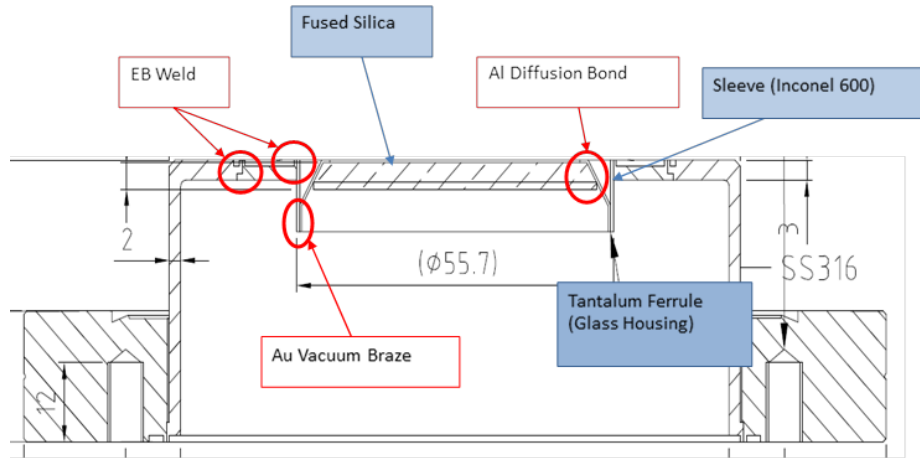


Figure A-3: An example vacuum viewport structure. Picture courtesy of UKAEA.

Appendix B

Tunable Single-Ion Anisotropy in Spin-1 Models Realized with Ultracold Atoms

This appendix contains a reprint of Ref. [24]: Woo Chang Chung, Julius de Hond, Jinggang Xiang, Enid Cruz-Colón, and Wolfgang Ketterle, *Tunable Single-Ion Anisotropy in Spin-1 Models Realized with Ultracold Atoms*, Physical Review Letters **126**, 163203 (2021).

Tunable Single-Ion Anisotropy in Spin-1 Models Realized with Ultracold Atoms

Woo Chang Chung¹, Julius de Hond¹, Jinggang Xiang (项晶罡)¹, Enid Cruz-Colón, and Wolfgang Ketterle¹
*Research Laboratory of Electronics, MIT-Harvard Center for Ultracold Atoms, Department of Physics,
 Massachusetts Institute of Technology, Cambridge, Massachusetts 02139, USA*



(Received 4 January 2021; accepted 18 March 2021; published 23 April 2021)

Mott insulator plateaus in optical lattices are a versatile platform to study spin physics. Using sites occupied by two bosons with an internal degree of freedom, we realize a uniaxial single-ion anisotropy term proportional to $(S^z)^2$ that plays an important role in stabilizing magnetism for low-dimensional magnetic materials. Here we explore nonequilibrium spin dynamics and observe a resonant effect in the spin alignment as a function of lattice depth when exchange coupling and on-site anisotropy are similar. Our results are supported by many-body numerical simulations and are captured by the analytical solution of a two-site model.

DOI: 10.1103/PhysRevLett.126.163203

Mott insulators of ultracold atoms in optical lattices comprise a widely used platform for quantum simulations of many-body physics [1]. Since the motion of atoms is frozen out, the focus is on magnetic ordering and spin dynamics in a system with different (pseudo)spin states. As suggested in 2003, Mott insulators with two-state atoms realize quantum spin models with tunable exchange interactions and magnetic anisotropies [2,3]. Experimental achievements for spin-1/2 systems include the observation of antiferromagnetic ordering of fermions [4] and the study of spin transport in a Heisenberg spin model with tunable anisotropy of the spin-exchange couplings [5]. Spin dynamics for $S > 1$ has also been investigated [6].

However, all studies thus far have exclusively addressed spin systems with occupations of one atom per site. This limits spin Hamiltonians to spin-exchange terms between different sites i, j proportional to $\sum_{\langle ij \rangle} S_i^k S_j^k$ (where $k \in \{x, y, z\}$) and to Zeeman couplings to effective magnetic fields, proportional to $\sum_i S_i^z$. For Mott insulators with two or more atoms per site, the Hubbard model has direct on-site interactions that can give rise to a nonlinear term $D \sum_i (S_i^z)^2$, where D is the so-called single-ion anisotropy constant. $(S^z)^2$ terms, which are present for $S \geq 1$ only, are important for establishing nontrivial correlations such as in spin squeezing [7]. In spin-1 models, such terms can lead to a qualitatively new magnetic phase diagram [8,9]. For example, for ferromagnetic spin-1 Heisenberg models, the single-ion anisotropy gives rise to a gapped spin state (the “spin Mott insulator”) that can be used as an initial low-entropy state for an adiabatic ramp toward a highly correlated gapless spin state (the XY ferromagnet) [10,11]. For antiferromagnetic systems in one dimension, the single-ion anisotropy leads to a quantum phase transition between a topologically trivial phase and a nontrivial phase as predicted by Haldane [12–14]. The magnetic properties of many materials crucially depend on crystal field

anisotropies that break rotational symmetry and can stabilize ferromagnetism in two-dimensional materials by avoiding the Mermin-Wagner theorem, which forbids long-range order for continuous symmetries [15,16]. The interest in spin-1 systems is demonstrated by various studies on different platforms [17–19].

In this Letter, we use cold atoms in optical lattices to implement a spin-1 Heisenberg Hamiltonian using a Mott insulator of doubly occupied sites and demonstrate dynamical features that arise from the single-ion anisotropy. For spin-exchange interactions studied thus far in optical lattices, the only timescale for dynamics is second-order tunneling (i.e., superexchange), which monotonically slows down for deeper lattices. In contrast, as we show here, the single-ion anisotropy introduces a new timescale, and we find a dynamical behavior that is faster in deeper lattices due to a resonance effect when the energies of superexchange and single-ion anisotropy are comparable.

We present a protocol to directly measure the anisotropy in the spin distribution and find a pronounced transient behavior of this quantity when the resonance condition is met. Transients change sign along with the single-ion anisotropy. We find good agreement with theoretical simulations and explain the most salient features using a two-site model with an exact solution.

In the Mott insulator regime, the optical lattices are sufficiently deep that the on-site interaction suppresses first-order tunneling, and exchange processes are only possible via second-order tunneling. For two atoms per site with two internal states, the Bose-Hubbard Hamiltonian is approximated by an effective spin Hamiltonian

$$H = -J \sum_{\langle ij \rangle} \mathbf{S}_i \cdot \mathbf{S}_j + D \sum_i (S_i^z)^2 - B \sum_i S_i^z, \quad (1)$$

where \mathbf{S}_i are spin-1 operators, $\langle ij \rangle$ are pairs of nearest-neighbor sites, J is the exchange constant, D is the uniaxial single-ion anisotropy constant, and B is a fictitious magnetic bias field. The spin-1 operators are related to the boson creation and annihilation operators via $S_i^z = (a_i^\dagger a_i - b_i^\dagger b_i)/2$, $S_i^+ = a_i^\dagger b_i$, $S_i^- = b_i^\dagger a_i$ under the constraint $a_i^\dagger a_i + b_i^\dagger b_i = 2$, where a_i and b_i are boson annihilation operators at site i for state a and state b , respectively. In terms of the tunneling amplitude t and interaction energies $U_{\sigma\sigma'}$: $J = 4t^2/U_{ab}$ and $D = (U_{aa} + U_{bb})/2 - U_{ab}$, where $U_{\sigma\sigma'}$ represents the on-site interaction energy between atoms in two states $\sigma, \sigma' \in \{a, b\}$. The term proportional to B can be dropped if the total longitudinal magnetization $\sum_i S_i^z$ is constant, as it is in the experiment.

For the species studied here, ^{87}Rb , all $U_{\sigma\sigma'}$ differ by less than 1%, and therefore all spin-exchange couplings are almost equal, resulting in isotropic spin Hamiltonians for site occupancy $\nu = 1$. However, for $\nu = 2$, we can tune the relevant anisotropy parameter D/J over a large range of values because J decreases exponentially with lattice depth while D —a differential on-site energy—slowly increases.

The experimental sequence begins by preparing a Bose-Einstein condensate (BEC) of ^{87}Rb atoms in the $|F = 1, m_F = -1\rangle$ hyperfine state inside a crossed optical dipole trap. The sequence proceeds by loading the BEC into a deep three-dimensional optical lattice formed by retroreflected lasers with wavelengths of $\lambda = 1064$ nm. The lattices are ramped to final depths of $30E_R$ in 250 ms, where $E_R = \hbar^2/(2m\lambda^2)$ is the recoil energy for atomic mass m . Experimental parameters are chosen to maximize the size of the $\nu = 2$ Mott-insulator plateau without significant population of sites with $\nu = 3$ [see Fig. 1(a) and Ref. [20]].

To allow for spin dynamics, all atoms are rotated into an equal superposition of two hyperfine states $(|a\rangle - i|b\rangle)/\sqrt{2}$ using a combination of microwave pulses [20]. This initial state is a simple product state. Negative and positive values of D are realized with the pairs $|a\rangle = |1, -1\rangle$, $|b\rangle = |1, 1\rangle$ and $|a\rangle = |1, -1\rangle$, $|b\rangle = |1, 0\rangle$, respectively [20]. The spin-exchange dynamics in one-dimensional chains is initiated by a 3-ms quench, during which we ramp down the longitudinal lattice to a variable depth while the transverse lattices are ramped up to $35E_R$ [Fig. 1(b)]. After a variable evolution time, the final spin configuration is “frozen in” by ramping the longitudinal lattice to $35E_R$ as well [Fig. 1(c)].

Our observable for the anisotropy in the spin distribution is the longitudinal spin alignment $A = S(S+1) - 3\langle (S^z)^2 \rangle$, measured in the $\nu = 2$ plateau. $\langle (S^z)^2 \rangle = \sum_{i=1}^N \langle (S_i^z)^2 \rangle / N$ is the average on-site longitudinal spin correlation. A is defined to be zero for a random distribution of spins. Since $S^z = 1, 0, -1$ for the $|aa\rangle$, $|ab\rangle$, and $|bb\rangle$ doublons, respectively, A can be obtained by measuring the relative abundance of the different doublons. Specifically, we refer to the fraction of $|ab\rangle$ doublons as the “spin-paired doublon fraction” f .

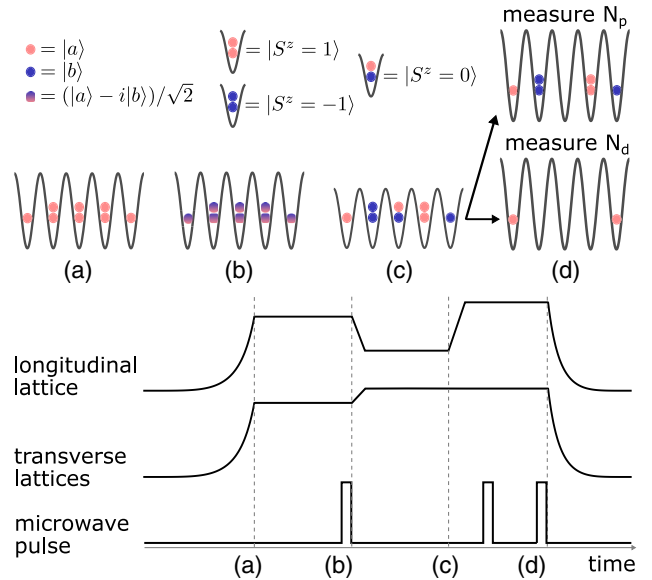


FIG. 1. Experimental sequence for the measurement of spin alignment and doublon fractions. (a) The lattices are ramped up to initialize a single-component Mott insulator with a maximal site occupancy of two. (b) Microwave pulses prepare a superposition of two hyperfine states $(|a\rangle - i|b\rangle)/\sqrt{2}$. Ramping down the longitudinal lattice initiates spin-exchange dynamics. (c) Ramping up the lattices stops the exchange dynamics. Microwave pulses transfer the two components to a pair of states with a Feshbach resonance. (d) Either $|ab\rangle$ doublons or all doublons are removed with the help of Feshbach-enhanced inelastic losses. The remaining atoms are transferred back to the $F = 1$ hyperfine states and are counted via absorption imaging to measure N_p or N_d .

Since $\langle (S^z)^2 \rangle = 1 - f$, we obtain $A = 3f - 1$. The doublon statistics can be measured by selectively introducing a fast loss process that targets a specific type of doublon and by comparing the remaining total numbers of atoms, which are measured via absorption imaging. Specifically, if N_a is the average total atom number in the whole cloud, N_p the average number of remaining atoms after removing $|ab\rangle$ doublons, and N_d the average number of remaining atoms after removing all doublons, then $f = (N_a - N_p)/(N_a - N_d)$ [Fig. 1(d)]. Fast losses of doublons are induced by transferring the atoms to hyperfine states for which inelastic two-body loss is enhanced near two narrow Feshbach resonances around a magnetic field of 9 G [20,28]. Since f and A are obtained from the ratio of differences in atom numbers, good atom number stability in the experiment (the deviation from mean being typically $< 4\%$) was crucial to measure A with sufficiently small uncertainties.

For the initial state, $f = 1/2$ and $A = 1/2$. Over times that are long compared to the spin-exchange timescale \hbar/J , heating processes drive the system toward thermal equilibrium with $A = 0$. At short times, coherent spin dynamics is observed: If D is negative, the $|aa\rangle$ and $|bb\rangle$ doublons are energetically favorable, and we expect f and A to decrease. If D is positive, the $|ab\rangle$ doublons are

favorable, and we expect f and A to increase. If D is zero, the system is described by an isotropic spin-1 Heisenberg Hamiltonian of which the initial state is an eigenstate. By fixing the hold time and scanning the value of the lattice depth for the spin chains, we can monitor the impact of D/J on the dynamical change in A . For positive (negative) D , we chose a hold time of 70 ms (25 ms). These hold times are chosen to be comparable to \hbar/J when $|D/J| \sim 1$ [20].

Figure 2 shows that for $|D/J| \ll 1$ or $|D/J| \gg 1$, A stays near its initial value of $1/2$. However, when $D/J \sim 2$, which corresponds to a longitudinal lattice depth of $14E_R$ ($11E_R$) for positive D (negative D), we see that A reaches a maximum (minimum). This nonmonotonic change of A with lattice depth is indicative of the interplay between spin-exchange and single-ion anisotropy. In addition, we observe that the change in A is smaller for positive D than for negative D .

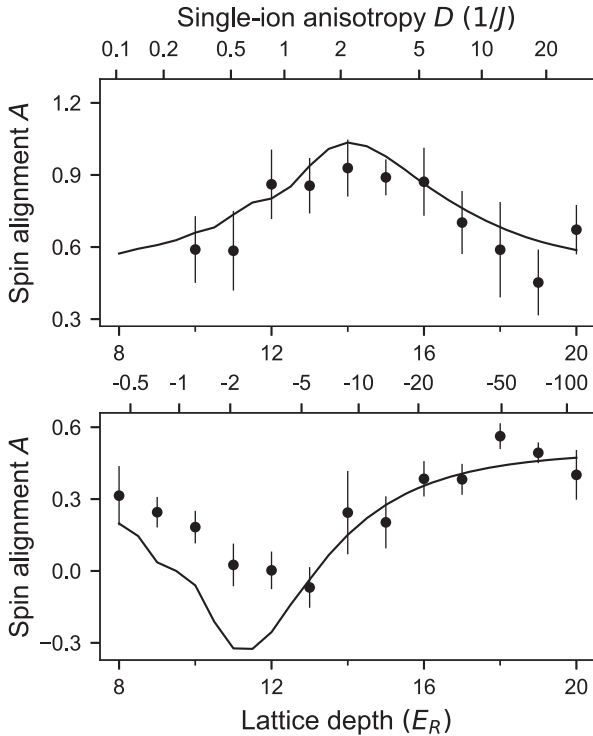


FIG. 2. Transient enhancement and reduction of the spin alignment A by coherent spin dynamics. The change in A is strongest when $|D/J| \sim 2$. Measurements were done for both positive (top) and negative (bottom) values of D/J . The atoms were held for 70 ms and 25 ms, respectively (also see Fig. 4). The top axis in both figures indicates the D/J ratio. Solid lines are the results of matrix-product state–time-evolving block decimation (MPS-TEBD) calculations. The error bars represent the standard error of the mean for A , obtained by error propagation after averaging three measurements for each of N_a , N_p , and N_d . We found the error bars to be dominated by fluctuations in prepared atom number over systematic errors. For the lowest lattice depths, the spin model may not fully represent the Bose-Hubbard model.

Several aspects of the observed spin dynamics can be captured by a two-site model. Although states on two spin-1 sites span a 9-dimensional Hilbert space, we can reduce the spin dynamics to a beat note between two states. Since exchange interactions do not change the total magnetization $\sum_{i=1}^N S_i^z$, the Hilbert space factorizes to subspaces with the same total magnetization (although S_i^z can differ within a subspace). Furthermore, the initial superposition state is symmetric between the left and right wells, and any change in A comes from the two coupled states: $|ab\rangle_L|ab\rangle_R$ and $(|aa\rangle_L|bb\rangle_R + |bb\rangle_L|aa\rangle_R)/\sqrt{2}$, for which A equals 2 and -1 , respectively (Fig. 3). By describing these two states as two poles on a Bloch sphere, we see that the initial state is represented by a vector pointing somewhere between the north pole and the equator with a vertical fictitious external field. The quench in J and D suddenly changes the strength and the orientation of this external field and induces a precession of the state vector around the new external field [20]. This results in an oscillation of A with amplitude

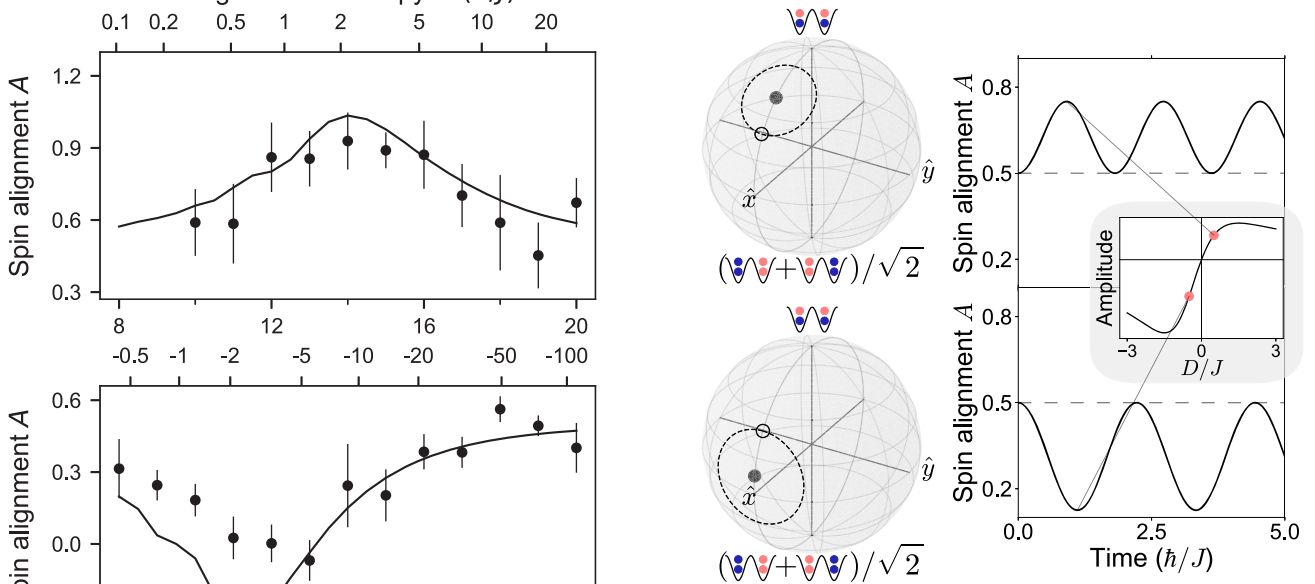


FIG. 3. Coherent spin oscillations in a two-site model. While the full basis contains nine states, the oscillations in the spin alignment A involve only a 2×2 block of the Hamiltonian. This allows us to illustrate the dynamics on Bloch spheres (left), where the initial state is represented by the open circle. If $J = 0$, the effective magnetic field points along \hat{z} , and the purely azimuthal precession will not change A . If $J > 0$, the effective magnetic field is tilted, resulting in a precession along the dashed circle, which is observed as an oscillation in A (right). The frequency of the oscillation, in units of J/\hbar , is given by $\Omega = \sqrt{9 + 4D/J + 4(D/J)^2}$, and its peak-to-peak amplitude is $6(D/J)/[9 + 4D/J + 4(D/J)^2]$ (see inset). This shows that the direction of oscillation depends on the sign of D/J (compare top and bottom rows, where $D/J = 0.5$ and -0.5 , respectively). Note that while the initial value of A for this subspace is 1, the contribution of other states sets the initial A of the whole system to $1/2$.

$6(D/J)/[9 + 4D/J + 4(D/J)^2]$. This function has local extrema for $D/J = \pm 3/2$ but is not symmetric around $D/J = 0$. This explains the nonmonotonic behavior as a function of lattice depth and shows why the contrast is smaller for positive D/J than for negative D/J .

One would expect that, for a larger number of sites, additional precession frequencies appear, turning the periodic oscillation for two sites into a relaxation toward an asymptotic value, which, according to the eigenstate thermalization hypothesis, represents a low-temperature

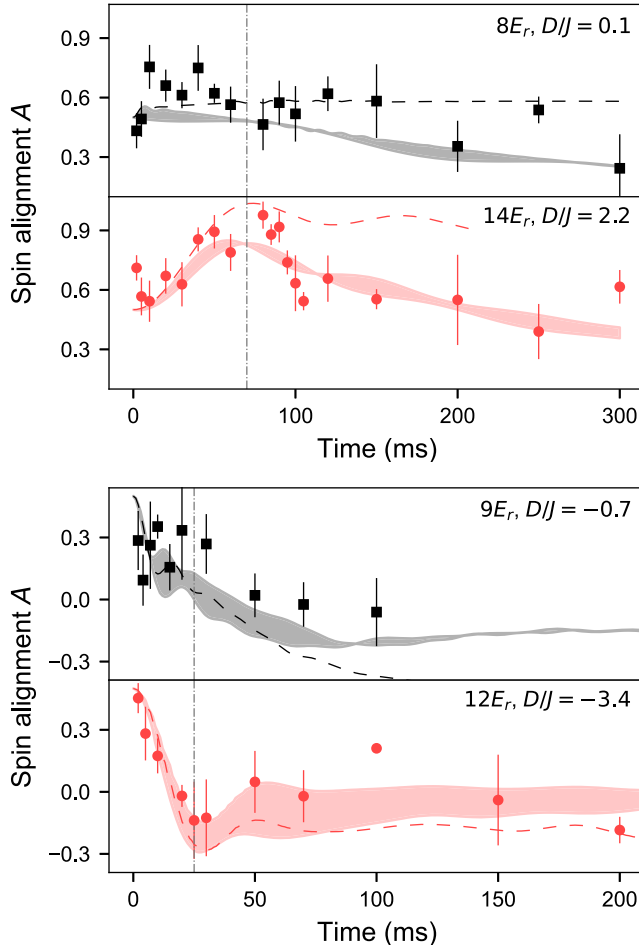


FIG. 4. Coherent dynamics of the spin alignment A after a quench in D/J . Varying the hold time at characteristic lattice depths for both positive and negative values of D/J (top and bottom pairs of panels, respectively) reveals that strong transients in A only occur at intermediate lattice depth for which D and J are comparable. The vertical dash-dotted lines indicate the hold times used for these pairs in Fig. 2. Dashed lines are the results of the MPS-TEBD simulation. The shaded regions denote the MPS-TEBD results with $\pm 0.5E_R$ uncertainty in the lattice depths and include exponential decay toward a thermal spin state with $A = 0$ with empirical $1/e$ times of 350 ms ($D > 0$) and 175 ms ($D < 0$), the ratio of which reflects the relative sensitivity to ambient magnetic field fluctuations of the pairs. The error bars are computed in the same manner as those in Fig. 2.

equilibrium [29]. Comparison between the two-site model and a many-site model numerically simulated using the time-evolving block decimation for matrix-product states (MPS-TEBD) shows that the initial change in A is indeed well captured by the two-site model [20]. Because of the spin dynamics, the system evolves from a product state into a highly correlated state with entanglement between sites; this has been the focus of recent theoretical works [30,31]. In the two-site model, the von Neumann entanglement entropy can reach up to $\sim 0.9 \times \ln(3)$ due to the interplay between single-ion anisotropy and exchange terms. This corresponds to an almost maximally entangled state since $\ln(3)$ is the maximum entropy for a spin-1 site.

To show that changes in the spin alignment A result from competition between the exchange interaction and the single-ion anisotropy, we study the time evolution of A at two different lattice depths (Fig. 4). For positive D , MPS-TEBD simulations predict very little change in A at a lower lattice depth, where the exchange constant is relatively large, but the anisotropy is small, while it predicts a noticeable change in A at a higher lattice depth, where the exchange constant and the anisotropy term become comparable. While the simulation predicts equilibration of A to an asymptotic value (thin lines), measurements show that it decays toward a lower value for positive D and does not decrease as much as the simulation predicts for negative D . The measurements are consistent with the fact that at high spin temperatures, the spin distribution becomes isotropic and A vanishes. Indeed, when we ramp down the lattices and retrieve a BEC, we observe a significant reduction of the condensate fraction after 300 ms. This represents the timescale over which entropy is either transported through the cloud or created by heating. It could possibly be extended by better stabilizing ambient field fluctuations or by adding a tilt to suppress entropy transport by holes [32].

In conclusion, we have implemented a spin-1 Heisenberg model with a single-ion anisotropy using the $\nu = 2$ plateau of a Mott insulator and have observed the subtle interplay between spin-exchange and on-site anisotropy in coherent spin dynamics. Much larger values of D can be implemented with spin-dependent lattices, which will allow us to observe much faster anisotropy-driven dynamics and will also enable mapping out the phase diagram of the anisotropic spin Hamiltonian [11]. It should also be noted that it is possible to change the sign of J with the gradient of an optical dipole potential [32,33], which will permit exploration of the antiferromagnetic sector with bosons. Interesting dynamical features of anisotropic spin models have been predicted [34], including transient spin currents, implying counterflow superfluidity.

Regarding quantum simulations, single-ion anisotropies play a crucial role in magnetic materials (e.g., monolayers containing chromium [35,36]). In such materials, crystal field effects lift the degeneracy of d orbitals, and spin-orbit

interaction transfers this anisotropy to the electronic spins responsible for the magnetism [37]. Here we have simulated this anisotropy by selecting a pair of atomic hyperfine states where the interspecies scattering length is different from the average of the intraspecies values. This illustrates the potential for ultracold atoms in optical lattices to implement idealized Hamiltonians describing important materials.

We thank Colin Kennedy, William Cody Burton, and Wenlan Chen for contributions to the development of experimental techniques and Ivana Dimitrova and Andrew Daley for their critical reading of the manuscript. We acknowledge support from the NSF through the Center for Ultracold Atoms and Grant No. 1506369, ARO-MURI Non-equilibrium Many-Body Dynamics (Grant No. W911NF14-1-0003), AFOSR-MURI Quantum Phases of Matter (Grant No. FA9550-14-1-0035), ONR (Grant No. N00014-17-1-2253), and a Vannevar-Bush Faculty Fellowship. W.C.C. acknowledges additional support from the Samsung Scholarship.

W.C.C. and J.d.-H. contributed equally to this work.

-
- [1] I. Bloch, J. Dalibard, and W. Zwerger, *Rev. Mod. Phys.* **80**, 885 (2008).
- [2] L.-M. Duan, E. Demler, and M. D. Lukin, *Phys. Rev. Lett.* **91**, 090402 (2003).
- [3] A. B. Kuklov and B. V. Svistunov, *Phys. Rev. Lett.* **90**, 100401 (2003).
- [4] A. Mazurenko, C. S. Chiu, G. Ji, M. F. Parsons, M. Kanász-Nagy, R. Schmidt, F. Grusdt, E. Demler, D. Greiff, and M. Greiner, *Nature (London)* **545**, 462 (2017).
- [5] P. N. Jepsen, J. Amato-Grill, I. Dimitrova, W. W. Ho, E. Demler, and W. Ketterle, *Nature (London)* **588**, 403 (2020).
- [6] A. de Paz, A. Sharma, A. Chotia, E. Maréchal, J. H. Huckans, P. Pedri, L. Santos, O. Gorceix, L. Vernac, and B. Laburthe-Tolra, *Phys. Rev. Lett.* **111**, 185305 (2013).
- [7] M. Kitagawa and M. Ueda, *Phys. Rev. A* **47**, 5138 (1993).
- [8] Y. Li, M. R. Bakhtiari, L. He, and W. Hofstetter, *Phys. Rev. B* **84**, 144411 (2011).
- [9] Y. Li, L. He, and W. Hofstetter, *Phys. Rev. A* **93**, 033622 (2016).
- [10] E. Altman, W. Hofstetter, E. Demler, and M. D. Lukin, *New J. Phys.* **5**, 113 (2003).
- [11] J. Schachenmayer, D. M. Weld, H. Miyake, G. A. Siviloglou, W. Ketterle, and A. J. Daley, *Phys. Rev. A* **92**, 041602(R) (2015).
- [12] F. D. M. Haldane, *Phys. Lett.* **93A**, 464 (1983).
- [13] F. D. M. Haldane, *Phys. Rev. Lett.* **50**, 1153 (1983).
- [14] F. D. M. Haldane, *Rev. Mod. Phys.* **89**, 040502 (2017).
- [15] N. D. Mermin and H. Wagner, *Phys. Rev. Lett.* **17**, 1133 (1966).
- [16] J. Strečka, D. Ján, and L. Čanová, *Chin. J. Phys.* **46**, 329 (2008), <https://www.ps-taiwan.org/cjp/issues.php?vol=46#3>.
- [17] J. P. Renard, M. Verdaguer, L. P. Regnault, W. A. C. Erkelens, J. Rossat-Mignod, and W. G. Stirling, *Europhys. Lett.* **3**, 945 (1987).
- [18] P. Chauhan, F. Mahmood, H. J. Changlani, S. M. Koohpayeh, and N. P. Armitage, *Phys. Rev. Lett.* **124**, 037203 (2020).
- [19] C. Senko, P. Richerme, J. Smith, A. Lee, I. Cohen, A. Retzker, and C. Monroe, *Phys. Rev. X* **5**, 021026 (2015).
- [20] See Supplemental Material at <http://link.aps.org/supplemental/10.1103/PhysRevLett.126.163203> for the calculation of D and J values, the confinement parameters, the details of state preparation and doublon measurement, the derivation of the two-site model, and a description of our matrix-product state simulations, with Refs. [21–27] therein.
- [21] N. Marzari and D. Vanderbilt, *Phys. Rev. B* **56**, 12847 (1997).
- [22] W. Kohn, *Phys. Rev.* **115**, 809 (1959).
- [23] P. Cheinet, S. Trotzky, M. Feld, U. Schnorrberger, M. Moreno-Cardoner, S. Fölling, and I. Bloch, *Phys. Rev. Lett.* **101**, 090404 (2008).
- [24] G. K. Campbell, J. Mun, M. Boyd, P. Medley, A. E. Leanhardt, L. G. Marcassa, D. E. Pritchard, and W. Ketterle, *Science* **313**, 649 (2006).
- [25] D. M. Stamper-Kurn and M. Ueda, *Rev. Mod. Phys.* **85**, 1191 (2013).
- [26] J. Hauschild and F. Pollmann, *SciPost Phys. Lect. Notes* **5** (2018).
- [27] G. Vidal, *Phys. Rev. Lett.* **93**, 040502 (2004).
- [28] A. M. Kaufman, R. P. Anderson, T. M. Hanna, E. Tiesinga, P. S. Julienne, and D. S. Hall, *Phys. Rev. A* **80**, 050701(R) (2009).
- [29] J. M. Deutsch, *Rep. Prog. Phys.* **81**, 082001 (2018).
- [30] I. Morera, A. Polls, and B. Juliá-Díaz, *Sci. Rep.* **9**, 9424 (2019).
- [31] A. Venegas-Gomez, J. Schachenmayer, A. S. Buyskikh, W. Ketterle, M. L. Chiofalo, and A. J. Daley, *Quantum Sci. Technol.* **5**, 045013 (2020).
- [32] I. Dimitrova, N. Jepsen, A. Buyskikh, A. Venegas-Gomez, J. Amato-Grill, A. Daley, and W. Ketterle, *Phys. Rev. Lett.* **124**, 043204 (2020).
- [33] H. Sun, B. Yang, H.-Y. Wang, Z.-Y. Zhou, G.-X. Su, H.-N. Dai, Z.-S. Yuan, and J.-W. Pan, [arXiv:2009.01426](https://arxiv.org/abs/2009.01426).
- [34] A. Venegas-Gomez, A. S. Buyskikh, J. Schachenmayer, W. Ketterle, and A. J. Daley, *Phys. Rev. A* **102**, 023321 (2020).
- [35] C. Gong, L. Li, Z. Li, H. Ji, A. Stern, Y. Xia, T. Cao, W. Bao, C. Wang, Y. Wang *et al.*, *Nature (London)* **546**, 265 (2017).
- [36] C. Xu, J. Feng, H. Xiang, and L. Bellaïche, *npj Comput. Mater.* **4**, 57 (2018).
- [37] D. Dai, H. Xiang, and M.-H. Whangbo, *J. Comput. Chem.* **29**, 2187 (2008).

Supplemental Material for Tunable Single-Ion Anisotropy in Spin-1 Models Realized with Ultracold Atoms

Woo Chang Chung,* Julius de Hond,* Jingtang Xiang (项晶罡), Enid Cruz-Colón, and Wolfgang Ketterle
Research Laboratory of Electronics, MIT-Harvard Center for Ultracold Atoms, Department of Physics,
Massachusetts Institute of Technology, Cambridge, Massachusetts 02139, USA

(Dated: March 19, 2021)

Calculation of D and J

The superexchange parameter J and single-ion anisotropy D were calculated using maximally localized Wannier functions for a simply cubic lattice [S1, S2] and the scattering lengths in Table I.

The sign of D is important for the qualitative behavior. Of the $F = 1$ states, the only combination with $D < 0$ is that of the $|1, -1\rangle$ and $|1, 1\rangle$ states. Any pair involving the $|1, 0\rangle$ state has a positive value of D ; we chose the $|1, -1\rangle$ and $|1, 0\rangle$ combination because it was the easiest to prepare from the initial $|1, -1\rangle$ state. As mentioned in the main text, the value of D is proportional to the various onsite interactions, which have a linear dependence on the scattering lengths. This means that $D \propto (a_{aa} + a_{bb})/2 - a_{ab}$ which equals $-0.93a_0$ and $0.23a_0$ for the two chosen pairs. Through the Wannier functions, D and J depend on the lattice depth, which dependence is shown in Fig. S1.

Confinement parameters

The three-dimensional lattice is created by retro-reflecting three 1064-nm wavelength laser beams. The two horizontal beams have Gaussian beam waists of $150 \mu\text{m}$, while the vertical lattice beam has a waist of $270 \mu\text{m}$. During the entire experiment the atoms are being held in a crossed-beam optical dipole trap. This consists of a vertical beam (which has isotropic trap frequencies of $2\pi \times 24 \text{ Hz}$) intersecting a highly elongated horizontal beam that is at a 45° angle with respect to the horizontal lattices. The latter primarily serves to hold the atoms against gravity, and it has trap frequencies of $2\pi \times 13 \text{ Hz}$ and $2\pi \times 130 \text{ Hz}$ along its horizontal and vertical axes, respectively.

Using these parameters, we were able to calculate the occupation statistics of the Mott insulator, and obtained plateau fractions analogous to those presented in Ref. [S3]. We desire a large $\nu = 2$ Mott insulator plateau, while avoiding any population in the $\nu = 3$ shell as that would interfere with the doublon measurements. Occasionally, we have monitored the population in the different shells using clock-shift spectroscopy [S4]. On a day-to-day basis, however, we use the total atom number or the doublon fraction as indicators (note that our doublon detection scheme detects all the atoms on sites

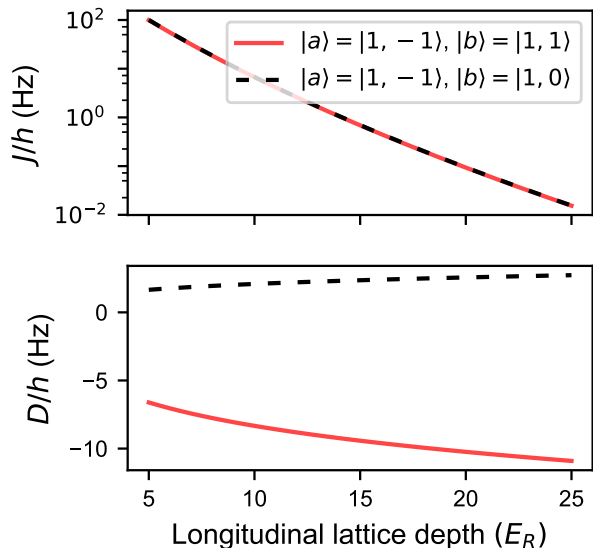


FIG. S1. Values of D and J as a function of longitudinal lattice depth. The results are based on the scattering lengths given in Table I, and assume transverse lattice depths of $35 E_r$.

	$ 1, -1\rangle$	$ 1, 0\rangle$	$ 1, 1\rangle$
$ 1, -1\rangle$	100.4	100.4	101.333
$ 1, 0\rangle$		100.867	100.4
$ 1, 1\rangle$			100.4

TABLE I. Scattering lengths in units of a_0 calculated using the values tabulated in Ref. [S5].

with $\nu \geq 2$). To be safe, the doublon fraction is kept below 0.5, and the atom number below 40×10^3 ; for these parameters the population in $\nu = 3$ should be negligible.

State preparation & doublon measurement

The initial state is prepared by a diabatic Landau-Zener sweep from the initial $|1, -1\rangle$ state to the $|2, 0\rangle$ state. The sweep parameters are set in such a way that we robustly create an equal superposition of the two states. Depending on whether we want to probe positive or negative D/J we either transfer the population fraction in $|2, 0\rangle$ to $|1, 0\rangle$ using a π pulse (which has small

sensitivity to magnetic-field fluctuations), or to $|1, 1\rangle$ using an adiabatic Landau–Zener sweep.

As described in the main text, the doublon statistics are derived from three separate measurements of the atom number, two of them after inducing selective losses that depend on the doublon type. To measure the total doublon fraction, all doublons are removed, regardless of their internal states. Dipolar relaxation is too slow, so a Feshbach resonance between the $|1, 1\rangle$ and $|2, 0\rangle$ states can be used. For this, the $|1, -1\rangle$ component of the pair is transferred to the $|2, 0\rangle$ state using a Landau–Zener sweep, while the other pair component is left in or put into the $|1, 1\rangle$ state. The pairs are removed by modulating the magnetic bias field by ~ 10 mG (peak-to-peak) at 300 Hz around the narrow Feshbach resonance at 9.045 G [S6]. Since the composition of the pairs we want to remove is arbitrary (they can be either $|aa\rangle$, $|ab\rangle$, or $|bb\rangle$), we continuously employ a diabatic Landau–Zener sweep that transfers the atoms back and forth between the $|2, 0\rangle$ and $|1, 1\rangle$ states during the bias modulation, to make sure any doublon spends some time in the Feshbach pair state in order to be removed. In practice, a removal time of 80 ms is sufficient.

In order to specifically remove *paired* doublons (i.e. those of the $|ab\rangle$ type), we transfer the $|1, -1\rangle$ component of the pair to the $|2, -2\rangle$ state, and ensure that the other component is in the $|1, 1\rangle$ state. To remove these pairs, the bias field is modulated by ~ 10 mG (peak-to-peak) at 300 Hz around the 9.092 G Feshbach resonance between the $|1, 1\rangle$ and $|2, -2\rangle$ states [S6].

For both removal steps, the sweep range is a few times the resonance width [S6]. This makes the process insensitive to small field fluctuations.

Two-site model

In the limit of two sites, the spin Hamiltonian (1) reduces to

$$\mathcal{H} = -JS_1 \cdot S_2 + D \left[(S_1^z)^2 + (S_2^z)^2 \right]. \quad (1)$$

The initial state is a product state between site 1 and site 2: $|\Psi\rangle = |\psi\rangle_1 \otimes |\psi\rangle_2$, where the single-site state is given by:

$$\begin{aligned} |\psi\rangle &= \left(\frac{|a\rangle - i|b\rangle}{\sqrt{2}} \right)_{\text{atom 1}} \otimes \left(\frac{|a\rangle - i|b\rangle}{\sqrt{2}} \right)_{\text{atom 2}} \\ &= \frac{1}{2} \left(|1\rangle - i\sqrt{2}|0\rangle - |-1\rangle \right) \end{aligned} \quad (2)$$

The full Hilbert space describing the two spin-1 sites is nine-dimensional. However, the Hamiltonian is block diagonal in the total spin projection, $S_1^z + S_2^z$, and also with regard to odd and even symmetry between the two sites. For the state prepared initially, all the dynamics takes

place in the symmetric $S_1^z + S_2^z = 0$ subspace, which contains only two states: $\{(|1, -1\rangle + |-1, 1\rangle)/\sqrt{2}, |0, 0\rangle\}$. The Hamiltonian is given by

$$\mathcal{H} = \begin{pmatrix} J + 2D & -\sqrt{2}J \\ -\sqrt{2}J & 0 \end{pmatrix}. \quad (3)$$

The projection of the initial state into this subspace is

$$|\psi\rangle = \sqrt{\frac{1}{6}} (|1, -1\rangle + |-1, 1\rangle) + \sqrt{\frac{2}{3}} |0, 0\rangle, \quad (4)$$

also see Fig. 3. Since the $|0, 0\rangle$ state has $(S_i^z)^2 = 0$, and the $(|1, -1\rangle + |-1, 1\rangle)/\sqrt{2}$ has $(S_i^z)^2 = 1$, a Rabi oscillation between them leads to an oscillation of the spin alignment A . Note that the components of the initial state in other subspaces contribute a constant value to A .

Inspection of the Hamiltonian (3) identifies $J + 2D$ as a z field, which is added to an x field equal to $\sqrt{2}J$. In a deep lattice with $J \sim 0$, the field is parallel to the z axis, but lowering the lattice adds an x field, which tilts the field vector and initiates a precession of the state vector around it (see Fig. 3).

The Rabi frequency of this oscillation is given by

$$\Omega = \sqrt{9J^2 + 4JD + 4D^2}/\hbar, \quad (5)$$

while the peak-to-peak amplitude of the oscillation in A is $6JD/\Omega^2$, which is maximized for $|D/J| = 3/2$.

Matrix-product state simulations

We implemented the time-evolution block decimation algorithm for matrix-product states (MPS-TEBD) [S7, S8] on 100 sites, using a maximum bond dimension χ of 20. This was found to give results consistent with published data [S9]. The modest bond dimension is sufficient because the transient behavior in A occurs within a few exchange times (\hbar/J), during which correlations only build up between clusters of sites. This has the additional benefit that the calculation can be run on a desktop computer.

The simulated evolution of the spin alignment A as a function of lattice depth is shown in Fig. S2. These results form the basis of the simulations presented in the main text. Comparing to the two-site model, we observe that the early time behavior is dominated by nearest-neighbor physics. Specifically, the first minima seen in Fig. S2 occur at the period of the Rabi oscillation given in Eq. (5) divided by $\sqrt{2}$ to account for the fact that a site in the chain has not one but two neighbors.

This also allows us to understand the choice of hold times in Fig. 2 as $\pi/\sqrt{2}\Omega$ at the lattice depth where $|D/J| \sim 3/2$. This number equals 67 and 17 ms for the positive and negative D/J pair, respectively, while the

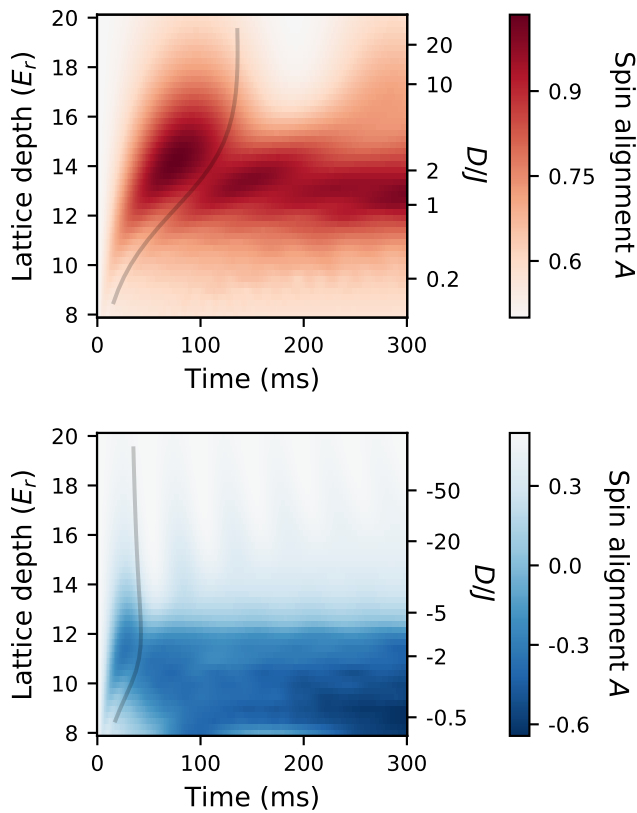


FIG. S2. Time evolution of the spin alignment A for various lattice depths, calculated using the TEBD algorithm for matrix-product states. The top and bottom figures are calculated for pairs with positive ($|1, -1\rangle$ and $|1, 0\rangle$) and negative ($|1, -1\rangle$ and $|1, 1\rangle$) values of D/J , respectively. The solid lines indicate the inverse (lattice depth dependent) Rabi frequency of Eq. (5) times $\pi\sqrt{2}$, showing that the initial behavior is dictated by nearest neighbors.

actual values we use are 70 and 25 ms. It can be thought of as half a Rabi oscillation to ensure the largest possible contrast in the signal.

Finally, we investigate the entanglement properties of the spin chain in greater detail. See Fig. S3 for the von Neumann entropy calculated for both long ($L = 100$) spin chains using MPS-TEBD, and shorter ones that can be solved exactly. The von Neumann entropy is evaluated between the equally long left and right halves of the chain. Both calculations show an initial linear growth in entanglement entropy, which implies that the bond dimension required to accurately capture the evolution grows exponentially. Naturally, this leads to convergence issues after a few exchange times. Note, though, that the initial growth rate is independent of system size.

Physically, if the chain contains an even number of sites, the maximum entanglement entropy between the two halves, in units of k_B , is given by $\ln(3^{L/2})$. In the case of the MPS simulations this will be artificially

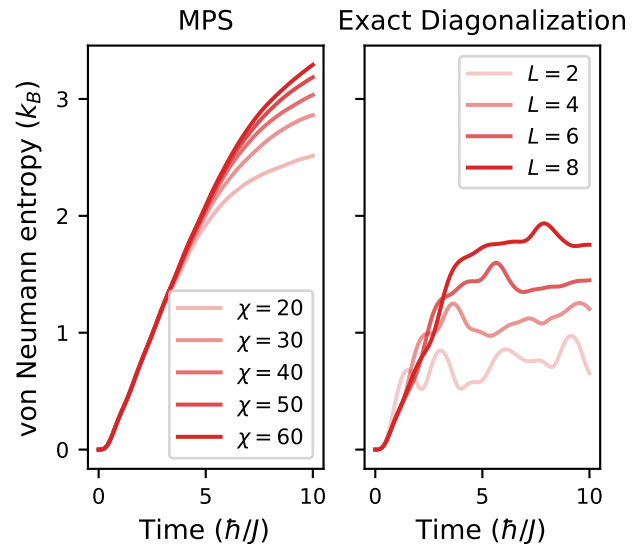


FIG. S3. Comparison of the von Neumann entanglement entropy between matrix product state calculations on $L = 100$ sites for varying bond dimension χ (left), and exact diagonalization for varying chain length (right); both calculated for $D/J = 1$. Note that the bond dimensions in the MPS calculations are not sufficiently large to capture the full entanglement at long evolution times, indicated by a lack of convergence there.

bounded, because an MPS with a maximum bond dimension of χ can only represent states with a maximal entanglement entropy of $\ln(\chi)$. Nevertheless, the simulation is expected to provide an accurate result for the first few exchange times \hbar/J .

-
- * These authors contributed equally to this work.
- [S1] N. Marzari and D. Vanderbilt, Phys. Rev. B **56**, 12847 (1997).
- [S2] W. Kohn, Physical Review **115**, 809 (1959).
- [S3] P. Cheinet, S. Trotzky, M. Feld, U. Schnorrberger, M. Moreno-Cardoner, S. Fölling, and I. Bloch, Phys. Rev. Lett. **101**, 090404 (2008).
- [S4] G. K. Campbell, J. Mun, M. Boyd, P. Medley, A. E. Leanhardt, L. G. Marcassa, D. E. Pritchard, and W. Ketterle, Science **313**, 649 (2006).
- [S5] D. M. Stamper-Kurn and M. Ueda, Reviews of Modern Physics **85**, 1191 (2013).
- [S6] A. M. Kaufman, R. P. Anderson, T. M. Hanna, E. Tiesinga, P. S. Julienne, and D. S. Hall, Phys. Rev. A **80**, 050701(R) (2009).
- [S7] J. Hauschild and F. Pollmann, SciPost Physics Lecture Notes , 5 (2018).
- [S8] G. Vidal, Phys. Rev. Lett. **93**, 040502 (2004).
- [S9] A. Venegas-Gomez, A. S. Buyskikh, J. Schachenmayer, W. Ketterle, and A. J. Daley, Phys. Rev. A **102**, 023321 (2020).

Appendix C

Calculation of the effective spin-1 model parameters

In this appendix we show that the effective spin-1 model for a $\langle \hat{n} \rangle = 2$ bosonic Mott insulator contains an exchange anisotropy as well as an on-site anisotropy (single-ion anisotropy). We make use of a computer algebra system (Mathematica) to derive the main results.

The spin model does not contain any anisotropy when $U_{aa} = U_{bb} = U_{ab}$ and $t_a = t_b$. We track the appearance of anisotropies by defining the following variables [97]:

$$\begin{aligned}\frac{1}{U} &= \frac{1}{2} \left(\frac{1}{U_{aa}} + \frac{1}{U_{bb}} \right) \\ d &= (U_{aa} + U_{bb})/2 - U_{ab} \\ \delta &= \frac{U_{aa} - U_{bb}}{U_{aa} + U_{bb}}\end{aligned}$$

With these variables, the spin-dependent interaction energies can be re-expressed as follows:

$$\begin{aligned}U_{aa} &= \frac{U}{1 - \delta} \\ U_{bb} &= \frac{U}{1 + \delta} \\ U_{ab} &= \frac{d\delta^2 - d + U}{1 - \delta^2}\end{aligned}$$

We also denote by z the number of nearest neighbors. While Eq. 6.2 expresses the matrix element equivalence between a N -site Bose-Hubbard model and a N -site spin-1 model, we can reduce the equivalence to that between a two-site Bose-Hubbard model and a two-site spin-1 model, because all the interactions only involve nearest-neighbors. The total interaction energy is just the sum of interaction energies found in all possible two-site pairs within the given many-body state, so it suffices to simply track distinct two-site pairs. However, during this reduction we have to be careful to avoid double-counting of single-body terms such as the energy offset or the fictitious bias field, so such terms need to be divided by z . For example, consider the equation for two neighboring $|S_z = 1\rangle$ (first row in Fig. 6-3). The equation is written as

$$\frac{U_{aa}}{z_1} + \frac{U_{aa}}{z_2} - \frac{12t^2}{U_{aa}} + \frac{c}{z_1} + \frac{c}{z_2} = J_z - \frac{h_z}{z_1} - \frac{h_z}{z_2} \quad (\text{C.1})$$

To check the validity of this example, consider a three-site chain filled with $|S_z = 1\rangle$. The corresponding equation is

$$3U_{aa} - \frac{24t^2}{U_{aa}} + 3c = 2J_z - 3h_z$$

Since the value of z is 1,2,1 for the three sites, we see that summing up Eq. C.1 twice (the number of links in the chain) with $(z_1, z_2) = (1, 2)$ and $(z_2, z_3) = (2, 1)$ returns the correct total energy for the three-site chain. For the remainder of the calculation we assume $z_1 = z_2$. The solution (or the least-square solution) to the system of linear equations is searched with the attached Mathematica code.

System of Linear Equations

```

In[383]:= With[{order = 1},
  Clear[c, hz, Jz, Jp, SIA];
  eq1 =
    (Series[2  $\frac{U}{1-\delta}$  - z  $\frac{12 t^2}{U}$  (1 -  $\delta$ ) + 2 c, { $\delta$ , 0, order}] // Normal) == z Jz - 2 hz + 2 SIA;
  eq2 = (Series[2 ( $\frac{d-U-d \delta^2}{-1+\delta^2}$ ) - z (4  $\frac{t^2}{U}$  (1 -  $\delta$ ) + 4  $\frac{t^2}{U}$  (1 +  $\delta$ )) + 2 c,
    { $\delta$ , 0, order}, {d, 0, 1}] // Normal) == 0;
  eq3 = (Series[2  $\frac{U}{1+\delta}$  - z  $\frac{12 t^2}{U}$  (1 +  $\delta$ ) + 2 c, { $\delta$ , 0, order}] // Normal) == z Jz + 2 hz + 2 SIA;
  eq4 = (Series[ $\frac{U}{1-\delta}$  + ( $\frac{d-U-d \delta^2}{-1+\delta^2}$ ) - z ( $\frac{3 t^2}{2 \frac{U}{1-\delta} - (\frac{d-U-d \delta^2}{-1+\delta^2})} + \frac{5 t^2}{(\frac{d-U-d \delta^2}{-1+\delta^2})}$ ) + 2 c,
    { $\delta$ , 0, order}, {d, 0, order}] // Normal) == -hz + SIA;
  eq5 = (Series[ $\frac{U}{1+\delta}$  + ( $\frac{d-U-d \delta^2}{-1+\delta^2}$ ) - z ( $\frac{3 t^2}{2 \frac{U}{1+\delta} - (\frac{d-U-d \delta^2}{-1+\delta^2})} + \frac{5 t^2}{(\frac{d-U-d \delta^2}{-1+\delta^2})}$ ) + 2 c,
    { $\delta$ , 0, order}, {d, 0, order}] // Normal) == hz + SIA;
  eq6 = (Series[ $\frac{U}{1-\delta}$  +  $\frac{U}{1+\delta}$  - z ( $\frac{2 t^2}{2 (\frac{d-U-d \delta^2}{-1+\delta^2}) - \frac{U}{1-\delta}} + \frac{2 t^2}{2 (\frac{d-U-d \delta^2}{-1+\delta^2}) - \frac{U}{1+\delta}}$ ) + 2 c,
    { $\delta$ , 0, order}, {d, 0, order}] // Normal) == -z Jz + 2 SIA;
  eq7and8 = (Series[- $\frac{4 t^2}{(\frac{d-U-d \delta^2}{-1+\delta^2})}$ , { $\delta$ , 0, order}, {d, 0, order}] // Normal) == Jp;
  eq9 = (Series[t^2 ( $\frac{1}{\frac{U}{1+\delta} - 2 (\frac{d-U-d \delta^2}{-1+\delta^2})} + \frac{1}{-\frac{U}{1-\delta}} + \frac{1}{\frac{U}{1-\delta} - 2 (\frac{d-U-d \delta^2}{-1+\delta^2})} + \frac{1}{-\frac{U}{1+\delta}}$ ),

```

```

      {δ, 0, order}, {d, 0, order}] // Normal) == Jp;

Print[Reduce[{eq7and8, eq9}, {Jp}, Reals] // Simplify[#, Assumptions → {U ≠ 0}] &];
Reduce[{eq1, eq2, eq3, eq4, eq5, eq6} // Evaluate, {SIA, Jz, hz, c}, Reals] //
  Simplify[#, Assumptions → {t > 0, U > 0, δ ≠ 0, z > 0}] & // Reduce //
  FullSimplify[#, Assumptions → {SIA ≠ 0}] &]

Jp == -  $\frac{4 t^2 (d + U)}{U^2}$ 
Out[383]= False

```

Approximate Solution to an overdetermined system

The equations for the diagonal elements constitute an overdetermined system.

If we express our system of linear equations as $A \vec{x} = \vec{b}$ and A is not invertible, then we can obtain an approximate solution by minimizing $\|A \vec{x} - \vec{b}\|^2$ (least-square solution). Let's assume the solution vector \vec{x} represents (c, h_z, J_z, SIA) .

If $(A^T A)^{-1}$ is nonsingular, then the pseudoinverse of A is $(A^T A)^{-1} A^T$.

```

In[ ]:= Clear[c, hz, Jz, SIA]
sys = ({#1, Coefficient[#2, {c, hz, Jz, SIA}]} & @@ AddSides[#, -2 c]) & /@
  {eq1, eq2, eq3, eq4, eq5, eq6};
A = sys[[;;, 2]];
b = sys[[;;, 1]];

```

```

In[ ]:= PseudoInverse[A] // MatrixForm

```

```

Out[ ]//MatrixForm=

$$\begin{pmatrix} \frac{1}{27} & -\frac{19}{54} & \frac{1}{27} & -\frac{4}{27} & -\frac{4}{27} & \frac{2}{27} \\ -\frac{1}{5} & 0 & \frac{1}{5} & -\frac{1}{10} & \frac{1}{10} & 0 \\ \frac{7}{27z} & \frac{1}{27z} & \frac{7}{27z} & -\frac{1}{27z} & -\frac{1}{27z} & -\frac{13}{27z} \\ \frac{4}{27} & -\frac{11}{27} & \frac{4}{27} & -\frac{5}{54} & -\frac{5}{54} & \frac{8}{27} \end{pmatrix}$$


```

```

In[ ]:= {c, hz, Jz, SIA} = PseudoInverse[A].b // FullSimplify // Expand

```

```

Out[ ]:=  $\left\{ d - U + \frac{4 t^2 z}{U}, -U \delta + \frac{12 d t^2 z \delta}{5 U^2} - \frac{6 t^2 z \delta}{U}, \frac{4 d t^2}{U^2} - \frac{4 t^2}{U}, d - \frac{2 d t^2 z}{U^2} \right\}$ 

```

We can check the deviation of the true Hamiltonian from the spin model by feeding the solution above back into the linear set of equations and inspecting the leftover on the LHS of the equations.

```

In[ ]:= Map[({#[1] - #[2]}) &, {eq1, eq2, eq3, eq4, eq5, eq6}] // FullSimplify

```

```

Out[ ]:=  $\left\{ \frac{24 d t^2 z \delta}{5 U^2}, 0, -\frac{24 d t^2 z \delta}{5 U^2}, -\frac{48 d t^2 z \delta}{5 U^2}, \frac{48 d t^2 z \delta}{5 U^2}, 0 \right\}$ 

```

Appendix D

Spherical tensor identities

In this appendix, we review important definitions and identities related to the algebra of spherical tensors. Explicit expressions for $\alpha_J^{(k)}$ and $\alpha_F^{(k)}$ defined in Eq. 3.4 are provided. For a general introduction to spherical tensors, we refer to Ref. [46].

D.1 Spherical basis

With respect to the Cartesian basis defined by unit vectors $\mathbf{e}_x, \mathbf{e}_y, \mathbf{e}_z$, the spherical basis vectors can be written as

$$\begin{aligned}\mathbf{e}_{\pm 1} &= \mp \frac{\mathbf{e}_x \pm i\mathbf{e}_y}{\sqrt{2}} \\ \mathbf{e}_0 &= \mathbf{e}_z\end{aligned}$$

In the spherical basis, the scalar product $\mathbf{A} \cdot \mathbf{B}$ between two vectors \mathbf{A} and \mathbf{B} is defined as

$$\mathbf{A} \cdot \mathbf{B} = \sum_q A_q B_q^* = \sum_q (-1)^q A_q B_{-q}$$

where the vector components A_q are defined as $\mathbf{A} \cdot \mathbf{e}_q$ and similarly for B_q . This means the vector \mathbf{A} is expressed as $\sum_q A_q \mathbf{e}_q^*$.

For rank- k spherical tensors $A^{(k)}$ and $B^{(k)}$, the scalar product is expressed as

$$A^{(k)} \cdot B^{(k)} = \sum_{q=-k}^k (-1)^q A_q^{(k)} B_{-q}^{(k)} \quad (\text{D.1})$$

If two spherical tensor operators $P^{(k_1)}$ and $Q^{(k_2)}$ commute, we can derive a useful identity. For the purpose of the derivation, denote the Clebsch-Gordan (CG) coefficient $\langle k_1, q_1; k_2, q_2 | kq \rangle$ by $C_{k_1 q_1, k_2 q_2}^{kq}$. The CG coefficients satisfy an orthogonality relation:

$$\sum_{k=|k_1-k_2|}^{k_1+k_2} \sum_{q=-k}^k C_{k_1 q_1, k_2 q_2}^{kq} C_{k_1 q'_1, k_2 q'_2}^{kq} = \delta_{q_1, q'_1} \delta_{q_2, q'_2}$$

and they also satisfy the following permutation relation:

$$C_{k_1 q_1, k_2, q_2}^{kq} = (-1)^{k_1+k_2-k} C_{k_1(-q_1), k_2, (-q_2)}^{k(-q)}$$

Now consider the expression $(P^{(k_1)} \cdot Q^{(k_1)}) (R^{(k_2)} \cdot S^{(k_2)})$, where Q and R commute as mentioned. We use Eq. D.1 and the two aforementioned properties of CG coefficients:

$$\begin{aligned} & (P^{(k_1)} \cdot Q^{(k_1)}) (R^{(k_2)} \cdot S^{(k_2)}) = \sum_{q_1, q_2} (-1)^{q_1+q_2} P_{q_1}^{(k_1)} R_{q_2}^{(k_2)} Q_{-q_1}^{(k_1)} S_{-q_2}^{(k_2)} \\ &= \sum_{q_1, q_2, q_3, q_4} (-1)^{q_1+q_2} P_{q_1}^{(k_1)} R_{q_2}^{(k_2)} Q_{-q_3}^{(k_1)} S_{-q_4}^{(k_2)} \delta_{q_1, q_3} \delta_{q_1, q_4} \\ &= \sum_{k=|k_1-k_2|}^{k_1+k_2} \sum_{q=-k}^k \sum_{q_1, q_2, q_3, q_4} (-1)^{q_1+q_2} \left(P_{q_1}^{(k_1)} R_{q_2}^{(k_2)} C_{k_1 q_1, k_2 q_2}^{kq} \right) \left(Q_{-q_3}^{(k_1)} S_{-q_4}^{(k_2)} C_{k_1 q_3, k_2 q_4}^{kq} \right) \\ &= \sum_{k=|k_1-k_2|}^{k_1+k_2} (-1)^{k_1+k_2-k} \sum_{q=-k}^k \sum_{q_1, q_2} (-1)^{q_1+q_2} \left(P_{q_1}^{(k_1)} R_{q_2}^{(k_2)} C_{k_1 q_1, k_2 q_2}^{kq} \right) \\ &\times \sum_{q_3, q_4} \left(Q_{-q_3}^{(k_1)} S_{-q_4}^{(k_2)} C_{k_1(-q_3), k_2(-q_4)}^{k(-q)} \right) \\ &= \sum_{k=|k_1-k_2|}^{k_1+k_2} (-1)^{k_1+k_2-k} \sum_{q=-k}^k (-1)^q (P^{(k_1)} \otimes R^{(k_2)})_q^{(k)} (Q^{(k_1)} \otimes S^{(k_2)})_{-q}^{(k)} \\ &= \sum_{k=|k_1-k_2|}^{k_1+k_2} (-1)^{k_1+k_2-k} (P^{(k_1)} \otimes R^{(k_2)})^{(k)} \cdot (Q^{(k_1)} \otimes S^{(k_2)})^{(k)} \quad (\text{D.2}) \end{aligned}$$

This result is used in the derivation of $\alpha_J^{(k)} = \langle J \| \{ \mathbf{d} \otimes (R_+ + (-1)^k R_-) \mathbf{d} \}^{(k)} \| J \rangle$ in Sec. 3.3.

D.2 Reduced matrix element

A common source of confusion is the different conventions being used for the definition of the reduced matrix. In this thesis, the reduced matrix element is defined such that the Wigner-Eckart theorem is expressed as

$$\langle J, m_J | T_q^{(k)} | J', m'_J \rangle = (-1)^{2k} \langle J \| T^{(k)} \| J' \rangle \langle J, m_J | J', m'_J; k, q \rangle$$

This is also the convention used in Refs. [33, 46]. On the other hand, a common alternative convention, used by Refs. [25, 116], is

$$\begin{aligned} \langle J, m_J | T_q^{(k)} | J', m'_J \rangle &= \frac{(-1)^{2k}}{\sqrt{2J+1}} \langle J \| T^{(k)} \| J' \rangle \langle J, m_J | J', m'_J; k, q \rangle \\ &= (-1)^{J-m_J} \begin{pmatrix} J & k & J' \\ -m_J & q & m_{J'} \end{pmatrix} \langle J \| T^{(k)} \| J' \rangle \end{aligned}$$

where (...) is the Wigner 3- j symbol. The advantage of this convention is that the Wigner 3- j symbol has convenient permutation relations. However, depending on the familiarity with such relations, the presentation of the Wigner-Eckart theorem by the second convention may seem less clear. Hence we use the first convention.

D.3 Polarizability

Here we provide the full expression for $\alpha_J^{(k)}$. In the summation over the angular momentum of the excited states J' , we explicitly specify the remaining set of quantum numbers n' that fully describes the excited states. The formula can be obtained by

simplifying Eq. (5.5) in Ref. [46]:

$$\alpha_{n,J}^{(k)} = \sqrt{2k+1}\sqrt{2J+1} \sum_{n',J'} (-1)^{k+J+J'} \left\{ \begin{matrix} 1 & k & 1 \\ J & J' & J \end{matrix} \right\} |\langle n, J \| \mathbf{d} \| n', J' \rangle|^2 \\ \times \left(\frac{1}{E_{n,J} - E_{n',J'} + \hbar\omega} + \frac{(-1)^k}{E_{n,J} - E_{n',J'} - \hbar\omega} \right)$$

The symbol $\{\dots\}$ is the Wigner 6- j symbol. Tabulated values of $\langle n, J \| \mathbf{d} \| n', J' \rangle$ for alkali atoms can be found in e.g. Ref. [33].

For the computation of polarizabilities for hyperfine states $|F(J, I), m_F\rangle$, we must use $\alpha_F^{(k)}$, which depends on $\alpha_J^{(k)}$. The formula for $\alpha_F^{(k)}$ can be obtained by simplifying Eq. (5.9) in Ref. [46]:

$$\alpha_{F(J,I)}^{(k)} = (-1)^{F+J+I+k} \sqrt{2J+1}\sqrt{2F+1} \left\{ \begin{matrix} F & k & F \\ J & I & J \end{matrix} \right\} \alpha_J^{(k)}$$

Bibliography

- [1] M. H. Anderson, J. R. Ensher, M. R. Matthews, C. E. Wieman, and E. A. Cornell, “Observation of Bose-Einstein condensation in a dilute atomic vapor,” *Science*, vol. 269, no. 5221, pp. 198–201, 1995.
- [2] K. B. Davis, M. O. Mewes, M. R. Andrews, N. J. van Druten, D. S. Durfee, D. M. Kurn, and W. Ketterle, “Bose-Einstein condensation in a gas of sodium atoms,” *Phys. Rev. Lett.*, vol. 75, pp. 3969–3973, Nov 1995.
- [3] B. DeMarco and D. S. Jin, “Onset of Fermi degeneracy in a trapped atomic gas,” *Science*, vol. 285, no. 5434, pp. 1703–1706, 1999.
- [4] W. Ketterle, D. S. Durfee, and D. Stamper-Kurn, “Making, probing and understanding Bose-Einstein condensates,” *arXiv preprint cond-mat/9904034*, 1999.
- [5] W. Ketterle and M. W. Zwierlein, “Making, probing and understanding ultracold Fermi gases,” *arXiv preprint arXiv:0801.2500*, 2008.
- [6] R. P. Feynman, “Simulating physics with computers,” *International Journal of Theoretical Physics*, vol. 21, pp. 467–488, Jun 1982.
- [7] M. Greiner, O. Mandel, T. Esslinger, T. W. Hänsch, and I. Bloch, “Quantum phase transition from a superfluid to a Mott insulator in a gas of ultracold atoms,” *Nature*, vol. 415, pp. 39–44, Jan 2002.
- [8] W. Heisenberg, “Mehrkörperproblem und resonanz in der quantenmechanik,” *Zeitschrift für Physik*, vol. 38, pp. 411–426, Jun 1926.
- [9] P. A. M. Dirac and R. H. Fowler, “On the theory of quantum mechanics,” *Proceedings of the Royal Society of London. Series A, Containing Papers of a Mathematical and Physical Character*, vol. 112, no. 762, pp. 661–677, 1926.
- [10] S. Sachdev, *Quantum Phase Transitions*. Cambridge University Press, 2 ed., 2011.
- [11] F. Franchini, *An introduction to integrable techniques for one-dimensional quantum systems*. Springer, 2017.
- [12] D. Schneble, Y. Torii, M. Boyd, E. W. Streed, D. E. Pritchard, and W. Ketterle, “The onset of matter-wave amplification in a superradiant Bose-Einstein condensate,” *Science*, vol. 300, no. 5618, pp. 475–478, 2003.

- [13] D. M. Weld, P. Medley, H. Miyake, D. Hucul, D. E. Pritchard, and W. Ketterle, “Spin gradient thermometry for ultracold atoms in optical lattices,” *Phys. Rev. Lett.*, vol. 103, p. 245301, Dec 2009.
- [14] P. Medley, D. M. Weld, H. Miyake, D. E. Pritchard, and W. Ketterle, “Spin gradient demagnetization cooling of ultracold atoms,” *Phys. Rev. Lett.*, vol. 106, p. 195301, May 2011.
- [15] H. Miyake, G. A. Siviloglou, C. J. Kennedy, W. C. Burton, and W. Ketterle, “Realizing the Harper Hamiltonian with laser-assisted tunneling in optical lattices,” *Phys. Rev. Lett.*, vol. 111, p. 185302, Oct 2013.
- [16] C. J. Kennedy, W. C. Burton, W. C. Chung, and W. Ketterle, “Observation of bose–einstein condensation in a strong synthetic magnetic field,” *Nature Physics*, vol. 11, pp. 859–864, Oct 2015.
- [17] W. C. Burton, C. J. Kennedy, W. C. Chung, S. Vadia, W. Chen, and W. Ketterle, “Coherence times of Bose-Einstein condensates beyond the shot-noise limit via superfluid shielding,” *Phys. Rev. Lett.*, vol. 117, p. 275301, Dec 2016.
- [18] C. Kennedy, *Creating Novel Quantum States of Ultracold Bosons in Optical Lattices*. PhD thesis, Massachusetts Institute of Technology, 2017.
- [19] W. C. Burton, *Ultracold Bosons in Optical Lattices for Quantum Measurement and Simulation*. PhD thesis, Massachusetts Institute of Technology, 2019.
- [20] L.-M. Duan, E. Demler, and M. D. Lukin, “Controlling spin exchange interactions of ultracold atoms in optical lattices,” *Phys. Rev. Lett.*, vol. 91, p. 090402, Aug 2003.
- [21] A. B. Kuklov and B. V. Svistunov, “Counterflow superfluidity of two-species ultracold atoms in a commensurate optical lattice,” *Phys. Rev. Lett.*, vol. 90, p. 100401, Mar 2003.
- [22] E. Altman, W. Hofstetter, E. Demler, and M. D. Lukin, “Phase diagram of two-component bosons on an optical lattice,” *New Journal of Physics*, vol. 5, pp. 113–113, sep 2003.
- [23] J. Schachenmayer, D. M. Weld, H. Miyake, G. A. Siviloglou, W. Ketterle, and A. J. Daley, “Adiabatic cooling of bosons in lattices to magnetically ordered quantum states,” *Phys. Rev. A*, vol. 92, p. 041602, Oct 2015.
- [24] W. C. Chung, J. de Hond, J. Xiang, E. Cruz-Colón, and W. Ketterle, “Tunable single-ion anisotropy in spin-1 models realized with ultracold atoms,” *Phys. Rev. Lett.*, vol. 126, p. 163203, Apr 2021.
- [25] K. Beloy, *Theory of the ac Stark effect on the atomic hyperfine structure and applications to microwave atomic clocks*. PhD thesis, University of Nevada, Reno, 2009.

- [26] E. W. Streed, *Rubidium-87 Bose-Einstein condensates: Machine construction and quantum Zeno experiments*. PhD thesis, Massachusetts Institute of Technology, 2006.
- [27] E. W. Streed, A. P. Chikkatur, T. L. Gustavson, M. Boyd, Y. Torii, D. Schneble, G. K. Campbell, D. E. Pritchard, and W. Ketterle, “Large atom number Bose-Einstein condensate machines,” *Review of Scientific Instruments*, vol. 77, no. 2, p. 023106, 2006.
- [28] J. Mun, *Bose-Einstein condensates in optical lattices: The superfluid to Mott insulator phase transition*. PhD thesis, Massachusetts Institute of Technology, 2008.
- [29] M. Fuchs, “Development of a high power stabilized diode laser system,” Master’s thesis, University of Oregon, 6 2006.
- [30] M. L. Harris, C. S. Adams, S. L. Cornish, I. C. McLeod, E. Tarleton, and I. G. Hughes, “Polarization spectroscopy in rubidium and cesium,” *Phys. Rev. A*, vol. 73, p. 062509, Jun 2006.
- [31] M. Walhout, J. Dalibard, S. L. Rolston, and W. D. Phillips, “ $\sigma^+ - \sigma^-$ optical molasses in a longitudinal magnetic field,” *J. Opt. Soc. Am. B*, vol. 9, pp. 1997–2007, Nov 1992.
- [32] B. Merkel, K. Thirumalai, J. E. Tarlton, V. M. Schäfer, C. J. Ballance, T. P. Harty, and D. M. Lucas, “Magnetic field stabilization system for atomic physics experiments,” *Review of Scientific Instruments*, vol. 90, no. 4, p. 044702, 2019.
- [33] D. A. Steck, “Rubidium 87 D line data,” 2001.
- [34] H. J. Metcalf and P. van der Straten, *Laser Cooling and Trapping*. New York: Springer-Verlag, 1999.
- [35] M.-O. Mewes, M. R. Andrews, N. J. van Druten, D. M. Kurn, D. S. Durfee, and W. Ketterle, “Bose-Einstein condensation in a tightly confining dc magnetic trap,” *Phys. Rev. Lett.*, vol. 77, pp. 416–419, Jul 1996.
- [36] Y. Castin and R. Dum, “Bose-Einstein condensates in time dependent traps,” *Phys. Rev. Lett.*, vol. 77, pp. 5315–5319, Dec 1996.
- [37] A. M. Kaufman, B. J. Lester, and C. A. Regal, “Cooling a single atom in an optical tweezer to its quantum ground state,” *Phys. Rev. X*, vol. 2, p. 041014, Nov 2012.
- [38] J. D. Thompson, T. G. Tiecke, A. S. Zibrov, V. Vuletić, and M. D. Lukin, “Coherence and raman sideband cooling of a single atom in an optical tweezer,” *Phys. Rev. Lett.*, vol. 110, p. 133001, Mar 2013.

- [39] R. Mitsch, C. Sayrin, B. Albrecht, P. Schneeweiss, and A. Rauschenbeutel, “Exploiting the local polarization of strongly confined light for sub-micrometer-resolution internal state preparation and manipulation of cold atoms,” *Phys. Rev. A*, vol. 89, p. 063829, Jun 2014.
- [40] O. Mandel, M. Greiner, A. Widera, T. Rom, T. W. Hänsch, and I. Bloch, “Coherent transport of neutral atoms in spin-dependent optical lattice potentials,” *Phys. Rev. Lett.*, vol. 91, p. 010407, Jul 2003.
- [41] B. Yang, H.-N. Dai, H. Sun, A. Reingruber, Z.-S. Yuan, and J.-W. Pan, “Spin-dependent optical superlattice,” *Phys. Rev. A*, vol. 96, p. 011602, Jul 2017.
- [42] C. Robens, J. Zopes, W. Alt, S. Brakhane, D. Meschede, and A. Alberti, “Low-entropy states of neutral atoms in polarization-synthesized optical lattices,” *Phys. Rev. Lett.*, vol. 118, p. 065302, Feb 2017.
- [43] R. Grimm, M. Weidemüller, and Y. B. Ovchinnikov, “Optical dipole traps for neutral atoms,” *Advances in atomic, molecular, and optical physics*, vol. 42, pp. 95–170, 2000.
- [44] S. Eustice, K. Cassella, and D. Stamper-Kurn, “Laser cooling of transition-metal atoms,” *Phys. Rev. A*, vol. 102, p. 053327, Nov 2020.
- [45] R. J. Glauber, “The quantum theory of optical coherence,” *Phys. Rev.*, vol. 130, pp. 2529–2539, Jun 1963.
- [46] D. M. Brink and G. R. Satchler, *Angular Momentum*. London: Clarendon Press, 1994.
- [47] A. Mazurenko, C. S. Chiu, G. Ji, M. F. Parsons, M. Kanász-Nagy, R. Schmidt, F. Grusdt, E. Demler, D. Greif, and M. Greiner, “A cold-atom fermi–hubbard antiferromagnet,” *Nature*, vol. 545, pp. 462–466, May 2017.
- [48] B. J. Bloom, T. L. Nicholson, J. R. Williams, S. L. Campbell, M. Bishof, X. Zhang, W. Zhang, S. L. Bromley, and J. Ye, “An optical lattice clock with accuracy and stability at the 10^{-18} level,” *Nature*, vol. 506, pp. 71–75, Feb 2014.
- [49] I. Bloch, “Ultracold quantum gases in optical lattices,” *Nature Physics*, vol. 1, pp. 23–30, Oct 2005.
- [50] M. Lewenstein, A. Sanpera, V. Ahufinger, B. Damski, A. Sen(De), and U. Sen, “Ultracold atomic gases in optical lattices: mimicking condensed matter physics and beyond,” *Advances in Physics*, vol. 56, no. 2, pp. 243–379, 2007.
- [51] I. Bloch, J. Dalibard, and W. Zwerger, “Many-body physics with ultracold gases,” *Rev. Mod. Phys.*, vol. 80, pp. 885–964, Jul 2008.
- [52] O. Morsch and M. Oberthaler, “Dynamics of Bose-Einstein condensates in optical lattices,” *Rev. Mod. Phys.*, vol. 78, pp. 179–215, Feb 2006.

- [53] P. Jessen and I. Deutsch, “Optical lattices,” vol. 37 of *Advances In Atomic, Molecular, and Optical Physics*, pp. 95–138, Academic Press, 1996.
- [54] A. Heinz, A. J. Park, N. Šantić, J. Trautmann, S. G. Porsev, M. S. Safronova, I. Bloch, and S. Blatt, “State-dependent optical lattices for the strontium optical qubit,” *Phys. Rev. Lett.*, vol. 124, p. 203201, May 2020.
- [55] C. Becker, P. Soltan-Panahi, J. Kronjäger, S. Dörscher, K. Bongs, and K. Senstock, “Ultracold quantum gases in triangular optical lattices,” *New Journal of Physics*, vol. 12, p. 065025, jun 2010.
- [56] K. L. Lee, B. Grémaud, R. Han, B.-G. Englert, and C. Miniatura, “Ultracold fermions in a graphene-type optical lattice,” *Phys. Rev. A*, vol. 80, p. 043411, Oct 2009.
- [57] G.-B. Jo, J. Guzman, C. K. Thomas, P. Hosur, A. Vishwanath, and D. M. Stamper-Kurn, “Ultracold atoms in a tunable optical kagome lattice,” *Phys. Rev. Lett.*, vol. 108, p. 045305, Jan 2012.
- [58] N. W. Ashcroft, N. D. Mermin, *et al.*, “Solid state physics,” 1976.
- [59] N. Marzari, A. A. Mostofi, J. R. Yates, I. Souza, and D. Vanderbilt, “Maximally localized Wannier functions: Theory and applications,” *Rev. Mod. Phys.*, vol. 84, pp. 1419–1475, Oct 2012.
- [60] W. Kohn, “Analytic properties of Bloch waves and Wannier functions,” *Phys. Rev.*, vol. 115, pp. 809–821, Aug 1959.
- [61] J. Dalibard and C. Cohen-Tannoudji, “Laser cooling below the Doppler limit by polarization gradients: simple theoretical models,” *J. Opt. Soc. Am. B*, vol. 6, pp. 2023–2045, Nov 1989.
- [62] C. Robens, S. Brakhane, W. Alt, D. Meschede, J. Zopes, and A. Alberti, “Fast, high-precision optical polarization synthesizer for ultracold-atom experiments,” *Phys. Rev. Applied*, vol. 9, p. 034016, Mar 2018.
- [63] T. A. Savard, K. M. O’Hara, and J. E. Thomas, “Laser-noise-induced heating in far-off resonance optical traps,” *Phys. Rev. A*, vol. 56, pp. R1095–R1098, Aug 1997.
- [64] E. Hecht, *Optics*. Addison-Wesley, 4th ed., 1998.
- [65] “Technical note: Electro-optic modulator faqs.” <https://www.newport.com/n/electro-optic-modulator-faqs>. Accessed: 2021-04-26.
- [66] R. Paschotta, “article on ‘electro-optic modulators’ in the rp photonics encyclopedia.” https://www.rp-photonics.com/electro_optic_modulators.html. Accessed: 2021-04-26.

- [67] “Linios laser modulators - laser modulators introduction.” <https://www.qioptiq-shop.com/en/Precision-Optics/LINOS-Laser-Modulators-Pockels-Cells/LINOS-Laser-Modulators/Laser-Modulators-Introduction/>. Accessed: 2021-04-26.
- [68] Meadowlark Optics, Inc., “Response time in liquid-crystal variable retarders.” Application Notes, 2005.[Online].
- [69] N. Walker and G. Walker, “Polarization control for coherent communications,” *Journal of Lightwave Technology*, vol. 8, no. 3, pp. 438–458, 1990.
- [70] D. Jaksch, C. Bruder, J. I. Cirac, C. W. Gardiner, and P. Zoller, “Cold bosonic atoms in optical lattices,” *Phys. Rev. Lett.*, vol. 81, pp. 3108–3111, Oct 1998.
- [71] M. P. A. Fisher, P. B. Weichman, G. Grinstein, and D. S. Fisher, “Boson localization and the superfluid-insulator transition,” *Phys. Rev. B*, vol. 40, pp. 546–570, Jul 1989.
- [72] M. Łacki, D. Delande, and J. Zakrzewski, “Dynamics of cold bosons in optical lattices: effects of higher bloch bands,” *New Journal of Physics*, vol. 15, p. 013062, jan 2013.
- [73] D.-S. Lühmann, O. Jürgensen, and K. Sengstock, “Multi-orbital and density-induced tunneling of bosons in optical lattices,” *New Journal of Physics*, vol. 14, p. 033021, mar 2012.
- [74] S. Will, T. Best, U. Schneider, L. Hackermüller, D.-S. Lühmann, and I. Bloch, “Time-resolved observation of coherent multi-body interactions in quantum phase revivals,” *Nature*, vol. 465, pp. 197–201, May 2010.
- [75] H. T. Stoof, K. B. Gubbels, and D. B. Dickerscheid, *Optical Lattices*, pp. 391–430. Dordrecht: Springer Netherlands, 2009.
- [76] M. Kardar, *Statistical Physics of Fields*. Cambridge University Press, 2007.
- [77] G. K. Campbell, J. Mun, M. Boyd, P. Medley, A. E. Leanhardt, L. G. Marcassa, D. E. Pritchard, and W. Ketterle, “Imaging the Mott insulator shells by using atomic clock shifts,” *Science*, vol. 313, no. 5787, pp. 649–652, 2006.
- [78] S. Fölling, A. Widera, T. Müller, F. Gerbier, and I. Bloch, “Formation of spatial shell structure in the superfluid to Mott insulator transition,” *Phys. Rev. Lett.*, vol. 97, p. 060403, Aug 2006.
- [79] P. Cheinet, S. Trotzky, M. Feld, U. Schnorrberger, M. Moreno-Cardoner, S. Fölling, and I. Bloch, “Counting atoms using interaction blockade in an optical superlattice,” *Phys. Rev. Lett.*, vol. 101, p. 090404, Aug 2008.
- [80] J. F. Sherson, C. Weitenberg, M. Endres, M. Cheneau, I. Bloch, and S. Kuhr, “Single-atom-resolved fluorescence imaging of an atomic Mott insulator,” *Nature*, vol. 467, pp. 68–72, Sep 2010.

- [81] K. Sheshadri, H. R. Krishnamurthy, R. Pandit, and T. V. Ramakrishnan, “Superfluid and insulating phases in an interacting-boson model: Mean-field theory and the RPA,” *Europhysics Letters (EPL)*, vol. 22, pp. 257–263, may 1993.
- [82] T. D. Kühner, S. R. White, and H. Monien, “One-dimensional Bose-Hubbard model with nearest-neighbor interaction,” *Phys. Rev. B*, vol. 61, pp. 12474–12489, May 2000.
- [83] S. Will, *From Atom Optics to Quantum Simulation: Interacting Bosons and Fermions in Three-Dimensional Optical Lattice Potentials*. Springer Science & Business Media, 2012.
- [84] D.-S. Lühmann, *Multiorbital Physics in Optical Lattices*. PhD thesis, University of Hamburg, 2009.
- [85] P. N. Jepsen, W. W. Ho, J. Amato-Grill, I. Dimitrova, E. Demler, and W. Ketterle, “Transverse spin dynamics in the anisotropic Heisenberg model realized with ultracold atoms,” *arXiv preprint arXiv:2103.07866*, 2021.
- [86] J. Keeling, “Quantum magnetism,” *Lecture notes. University of St. Andrews*, 2008.
- [87] A. Auerbach, *Interacting electrons and quantum magnetism*. Springer Science & Business Media, 2012.
- [88] I. M. Georgescu, S. Ashhab, and F. Nori, “Quantum simulation,” *Rev. Mod. Phys.*, vol. 86, pp. 153–185, Mar 2014.
- [89] D. Dai, H. Xiang, and M.-H. Whangbo, “Effects of spin-orbit coupling on magnetic properties of discrete and extended magnetic systems,” *Journal of Computational Chemistry*, vol. 29, no. 13, pp. 2187–2209, 2008.
- [90] A. Kitaev, “Anyons in an exactly solved model and beyond,” *Annals of Physics*, vol. 321, no. 1, pp. 2–111, 2006. January Special Issue.
- [91] T. Moriya, “Anisotropic superexchange interaction and weak ferromagnetism,” *Phys. Rev.*, vol. 120, pp. 91–98, Oct 1960.
- [92] S. Trotzky, P. Cheinet, S. Fölling, M. Feld, U. Schnorrberger, A. M. Rey, A. Polkovnikov, E. A. Demler, M. D. Lukin, and I. Bloch, “Time-resolved observation and control of superexchange interactions with ultracold atoms in optical lattices,” *Science*, vol. 319, no. 5861, pp. 295–299, 2008.
- [93] E. Koch, “Exchange mechanisms,” *Correlated electrons: from models to materials*, vol. 2, pp. 1–31, 2012.
- [94] D. J. Klein, “Degenerate perturbation theory,” *The Journal of Chemical Physics*, vol. 61, no. 3, pp. 786–798, 1974.

- [95] C. Cohen-Tannoudji, G. Grynberg, and J. Dupont-Roc, *Atom-Photon Interactions*, ch. 1: Transition Amplitudes in Electrodynamics, pp. 5–66. John Wiley & Sons, Ltd, 1998.
- [96] E. Demler, “Strongly correlated systems in atomic and condensed matter physics, lecture notes for physics 284, chapter 9.” <http://cmt.harvard.edu/demler/TEACHING/Physics284/chapter9.pdf>, February 2018. [Online; accessed 27-April-2021].
- [97] N. Jepsen, J. Amato-Grill, I. Dimitrova, W. Lunden, and W. Ketterle, “Spin-1 Heisenberg model with lithium-7.” Internal report.
- [98] F. Gerbier, A. Widera, S. Fölling, O. Mandel, and I. Bloch, “Resonant control of spin dynamics in ultracold quantum gases by microwave dressing,” *Phys. Rev. A*, vol. 73, p. 041602, Apr 2006.
- [99] D. M. Stamper-Kurn and M. Ueda, “Spinor bose gases: Symmetries, magnetism, and quantum dynamics,” *Rev. Mod. Phys.*, vol. 85, pp. 1191–1244, Jul 2013.
- [100] T. Fukuhara, A. Kantian, M. Endres, M. Cheneau, P. Schauß, S. Hild, D. Bellem, U. Schollwöck, T. Giamarchi, C. Gross, I. Bloch, and S. Kuhr, “Quantum dynamics of a mobile spin impurity,” *Nature Physics*, vol. 9, pp. 235–241, Apr 2013.
- [101] S. Hild, T. Fukuhara, P. Schauß, J. Zeiher, M. Knap, E. Demler, I. Bloch, and C. Gross, “Far-from-equilibrium spin transport in Heisenberg quantum magnets,” *Phys. Rev. Lett.*, vol. 113, p. 147205, Oct 2014.
- [102] S. Fölling, *Probing strongly correlated states of ultracold atoms in optical lattices*. PhD thesis, Johannes Gutenberg University of Mainz, 2008.
- [103] E. Altman, E. Demler, and M. D. Lukin, “Probing many-body states of ultracold atoms via noise correlations,” *Phys. Rev. A*, vol. 70, p. 013603, Jul 2004.
- [104] S. Fölling, F. Gerbier, A. Widera, O. Mandel, T. Gericke, and I. Bloch, “Spatial quantum noise interferometry in expanding ultracold atom clouds,” *Nature*, vol. 434, pp. 481–484, Mar 2005.
- [105] A. M. Kaufman, R. P. Anderson, T. M. Hanna, E. Tiesinga, P. S. Julienne, and D. S. Hall, “Radio-frequency dressing of multiple Feshbach resonances,” *Phys. Rev. A*, vol. 80, p. 050701, Nov 2009.
- [106] J. T. M. Walraven, “Quantum gases.” https://staff.fnwi.uva.nl/j.t.m.walraven/walraven/Publications_files/2019-Quantum-Gases.pdf, October 2019. [Online; accessed 09-May-2021].
- [107] K. M. Mertes, J. W. Merrill, R. Carretero-González, D. J. Frantzeskakis, P. G. Kevrekidis, and D. S. Hall, “Nonequilibrium dynamics and superfluid ring excitations in binary bose-einstein condensates,” *Phys. Rev. Lett.*, vol. 99, p. 190402, Nov 2007.

- [108] P. Chauhan, F. Mahmood, H. J. Changlani, S. M. Koochpayeh, and N. P. Armitage, “Tunable magnon interactions in a ferromagnetic spin-1 chain,” *Phys. Rev. Lett.*, vol. 124, p. 037203, Jan 2020.
- [109] S. Braun, M. Friesdorf, S. S. Hodgman, M. Schreiber, J. P. Ronzheimer, A. Rivera, M. del Rey, I. Bloch, J. Eisert, and U. Schneider, “Emergence of coherence and the dynamics of quantum phase transitions,” *Proceedings of the National Academy of Sciences*, vol. 112, no. 12, pp. 3641–3646, 2015.
- [110] L. Pitaevskii and S. Stringari, *Bose-Einstein condensation and superfluidity*, vol. 164. Oxford University Press, 2016.
- [111] J. Simon, W. S. Bakr, R. Ma, M. E. Tai, P. M. Preiss, and M. Greiner, “Quantum simulation of antiferromagnetic spin chains in an optical lattice,” *Nature*, vol. 472, pp. 307–312, Apr 2011.
- [112] H. Gross, H. Zügge, M. Peschka, and F. Blechinger, *Aberrations*, ch. 29, pp. 1–70. John Wiley & Sons, Ltd, 2006.
- [113] R. Barakat, “Rayleigh wavefront criterion,” *J. Opt. Soc. Am.*, vol. 55, pp. 572–573, May 1965.
- [114] QED Technologies, Inc. personal communication.
- [115] S. Brakhane, W. Alt, D. Meschede, C. Robens, G. Moon, and A. Alberti, “Note: Ultra-low birefringence dodecagonal vacuum glass cell,” *Review of Scientific Instruments*, vol. 86, no. 12, p. 126108, 2015.
- [116] F. Le Kien, P. Schneeweiss, and A. Rauschenbeutel, “Dynamical polarizability of atoms in arbitrary light fields: general theory and application to cesium,” *The European Physical Journal D*, vol. 67, p. 92, May 2013.